Technische Universität München
Fakultät für Chemie
Lehrstuhl für Technische Chemie II

Modification of MFI zeolites with extra-framework $Si(OH)_x$ groups for catalytic cracking

Ruixue Zhao

Vollständiger Abdruck der von der Fakultät für Chemie der Technischen Universität München zur Erlangung des akademischen Grades eines

Doktors der Naturwissenschaften (Dr. rer. nat.)

genehmigten Dissertation.

Vorsitzender:	Prof. Dr. -Ing. Kai-Olaf Martin Hinrichsen
Prüfer der Dissertation:	Prof. Dr. Johannes A. Lercher
	Hon.-Prof. Dr. Richard W. Fischer
	Prof. Gary L. Haller, Ph.D. (Yale University, USA)

Die Dissertation wurde am 30.06.2020 bei der Technischen Universität München eingereicht und durch die Fakultät für Chemie am 17.06.2021 angenommen.

献给我至爱的家人们。

To my beloved family.

纪念我亲爱的母亲。

To memory my beloved mother.

知止而后有定,

定而后能静, 静而后能安,

安而后能虑, 虑而后能得.

——《大学》

Acknowledgements

My sincere appreciation is firstly expressed to the supervisor of my doctoral work, Prof. Dr. Johannes A. Lercher. Thanks for providing me the opportunity to do research in his group working on such an innovative and challenging topic. During my stay here, I experienced his rigorous attitude to work and his profound knowledge. I have been always inspired by his passion of science, his expertise in research and his humor and wisdom. It has been a great pleasure to do my Ph. D. thesis under his supervision.

My special gratitude goes to Dr. Yue Liu, for his insightful mentoring and supporting. He is such a brilliant scientist, who always comes up with novel and exciting ideas. His passionate attitude towards scientific studies as well as life inspired me a lot not only for my doctoral period but also for the future.

I owe as well gratitude to Dr. Ricardo Bermejo de Val for his guidance during the past years. He led me to the deeper-understanding world of synthesis. He granted me the freedom in research and encouraged me all the time, which I deeply appreciate.

I warmly thank Dr. Maricruz Sanchez-Sanchez for her supervising in the earlier stage of my doctoral work. Thanks to her kindness and patience on me as a junior in the group. Without her help, I could not get my research started smoothly.

Grateful thanks go to Prof. Dr. Andreas Jentys for all the scientific discussions and suggestions, especially on the infrared. I would like to also thank other senior members in our group, Dr. Hui Shi, Dr. Erika E. Ember and Dr. Eszter Baráth for all of their help in the past years. I owe my special thanks to Franz-Xaver Hecht, the magician of TCII, the hero in my heart, who solved enormous amount of the troubles on my set up and did the BET measurements for me. I would like to also thank Martin Neumann for his help on the AAS measurements and all the chemical stuff, Andreas Marx for all his efforts with the

electronic devices. I am grateful to our nice secretaries, Bettina Federmann, Stefanie Seibold, Kateryna Kryvko and Ulrike Sanwald, for their great assistance with all the administrative matters.

I am very grateful to all the former and present members of TCII, it is lucky to have all of them as colleges and friends. I would like to thank Dr. Guoju Yang, who is the first one to say “Hi” to me when I was here; Dr. Yang Song, who taught me the serious meaning of fashion; Dr. Yuanshuai Liu, who has the incredible power and installed my wardrobe; Dr. Yu Lou, who made my living in Germany much easier with his extensive experience; Dr.Wanqiu Luo, who I could share funny videos to; Dr. Yang Zhang, who did the previous work that helped me a lot; Dr. Wei Zhang, Guanhua Cheng, Fuli Deng, Lingli Ni, Xi Chen, Lei Tao, with whom we had so much good time together making my life in Germany less homesick; Niklas Pfriem, who is always nice, gentle and good-looking; Ferdinand Vogelgsang, Martin Baumgätl and Roland Weindl, who made and witness my first drunk; Teresa Schachtl, who went home even later than me sometimes so that I was not alone; Matina Aigner, who helped me a lot on my solid state NMR mesurements; Verena Höpfl, from whom I could always get components for my setup; Laura Löbbert, who led me to dance; Insu Lee, who gave me his measuring day on Vertex IR for me to finish the very last adsorption data; and all the other members who are not mentioned here, for their help and the great time we have shared in the group.

Very special thanks go to my friends Yuan Tan, Xian Gao and their lovely cats Shima and Danny for being my family here in Germany. They lent me their couch when I could not find a dwelling place in Munich and supported me in any difficult situations. We have experienced so much together in the past and we will have more fun time in the future. Besides, I would like to give my best wishes to Yuan Tan to finish her Ph. D and become Dr. Tan in the near future.

My thanks as well go to the Chinese Scholarship Council for the financial support of my living in Germany.

Finally yet importantly, my greatest gratitude goes to my family, especially my father, Jixin Zhao, who is the greatest father in the world, offering me the

unconditional supporting and holding his faith in me for all the time during my growth until now. I would like to say “爸爸我爱你” to him. I appreciate my stepmother, Suhua Hui, for disburdening my studying aboard for such a long time. I as well appreciate my aunts, uncles for all their love during my growth. They are the best I have in my life.

Ruixue Zhao

11.03.2020

Abstract

Novel zeolitic Brønsted acid sites have been synthesized via grafting of extra-framework silica in H-MFI zeolite next to conventional Brønsted acid sites. The proximity of both functional groups leads to hydrogen bonding and strengthens the interaction with pyridine and amines via van der Waals interaction with their aryl or alkyl chains. This new site increases the reaction rate of protolytic cracking of n-pentane via a mechanism different from extra lattice alumina by decreasing the activation energy, stabilizing the transition state enthalpically.

Kurzzusammenfassung

Durch chemische Verankerung von $Si(OH)_x$ Gruppen an Sauerstoffe des Zeolithgerüsts wurden neue zeolithische Brønsted-saure Zentren in H-MFI-Zeolithen synthetisiert. Die Nähe der $Si(OH)_x$ Gruppen zu Brønsted sauren Zentren führt zur Ausbildung von Wasserstoffbrücken. Dies resultierte in besonders starken Wechselwirkungen mit Pyridin und Aminen über die van der Waals Wechselwirkung mit ihren Aryl- oder Alkylketten. Dies führte zu einer deutlich höheren Reaktionsgeschwindigkeit des protolytischen Spaltens von n-Pentan. Die neuen Zentren zeigten eine deutlich niedrigere Aktivierungsenergie für die Reaktion.

Table of contents

Acknowledgements ..... **I**

Abstract ..... **IV**

Kurzzusammenfassung ..... **V**

Table of contents ..... **VI**

Abbreviations ..... **IX**

Symbols and indices ..... **XI**

List of figures, schemes and tables ..... **XIII**

Chapter 1. Introduction ..... **- 1 -**

1.1 Zeolites ..... **- 2 -**

1.1.1 Introduction of zeolite history ..... - 2 -

1.1.2 General introduction of zeolites ..... - 4 -

1.1.2.1 Frameworks and structures of zeolites ..... - 4 -

1.1.2.2 Acidity of zeolites ..... - 7 -

1.1.3 ZSM-5 zeolites ..... - 8 -

1.1.3.1 Framework structure of ZSM-5 ..... - 9 -

1.1.3.2 Nature of acid sites ..... - 11 -

1.1.3.3 Post treatments on ZSM-5 ..... - 13 -

1.2 Catalytic cracking of alkanes over MFI zeolites ..... **- 15 -**

1.2.1 Stages of heterogeneous reactions ..... - 15 -

1.2.2 Protolytic cracking of alkanes ..... - 22 -

1.2.3 Promotion of cracking activity by extra framework Al ..... - 26 -

1.2.4 Studies on extra framework Si (EFSi) ..... - 28 -

1.3 Scope of the thesis ..... - 28 -

Chapter 2. Experimental ..... - 30 -

2.1 Chemicals and materials ..... - 31 -

2.2 Sample preparation ..... - 32 -

2.2.1 Removal of extra-framework aluminum ..... - 32 -

2.2.2 Si grafting by silylamine post treatment ..... - 32 -

2.3 Catalyst characterization ..... - 33 -

2.3.1 X-ray diffraction ..... - 33 -

2.3.2 Nitrogen physisorption ..... - 33 -

2.3.3 Elemental analysis ..... - 34 -

2.3.4 Titration of acid sites with pyridine ..... - 34 -

2.3.5 Titration of acid sites with ammonia ..... - 34 -

2.3.6 Adsorption of n-pentane ..... - 35 -

2.3.7 Adsorption of N-methylpropylamine and diethylamine ..... - 36 -

2.3.8 Adsorption of diethyl ether, water and methanol ..... - 37 -

2.4 Catalytic reaction of n-pentane cracking ..... - 37 -

Chapter 3. Synthesis, identification and quantification of EFSi-BAS and its adsorption properties. ..... - 39 -

3.1 Synthesis, identification and quantification of EFSi-BAS ..... - 40 -

3.1.1 The presence of EFSi ..... - 40 -

3.1.2 Quantification of BAS and EFSi-BAS on EFSi-MFIs ..... - 44 -

3.2 Influence of EFSi on the adsorption properties ..... - 48 -

3.2.1 Acid strength of BAS and EFSi-BAS ..... - 48 -

3.2.2 N-pentane adsorption on H-MFI and EFSi-MFI ..... - 50 -

3.2.3 N-methylpropylamine adsorption on H-MFI and EFSi-MFI ..... - 54 -

3.2.4 Diethyl ether adsorption on H-MFI and EFSi-MFI ..... - 57 -

3.2.5 Water adsorption on H-MFI and EFSi-MFI ..... - 60 -

3.2.6 Methanol adsorption on H-MFI and EFSi-MFI ..... - 63 -

3.3 Chapter summary ..... - 65 -

Chapter 4. Catalytic activity of EFSi-BAS in n-pentane cracking ..... - 67 -

4.1 The turn over frequency (TOF) of n-pentane cracking on BAS and EFSi-BAS - 68 -

4.2 Analysis of reaction barriers and transition states in n-pentane cracking ... - 75 -

4.2.1 Adsorption of n-pentane ..... - 75 -

4.2.2 Analysis of the reaction barriers in n-pentane cracking ..... - 76 -

4.2.3 Analysis of the transition states in n-pentane cracking ..... - 79 -

4.3 Chapter summary ..... - 84 -

Chapter 5. Summary and conclusion ..... - 86 -

References ..... - 88 -

Associated content ..... - 105 -

Abbreviations

ZSM-5	Zeolite Socony Mobil-5
$AlPO_4$	Aluminophosphate
NMR	Nuclear magnetic resonance
PBU	Primary building unit
SBU	Secondary building unit
3D	Three dimensinal
MR	Member rings
BAS	Brønsted acid sites
LAS	Lewis acid sites
EFAl	Extra framework aluminum
NH_3-TPD	Ammonia temperature programmed desorption
MAS	Magic-angle spinning
CCS	Catalytic cracking of silane
CVD	Chemical vapour deposition
CLD	Chemical liquid deposition
TEOS	Tetraethoxysilane
TMOS	Tetramethoxysilane
LH mechanism	Langmuir-Hinshelwood mechanism
ER mechanism	Eley-Rideal mechanism
TST	Transition state theory

SBAS	Strong Brønsted acid sites
Ref.	Reference
EFSi	Extra framework silica
IR	Infrared
AHFS	Ammonia hexafluorosilicate
wt.	Weight
BET	Brunauer-Emmett-Teller
AAS	Atomic absorption spectroscopy
FT-IR	Fourier transformed infrared spectroscopy
TG	Thermogravimetry
DSC	Differential scanning calorimetry
GC	Gas chromatography
FID	Flame ionization detector
N_2	Dinitrogen
XRD	X-ray diffraction
TOF	Turn over frequency
e.g.	exempli gratia
i.e.	id est
etc.	et cetera
approx.	approximately

Symbols and indices

Å	10^{-10} m	Angstrom
ΔH	kJ mol^{-1}	Enthalpy
ads.		Adsorption
meas.		Measured
int.		Intrinsic
des.		Desorption
react.		Reaction
K		Equilibrium constant
p	bar	Partial pressure
k		Rate constant
k_B	J K^{-1}	Boltzmann’s constant
T	K	Absolute temperature
h	J s	Plank’s constant
R	J mol^{-1} K^{-1}	Gas constant
ΔG	kJ mol^{-1}	Gibbs free energy
ΔS	J mol^{-1} K^{-1}	Entropy
ϴ		Standard state
TS		Transition state
n	mol	Amount of substance
max.		Maximum

TOF	s^{-1}	Turn over frequency
‡		Transition state
ΔQ	kJ mol^{-1}	Calorimetrically measured differential heat
θ		Fractional occupancy of the adsorption site
κ		Transmission coefficient
v		Stretching vibration
δ		In-plane bending vibration
γ		Out-plane bending vibration

List of figures, schemes and tables

Figure 1.1. Examples of secondary building units in zeolites (the corner of the polyhedral represent tetrahedral atoms). .....- 5 -

Figure 1.2. Bridging hydroxyl groups (Brønsted acid sites) in zeolites. .....- 7 -

Figure 1.3. Lewis acid sites (LAS) in zeolites originated from (a) extraframework aluminium species, (b) metal cation compensating the charge of lattice and (c) isomorphic substitution of silicon by a metal. .....- 8 -

Figure 1.4. (a) The secondary building unit, (b) pentasil unit and (c) pentasil chain in ZSM-5 zeolite.....- 9 -

Figure 1.5. Framework of ZSM-5 viewed along (a) [010] and (b) [100][45].....- 10 -

Figure 1.6. The intersecting channel system in ZSM-5[44]. .....- 10 -

Figure 1.7. 10-member rings of ZSM-5 viewed along (a) [010] and (b) [100]. .....- 11 -

Figure 1.8. Transport and the boundary layer around the surface of a catalyst pellet. ..- 16 -

Figure 1.9. Diffusivity of gas phase molecules. .....- 17 -

Figure 1.10. Energy diagram of a catalytic reaction. .....- 18 -

Figure 1.11. (a) Langmuir-Hinshelwood mechanism, (b) Eley-Rideal mechanism and (c) Mars van Krevelen mechanism. .....- 21 -

Figure 1.12. Energy scheme for protolytic cracking on zeolites. .....- 25 -

Figure 1.13. (a) Impact of AHFS modification on n-pentane cracking and dehydrogenation rates over MFI zeolites with different Si/Al ratios (adapted from Ref.[89], rounded symbols for the rates on MFI zeolites without EFAl removal and triangle symbols for the rates on MFI zeolites after EFAl removal) and (b) the promotion effect of n-pentane cracking and dehydrogenation over MFI zeolites by EFAl (adapted from Ref.[129]). .....- 27 -

Figure 3.1. IR spectra for samples during EFSi grafting. (a) H-MFI, (b) H-MFI with adsorbed n,n-dimethyltrimethylsilylamine $(CH_3)_3SiN(CH_3)_2$ (65% loading corresponding to the Al content) and (c) after calcination to EFSi-MFI-61%. (Spectra taken at 423 K.) .- 40 -

Figure 3.2. XRD patterns of H-MFI and EFSi-MFIs. .....- 41 -

Figure 3.3. N_2 adsorption-desorption isotherms on H-MFI and EFSi-MFIs at 77 K. ..- 42 -

Figure 3.4. IR spectra of OH stretching vibration region of H-MFI and EFSi-MFIs. ...- 43 -

Figure 3.5. Pyridine adsorption on H-MFI and EFSi-MFIs. Difference IR spectra of OH stretching and NH bending vibration region for (a) H-MFI and (b) – (d) EFSi-MFIs with increasing pyridine uptake at 423K; BAS-OH (3610 cm^{-1}) coverage under different HPy^+ concentrations on (e) H-MFI and (f) – (h) EFSi-MFIs. (HPy^+ concentration determined

from the peak area of 1545 cm^{-1} band; BAS-OH coverage determined from the peak area of 3610 cm^{-1} band.) .....- 45 -

Figure 3.6. Ammonia, diethylamine, N-methylpropylamine and pyridine adsorption on EFSi-MFI-46% at 423 K. BAS-OH coverage (determined from the area decrease of band 3610 cm^{-1} on IR spectra) under different concentrations of protonated probe molecules, i.e. ammonium ion, diethylaminium ion, N-methylpropylaminium ion and pyridinium ion.....- 48 -

Figure 3.7. Temperature-programmed desorption of ammonia for all samples. .....- 49 -

Figure 3.8. Pentane adsorption on H-MFI and EFSi-MFIs. Difference spectra of OH vibration region for with pentane adsorption at 333 K under different partial pressure. .....- 50 -

Figure 3.9. Difference spectra in OH stretching vibration region for (a) H-MFI, (b) EFSi-MFI-46% and (c) pre-pyridine-titrated EFSi-MFI-46% with sorbed pentane at 333 K under increasing pentane pressures up to the coverage* of ~346 µmol g-1 BAS-OH; (d) difference spectra between (b) and (c) showing the spectra of pentane on EFSi-BAS-OH, with the difference spectra of pentane on BAS-OH as reference. (*BAS-OH coverage determined from the peak area of 3610 cm^{-1} band. .....- 51 -

Figure 3.10. Difference IR spectra of O-H stretching and N-H bending vibration region (δNH_2) for (a) H-MFI and (b) EFSi-MFI-46% with increasing N-methylpropylamine uptake at 423 K. .....- 55 -

Figure 3.11. BAS coverage on (a) H-MFI and (b) EFSi-MFI-46% with increasing N-methylpropylamine uptake at 423 K. (Overall-BAS coverage determined from the peak area of 1605 cm^{-1} band for δNH_2; BAS-OH coverage determined from the peak area of 3610 cm^{-1} band.) .....- 56 -

Figure 3.12. Difference IR spectra of O-H stretching and C-H stretching vibration region for (a) H-MFI and (b) EFSi-MFI-46% with increasing diethyl ether uptake at 333 K..- 58 -

Figure 3.13. The band area decrease of 3610 cm^{-1} as a function of the band area increase of C-H vibration at 2850-3050 cm^{-1} on (c) H-MFI and (d) EFSi-MFI-46% upon diethyl ether adsorption at 333 K. .....- 59 -

Figure 3.14. Difference IR spectra for (a) H-MFI, (b) EFSi-MFI-46% with increasing water adsorption up to one H_2O molecule per overall-BAS-OH group at 423 K and (c) difference spectra between (b) and (a) showing difference of H_2O adsorption on H-MFI and EFSi-MFI-46% under the coverage of around one H_2O molecule per overall-BAS-OH ((1) H-MFI with H_2O adsorption, (2) EFSi-MFI-46% with H_2O adsorption and (3) subtraction of spectra (1) from (2)). .....- 61 -

Figure 3.15. Difference IR spectra for (a) H-MFI, (b) EFSi-MFI-46% with increasing methanol pressure up to 1 mbar at 423 K. .....- 64 -

Figure 4.1. Concentration of products in different reaction pathways at different contact time (1-3% pentane conversion) in H-MFI and EFSi-MFI-61% samples at 793K. - 69 -

Figure 4.2. First-order reaction of (a) overall cracking, (b) dehydrogenation and (c) – (e) different cracking pathways on H-MFI (black symbols) and EFSi-MFI-46% (colored symbols) at 793 K. .....- 70 -

Figure 4.3. TOF as a function of EFSi-BAS percentage on the samples at different temperatures. Solid symbols (■) for experimentally measured TOF, hollow symbols (□) for extrapolated TOF to 100% EFSi-BAS.....- 74 -

Figure 4.4. (a) Adsorption isotherms of n-pentane and (b) the heat of adsorption as a function of the concentration of adsorbed n-pentane on H-MFI and EFSi-MFIs at 333 K. .....- 75 -

Figure 4.5. Arrhenius plots of n-pentane cracking, shown by first order rate constant. (a) Overall cracking, (b) dehydrogenation and (c) – (e) different cracking pathways on BAS (black synbols) and EFSi-BAS (colored symbols). . .....- 77 -

Figure 4.6. Adsorption heat of amines on H-MFi and EFSi-MFI-46%. Differential heat of adsorption (black symbols) and integral heat of adsorption (blue symbols) of (a) N-methylpropylamine (CNCCC) and (b) diethylamine (CCNCC) on H-/EFSi-MFI at 423K.....- 81 -

Figure 4.7. Difference IR spectra of O-H stretching vibration region and N-H bending vibration region for (a) C2 (N-methylpropylamine, CNCCC) and (b) C3 (diethylamine, CCNCC) on EFSi-MFI-46% with increasing amine uptake at 423K. .....- 82 -

Figure 4.8. BAS coverage (%) as a function of overall BAS coverage (%) for CNCCC (■) and CCNCC (▲) adsorption on EFSi-MFI. (a) Overall scale up to fully coverage of total BAS and (b) amplified scale below 30% coverage of total BAS. (Total BAS coverage determined from the peak area of 1605 cm^{-1} band; BAS coverage determined from the peak area of 3610 cm^{-1} band.) .....- 83 -

Scheme 1.1. Binding of building units in the structure of zeolite (from primary building unit to secondary building unit).....- 4 -

Scheme 1.2. Shape selectivity of zeolites: (a) reactant shape selectivity, (b) product shape selectivity and (c) transition state shape selectivity (adapted from Ref.[33]).....- 6 -

Scheme 1.3. Reaction steps with intermediate configurations shown from dealumination (left) and desilication (right)[101].....- 14 -

Scheme 1.4. The stages of heterogeneous reactions.....- 16 -

Scheme 1.5. Elementary steps of protolytic cracking of n-pentane on zeolites. .....- 23 -

Scheme 2.1. EFSi introducing by adsorbing n, n-dimethyltrimethylsilylamine $(CH_3)_3SiN(CH_3)_2$ on BAS followed by calcination. .....- 33 -

Scheme 3.1. BAS perturbed by a neighboring EFSi. .....- 44 -

Scheme 3.2. Pyridine adsorption on (a) EFSi-BAS and (b) BAS.....- 47 -

Scheme 3.3. The structure of grafted EFSi, EFSi-BAS and pentane sorption on BAS and EFSi-BAS.....- 53 -

Scheme 3.4. N-methylpropylamine adsorption on the zeolitic BAS. .....- 54 -

Scheme 3.5. Proposed structure of adsorbed diethyl ether on BAS-OH group of MFI (adapted from Ref. [159]).....- 57 -

Scheme 3.6. Proposed structure of adsorbed water on BAS and EFSi-BAS. .....- 62 -

Scheme 3.7. Proposed structure of adsorbed methanol on SiOHAl groups. .....- 65 -

Scheme 4.1. Reaction pathways for n-pentane cracking on H-MFI. Red line indicates location of the bond scission. Dotted line represents the BAS proton coordinated with C or H in pentane as penta-coordinated carbon in transition state. .....- 68 -

Scheme 4.2. Cracking pathways going through C2 and C3 carbonium ion. .....- 79 -

Scheme 4.3. Amine adsorption on BAS simulating different transition states in n-pentane cracking. (a) N-Methylpropylamine adsorption on BAS simulating the C2 carbonium ion like transition state for P1 and P3 cracking pathways and (b) diethylamine adsorption on BAS simulating the C3 carbonium ion like transition state for P2 cracking pathway. .....- 80 -

Table 1.1. Heats of adsorption, apparent and intrinsic energies of activation of n-alkanes cracking over H-ZSM-5 at 773K[124]. .....- 26 -

Table 2.1. Chemicals and materials. .....- 31 -

Table 3.1. Physiochemical properties of H-MFI and EFSi-MFIs. .....- 42 -

Table 3.2. Acid site concentrations of H-MFI and EFSi-MFIs. .....- 47 -

Table 4.1. TOFs on different reaction pathways per BAS site (H-MFI) at 753 - 793 K with 0.020 bar of n-pentane. .....- 70 -

Table 4.2. TOFs on different reaction pathways in EFSi-MFI-18% at 753 - 793 K with 0.020 bar of n-pentane. .....- 71 -

Table 4.3. TOFs on different reaction pathways in EFSi-MFI-46% at 753 - 793 K with 0.020 bar of n-pentane. .....- 71 -

Table 4.4. TOFs on different reaction pathways in EFSi-MFI-61% at 753 - 793 K with 0.020 bar of n-pentane. .....- 72 -

Table 4.5. TOFs on different reaction pathways per EFSi-BAS site at 753 - 793 K with 0.020 bar of n-pentane. .....- 72 -

Table 4.6. Comparison of TOFs on different reaction pathways per BAS and EFSi-BAS at 753 K with 0.020 bar of n-pentane. .....- 74 -

Table 4.7. Adsorption properties of n-pentane on H-MFI and EFSi-MFIs at 333 K. ..- 76 -

Table 4.8. First order activation enthalpy and entropy of n-pentane cracking and dehydrogenation on BAS/EFSi-BAS. .....- 78 -

Table 4.9. Adsorption heat for N-methylpropylamine (CNCCC) and diethylamine (CCNCC) on H-MFI and EFSi-MFI-46% at 423K. .....- 84 -

Chapter 1. Introduction

1.1 Zeolites

1.1.1 Introduction of zeolite history

Zeolites are porous crystalline materials, generally crystalline aluminosilicates containing pores and cavities of molecular dimensions. The term of zeolite was firstly coined by Swedish mineralogist Axel Fredrik Cronstedt in 1756 from Greek with the meaning of boiling stones refers to the ability of adsorbing and releasing water[1–3].

Zeolites occur naturally from volcanic rocks and ash layers with alkaline groundwater or crystallize in post-depositional environments thousands to millions of years in shallow marine basins[4]. However, naturally obtained zeolites are commonly excluded from many applications due to their impurity arising from the contamination of other minerals, metals or quartz.

The development of the hydrothermal preparation method for zeolite synthesis started from the nineteenth century[5,6]. From the 1940s, Richard M. Barrer and Robert M. Milton, who are regarded as the founding fathers of zeolite synthesis science and practice, investigated the approach of the conversion of known mineral phases and synthesized the first zeolite (KFI structure[7]) using this approach[8–10]. From 1949 to 1951, Robert M. Milton developed a new and widely applicable method for synthesizing zeolites using soluble forms of silica and alumina precursors under highly alkaline conditions and discovered the A zeolite, B zeolite (later shown to be gismondine-type Na-P zeolite), C zeolite (later identified as basic sodalite) and a crystalline impurity named X (isostructural with faujasite)[10].

The following decade saw rapid developments in new synthesis and the investigation of the synthesis process. Such developments were initiated by introducing quaternary ammonium cations into the synthesis process. In 1967, the first high-silica zeolite, zeolite β with a Si/Al ratio from 5 to 100, was synthesized using tetraethylammonium cation as a structure-directing agent[4,11].

Upon the significant developments in the 1960s, not only the studies on zeolite synthesis methods but also the research on the kinetics and mechanism of synthesis process were explored in the 1970s. One of the most widely used zeolites nowadays, ZSM-5, was discovered in 1972[12]. The study of Al-free ZSM-5 using alkylammonium cations was afterwards published in 1978[13]. Moreover, Flanigen and Patton demonstrated a method using fluoride ion as a mineralizer in the synthesis of silicalite[14], which leads a series of studies in recent years.

In the 1980s, a new class of zeolites, aluminophosphates ($AlPO_4$s), was discovered[15]. This is the first family of molecular sieves synthesized without silica. Meanwhile, characterization techniques such as Raman spectroscopy and nuclear magnetic resonance (NMR) spectroscopy were applied to get a deeper understanding of the synthesis process and the properties of the zeolites[16].

Further discoveries on the porous materials with mesopores such as MCM-41 were aroused in the 1990s[17]. At the meantime, a new synthesis method of ZSM-5 in vapour phase was reported[18], which expanded a new field of zeolite synthesis.

Processing into the 21st century, with the increasing knowledge and related technological advances, the state of the zeolite science is tremendously developing in the field of synthesis mechanism[19–22], modifications on the zeolites through post treatments[23,24], discovering new zeolitic materials[25] and the applications of the zeolites in industry[21].

Nowdays, more than 200 unique frameworks of zeolites have been identified[26],and the zeolite science is keeping on attracting researchers to explore more.

1.1.2 General introduction of zeolites

1.1.2.1 Frameworks and structures of zeolites

The primary building units (PBU) of the zeolites are tetrahedral frameworks consisting 4-corrdinated *T*-atoms (usually Si and Al) and bridging oxygen atoms[27]. The 3-dimentional networks of the zeolites are a result of the corners for the tetrahedral PBUs being shared. By sharing the oxygen atoms, the special geometric forms of the secondary building units (SBU) are formed (**Scheme 1.1**). The existing classification of zeolite frameworks depends on the secondary building units, which can contain up to 16 *T*-atoms[27].

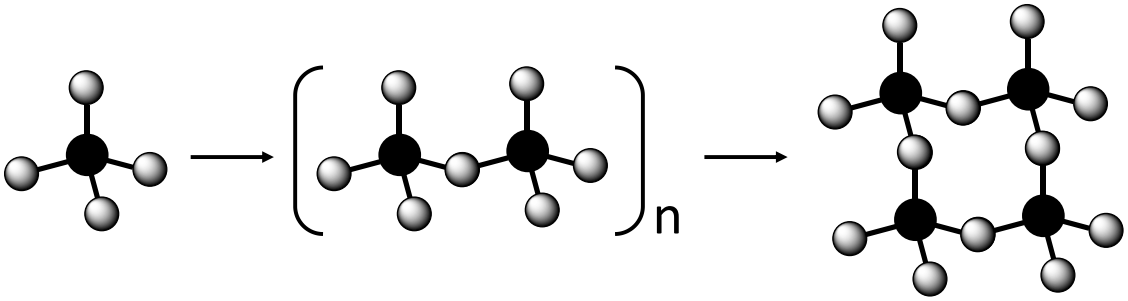

Scheme 1.1. Binding of building units in the structure of zeolite (from primary building unit to secondary building unit).

Figure 1.1 shows examples of secondary building units in zeolites. These SBUs connect topologically and form the specific 3D structures with different opening windows, pore channels and cages. Zeolites with unique frameworks have their corresponding minimum kinetic diameters for inorganic and organic molecules passing through. The minimum kinetic diameters, which depend on the geometrical *T*-O rings, are critical in scientific studying and industrial applications. *T*-O rings with varying number of members differ in kinetic diameters. For example, the diameter of the pores in zeolites with 8, 10 and 12 member rings (MR, referring to *T*-atoms) are approximately 4.5, 6 and 8 Å,

respectively[28]. Thus zeolites are classified as small pore zeolites (8-MR structures, e. g., CHA)[29], medium pore zeolites (10-MR structures, e. g., ZSM-5)[30], large pore zeolites (12-MR structures, e. g., FAU) and extra-large pore zeolites (rings larger than 12-MR, e. g., ITQ-33)[31].

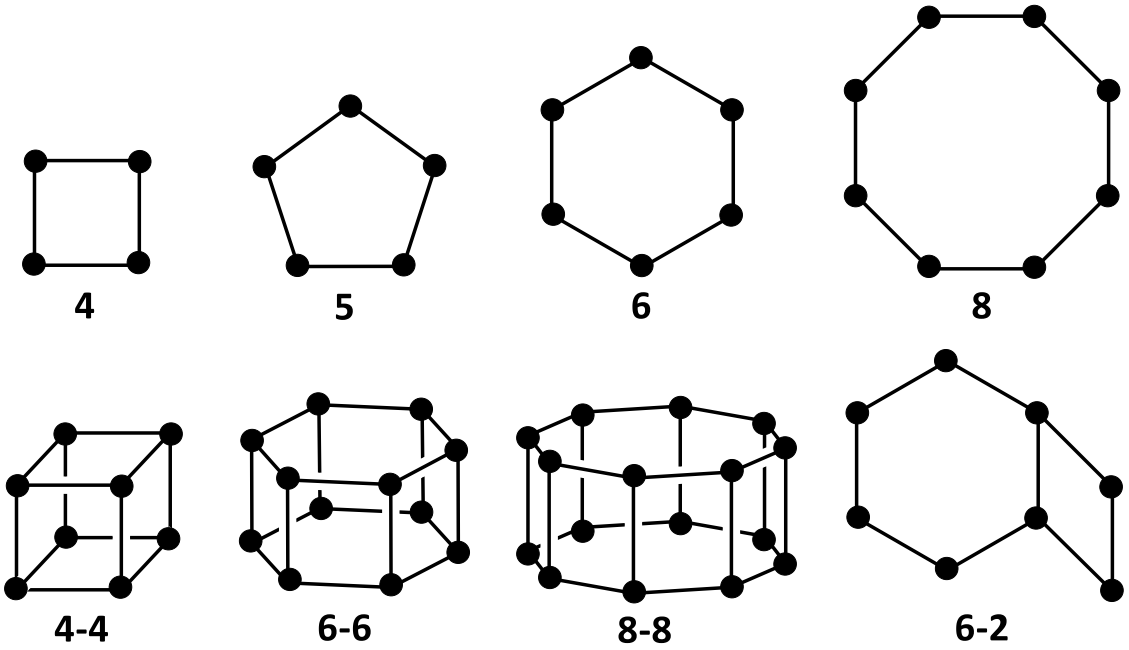

Figure 1.1. Examples of secondary building units in zeolites (the corner of the polyhedral represent tetrahedral atoms).

In general, zeolites can impose shape selective constraints through different frameworks, which in turn, lead to extremely discriminated reaction outcomes[32]. There are three forms of shape selectivity: reactant shape selectivity, product shape selectivity and transition state shape selectivity [33–35]. Reactant shape selectivity (**Scheme 1.2 a**) occurs when the reactant molecules are too large to enter the zeolites pores and reach the active sites, therefore they cannot convert to products. Product shape selectivity (**Scheme 1.2 b**) occurs when some of the product within the pores are too bulky to diffuse out as obtainable products. Transition state shape selectivity (**Scheme 1.2 c**) occurs when one or several transition states are too large that requires more space in the cavities.

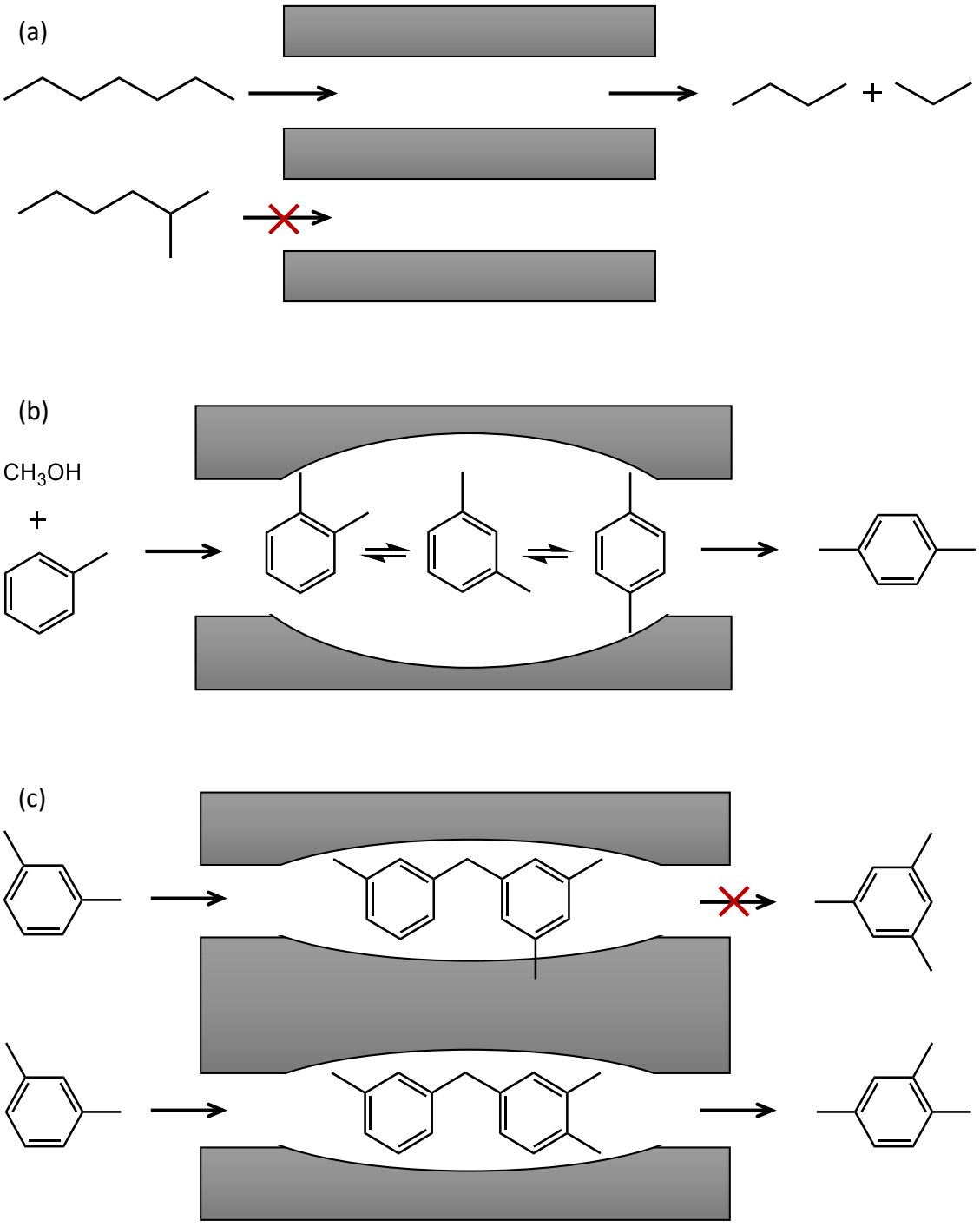

Scheme 1.2. Shape selectivity of zeolites: (a) reactant shape selectivity, (b) product shape selectivity and (c) transition state shape selectivity (adapted from Ref.[33]).

1.1.2.2 Acidity of zeolites

In a zeolite containing only silicon and oxygen (siliceous zeolite), all the tetrahedral PBUs are SiO_4. In this case, the framework of the zeolite is charge neutral and there is no acidity. However, most of the well-known zeolites are aluminosilicates. For these zeolites, Al^{3+} isomorphically substitutes some of the Si^{4+} in the framework, resulting in a negative charge of the $[AlO_4]^-$ tetrahedral PBUs, which can be balanced by the presence of a proton (H^+) or a cation (e. g., Na^+)[36]. The proton or the cation is attached to the oxygen atom connected to neighbour silicon and aluminium atoms. In case of proton, a bridging hydroxyl group is formed (**Figure 1.2**), this kind of bridging hydroxyl groups are the Brønsted acid sites of zeolites.

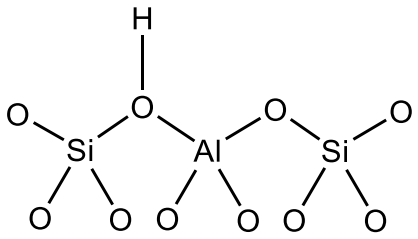

Figure 1.2. Bridging hydroxyl groups (Brønsted acid sites) in zeolites.

In addition to Brønsted acid sites, zeolites can also possess Lewis acid sites. Generally, Lewis acidity in zeolites originates from the presence of extra framework aluminium (EFAl) species (**Figure 1.3 a**)[37]. The EFAl species is created not only during the synthesis but also by post treatment such as mild steaming[38–40]. In addition, Lewis acid sites can be also generated by a metal cation (e.g., Cu^{2+}, Zn^{2+}) compensating the lattice charge (**Figure 1.3 b**)[41] and the isomorphic substitution of silicon by a metal (e.g., Ti^{4+}, Zr^{4+}, Sn^{4+}) in a pure silica framework (**Figure 1.3 c**)[38,42].

There are many different methods to characterize the acidity of the zeolites, the details for these method will be discussed in the following sections taking ZSM-5 zeolite as an example.

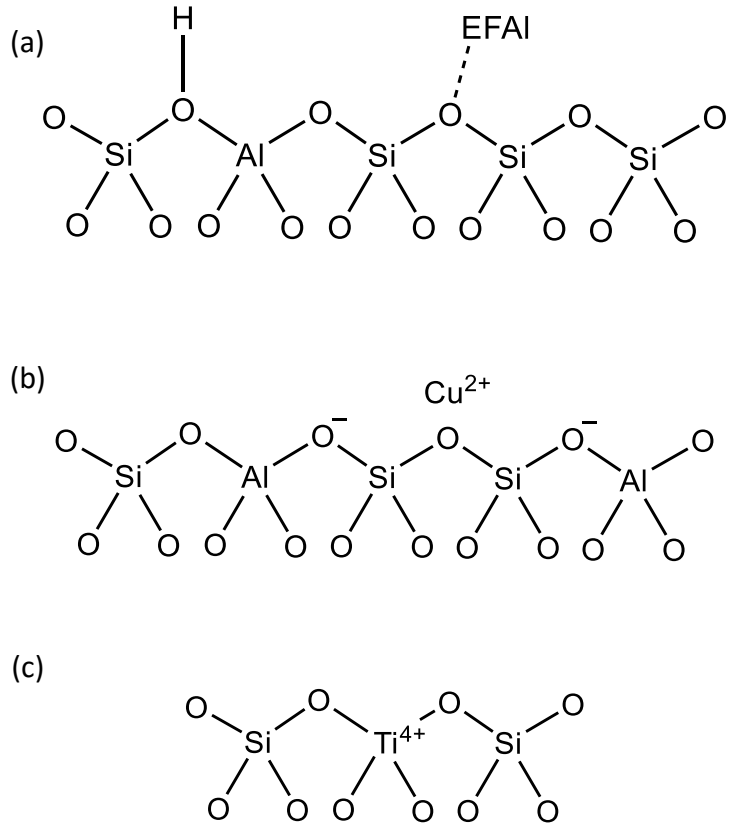

Figure 1.3. Lewis acid sites (LAS) in zeolites originated from (a) extraframework aluminium species, (b) metal cation compensating the charge of lattice and (c) isomorphic substitution of silicon by a metal.

1.1.3 ZSM-5 zeolites

ZSM-5, Zeolite Socony Mobil-5, is an aluminosilicate zeolite with the framework type MFI. It was synthesized by Robert J Argauer and George R Landolt in 1969 and then patented by Mobil Oil Company in 1972[12]. ZSM-5 is now one of the most widely used zeolites in the petroleum industry as a heterogeneous catalyst.

1.1.3.1 Framework structure of ZSM-5

As a member of the pentasil family of zeolites, ZSM-5 is composed of several pentasil units (**Figure 1.4 b**) containing the 5-1 secondary building units (**Figure 1.4 a**) to form pentasil chains (**Figure 1.4 c**)[43]. The pentasil chains then interconnect by oxygen bridges and construct the three dimensional framework structure of the zeolites (**Figure 1.5**).

The framework structure of ZSM-5 encloses two intersecting channels, one straight running parallel to [010] and the other sinusoidal (also described as zigzag channel) running parallel to [001] (**Figure 1.6**)[43,44]. Both the straight channel and the sinusoidal channel contain 10 member rings and they slightly differ in the kinetic diameters, which are, the limited diameter for straight channels 5.3 × 5.6 Å and the one for sinusoidal channels 5.1 × 5.5 Å (**Figure 1.7**).

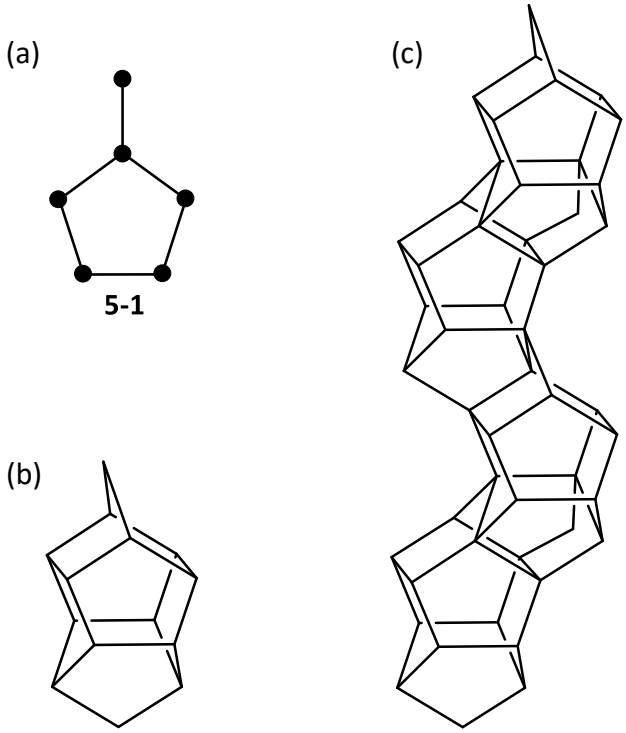

Figure 1.4. (a) The secondary building unit, (b) pentasil unit and (c) pentasil chain in ZSM-5 zeolite.

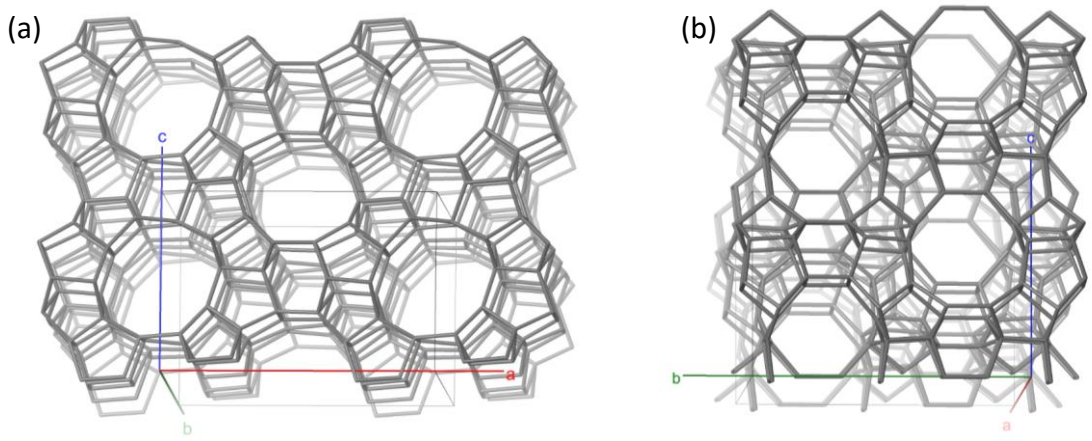

Figure 1.5. Framework of ZSM-5 viewed along (a) [010] and (b) [100][45].

The unique pore channels of ZSM-5 offer an effective size selectivity in many reactions. For example, in the isomerization of meta-xylene to para-xylene, para-xylene is able to traverse along the pore channels of the zeolite due to its higher diffusion coefficient than meta-xylene. Therefore, the reaction can occur quickly in a high yield[46].

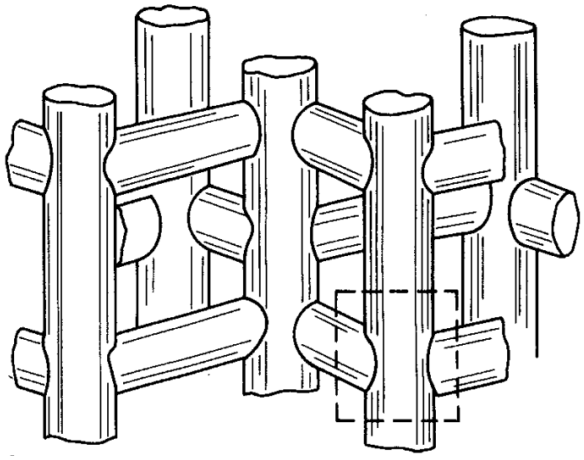

Figure 1.6. The intersecting channel system in ZSM-5[44].

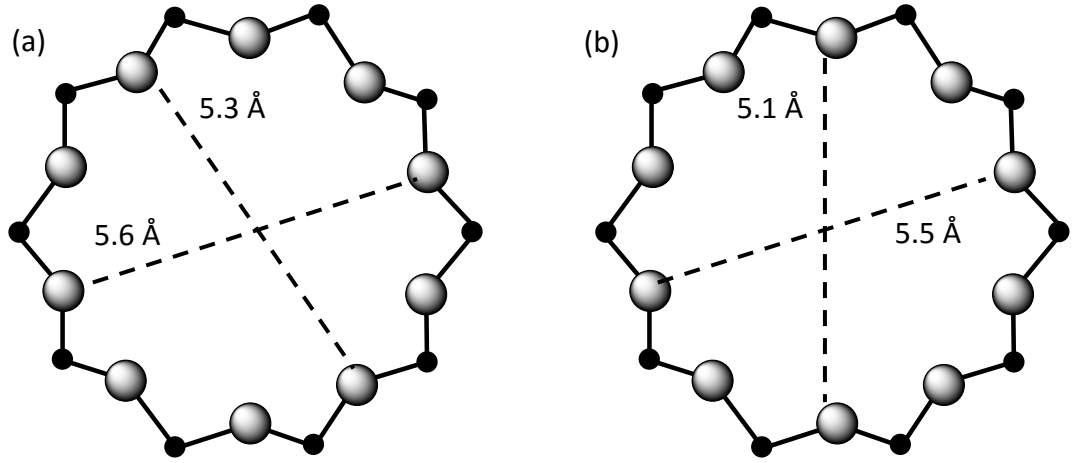

Figure 1.7. 10-member rings of ZSM-5 viewed along (a) [010] and (b) [100].

1.1.3.2 Nature of acid sites

As one of the most widely used heterogeneous catalyst in the chemical and petroleum industry, ZSM-5 is employed in many reactions such as cracking[47,48], isomerization[49] and alkylation[50]. It is accepted that active centers catalyzing these reactions are the bridging OH groups (SiOHAl) in the zeolites having Brønsted acidity [47–56]. ZSM-5 zeolite has a Si/Al ratio in the range of 10 to infinite[57,58]. In the zeolites with low Si/Al ratio, a part of the Al atoms exist in the extra framework positions (EFAl) act as Lewis acid sites[57]. It is widely accepted that there are three different locations for the acid sites in the pore system of ZSM-5: within the straight channels, within the sinusoidal channels or at the intersections of the sinusoidal and straight channels[59]. The relative distribution of the acid sites have a significant impact on the catalytic activity of the zeolites[60,61].

The properties of the acid sites have been studied over decades utilizing various methods such as titration, calorimetry and spectroscopy. The concentration of BAS is proportional to the Al content in the framework of ZSM-5. The acid strength can be altered by varying Al concentration[62–64], introducing other cations into the tectosilicate framework (e.g. B or Fe)[65–67], and partly exchanging the acid sites with rare-earth metal cations (e.g. La^{3+})[68–70].

Characterizations such as temperature programmed desorption of ammonia (NH_3-TPD) and infrared spectroscopy with probe molecule adsorption (*e.g.*, pyridine) are generally used to determine the concentration and the strength of the acid sites. Both ammonia and pyridine are typical base probe molecules used in the study of the acidity of the zeolites. Since these base molecules adsorb on the acid sites with a stoichiometry ratio of 1:1[71,72], the concentration of the acid sites can be determined from the amount of the adsorbed ammonia or pyridine in the zeolites and the acid strength can be determined from the desorption curve of the probe molecular under different temperatures.

In general, temperature programmed desorption (TPD) of ammonia indicates not only the acid amount of the zeolites but also the distribution of strength of acid sites. It has been reported that there are two peaks in the TPD of NH_3 from ZSM-5 zeolite: *l*-peak and *h*-peak. The *l*-peak showing at lower temperature is identified as physically adsorbed or weakly held ammonia while the *h*-peak showing at higher temperature is ascribable to the ammonia adsorbed on acid sites[73–75].

Pyridine is another frequently used probe molecule to study the surface acidity of the catalyst since the 1950s[76]. The infrared spectrum in the 1400 to 1700 cm^{-1} region with pyridine adsorption on the zeolites can be used to determine the concentration of Brønsted and Lewis acid sites[77]. Pyridine forms pyridinium ion (PyH^+) by the interaction with the proton on the BAS and gives a band at approximately 1540 cm^{-1} on the infrared spectrum[78–80]. The band at approximately 1450 cm^{-1} which is related to the coordinately bonded pyridine and hydrogen-bonded pyridine can be used as an indication to determine Lewis acidity[78,80].

Solid-state ^1H magic-angle spinning (MAS) NMR spectroscopy also serves as a tool for the characterization of zeolites acidity. It provides direct data on the type and of different hydroxyl groups in zeolites from the chemical shifts and their quantity from the peak areas. Studies addressing the properties of the hydroxyl groups in zeolites have shown that for a dehydrated H-ZSM-5 zeolite,

different proton species of Si-OH, Al-OH Si-OH-Al give peaks at around 1.7 ppm, 2.5 ppm and 3.9 ppm, respectively[81–84]. The chemical shift value and the spinning side bands can be used to infer the acid strength of the bridging hydroxyl groups[85–88]. Normally, a large chemical shift corresponds to a high acid strength.

1.1.3.3 Post treatments on ZSM-5

On the nature of the acid sites, it is also found that the activity of BAS is influenced by its local environment[51,89]. Post treatments such as dealumination, desilication (**scheme 1.3**) and silylation have been used to modify the zeolites to further study the interplay between the pore structure, acidity, catalytic activity and selectivity.

The Si/Al ratio of the zeolites is an important factor influencing the properties of the zeolites. Generally, zeolites with a low aluminium concentration are thermally and chemically more stable. However, the Si/Al ratio of a certain zeolite framework is restricted to a certain limit. In terms of these reasons, a desired zeolite with a low aluminium concentration can be obtained by post dealumination treatments. Nowadays, the mostly used methods for dealumination are steaming with water vapor [90] and acid leaching or hydrothermal treatment in a solution[91]. Normally, dealumination can create some extra framework aluminium species and form mesopores[92], sometimes it also lead to loss of the crystal strcture[93].

Desilication process follow the same pattern as the dealumination. It is also a post-synthetic way to create mesopores within the pore system[94–96]. The difference in this method compared to dealumination is that leaching treatment normally carried out by alkaline solutions.

Silylation is another widely used post treatment which is commonly conducted to block the active sites on the external surface of the zeolite, modifying the product selectivity[97]. For example, the location of the acid site of the ZSM-5 zeolite membrane can be controlled by a method called catalytic cracking of silane (CCS), which can selectively deactivate the acid sites at the outer surface of the zeolite membrane allowing an increasing selectivity of the

olefins by 10% in the methanol to olefin reaction[98]. Silylation is often performed by chemical vapour deposition (CVD)[99] or chemical liquid deposition (CLD)[100], using different silicon sources such as tetraethoxysilane (TEOS) and tetramethoxysilane (TMOS).

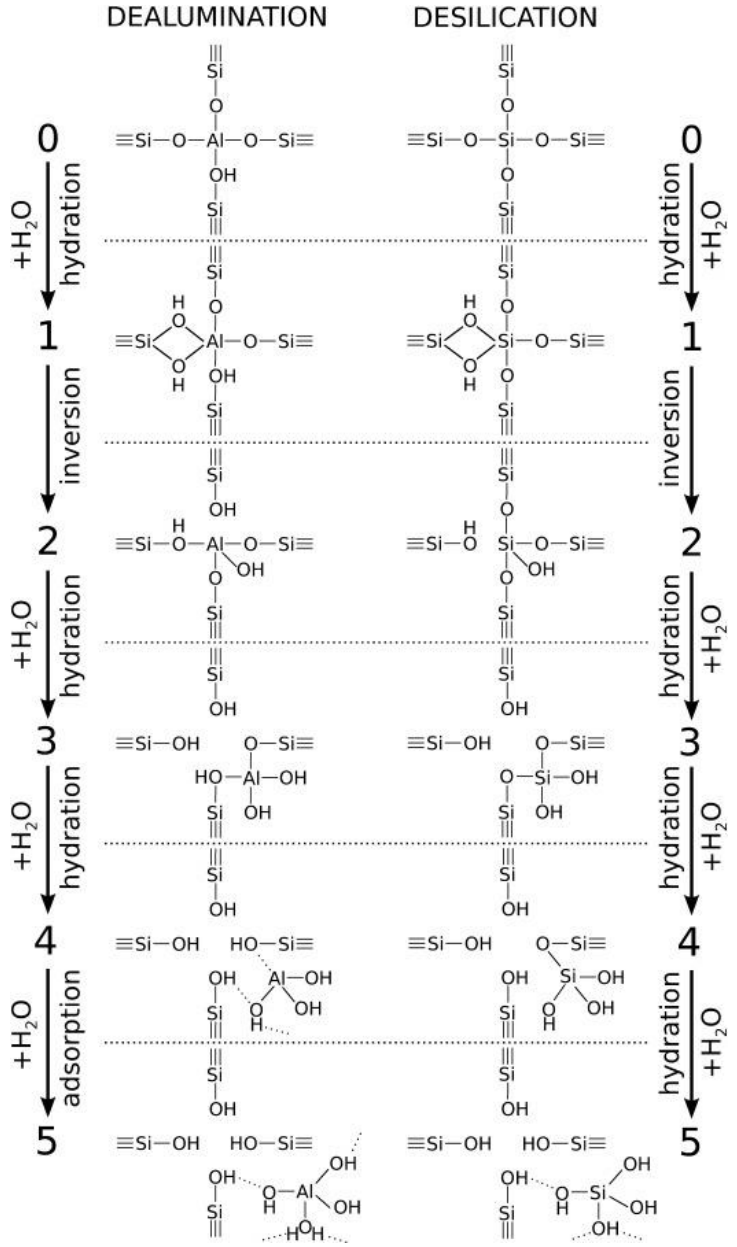

Scheme 1.3. Reaction steps with intermediate configurations shown from dealumination (left) and desilication (right)[101].

1.2 Catalytic cracking of alkanes over MFI zeolites

Catalytic cracking of medium-range petroleum fractions over zeolites is responsible for the manufacture of over 50% of gasoline in the world.[53] Alkane cracking over zeolite-based acidic catalysts as a typical heterogeneous reaction has been well examined in details. This section will introduce some of the basic knowledge.

1.2.1 Stages of heterogeneous reactions

The stages of heterogeneous reactions are shown in **Scheme 1.4**: ① external diffusion of the reactant from the bulk fluid to the outer surface of the zeolite, ② internal diffusion of the reactant from the pore mouth to the internal catalytic surface, ③ adsorption of the reactant on the active site, ④ reaction on the surface, ⑤ desorption of the product from the active site, ⑥ internal diffusion of the product from the catalytic surface to the pore mouth and ⑦ external diffusion of the product from the external surface to the bulk fluid.

Stage ① and ⑦ are external diffusions (**Figure 1.8**), which can be discussed in two cases. One is that the reaction occurs instantaneously on the surface of the catalyst pellet, thus the rate of mass transfer to the surface limits the overall rate of the reaction. Under this circumstance, the mass transfer coefficient should be taking into consideration, which is related to the temperature and the velocity of the fluid[102]. In the second case, the reaction is so slow that virtually no concentration gradient exists in the fluid phase the specific reaction rate is independent of the velocity of the fluid and the pellet size. However, at low velocities, the mass transfer boundary layer is thick so the diffusion may still limit the reaction. By increasing the linear velocity, the boundary layer thickness will decrease so the mass transfer is enhanced. For a certain velocity, external mass transfer limitation can be enhanced by using small particles. However, smaller particles lead to higher pressure drop in a fixed bed reactor. Therefore, the reaction should be operated at sufficiently high velocities with sufficiently small particles to ensure sufficient external mass transfer.

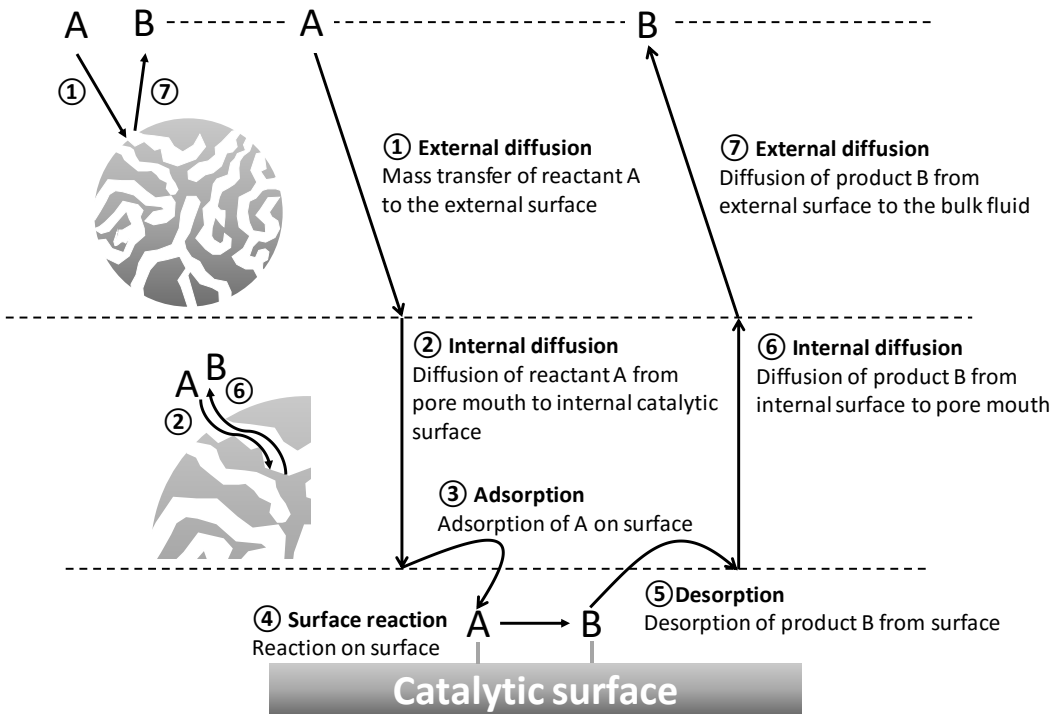

Scheme 1.4. The stages of heterogeneous reactions.

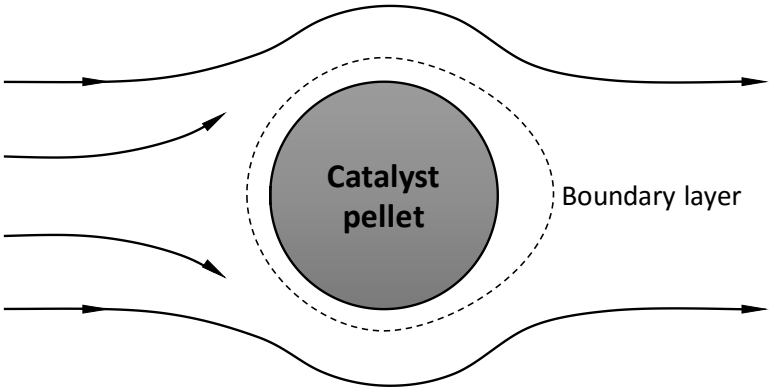

Figure 1.8. Transport and the boundary layer around the surface of a catalyst pellet.

Stage ② and ⑥ are internal diffusions related to the pore size of the catalyst and the kinetic diameters of the reactants and the products. Generally, the external diffusion limitation occurs at low temperature, under high

temperature conditions, a total pressure difference across the pore usually presents, generating a forced flow in pores[103]. There are three types of internal diffusion: molecular diffusion, Knudsen diffusion and single-file diffusion (**Figure 1.9**). Normally, the powder of the zeolites are compressed to form pellets so that the pressure drop is not too great in the industrial applications, the compression of the powders creates a new network of pores forming inter-granular voids, which should also be considered for the internal mass transfer[104].

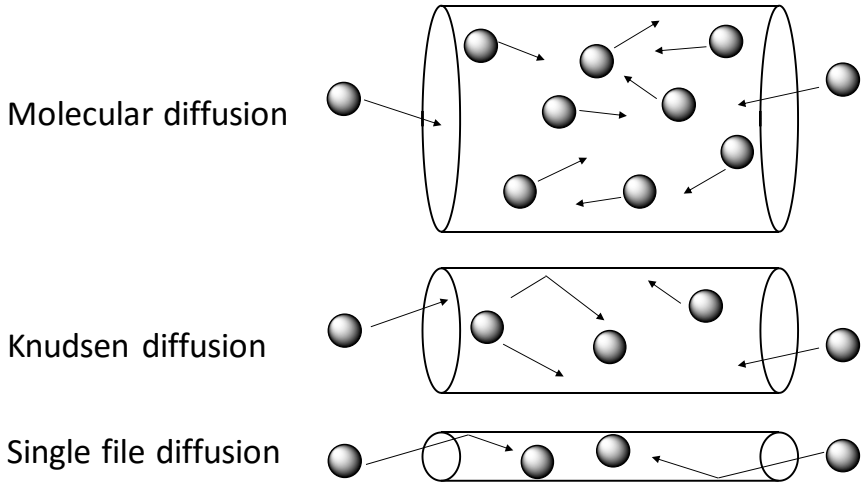

Figure 1.9. Diffusivity of gas phase molecules.

Stage ③, ④ and ⑤ are the core parts of the kinetic study in a catalytic reaction. **Figure 1.10** shows the overall energy profile during the catalytic reaction.

The adsorption can be physically or chemically. Physisorption, also called physical adsorption, is achieved by a van der Waals interaction between the sorbate and the surface[105,106] while chemisorption generates new chemical bonds[107,108]. The interaction of physisorption is weaker than chemisorption. Normally, typical enthalpies of chemisorption are much greater (in the region of 200 kJ mol^{-1}) than physisorption (in the region of 20 kJ mol^{-1})[109].Desorption process is the reverse of sorption, which is usually discussed together with adsorption.

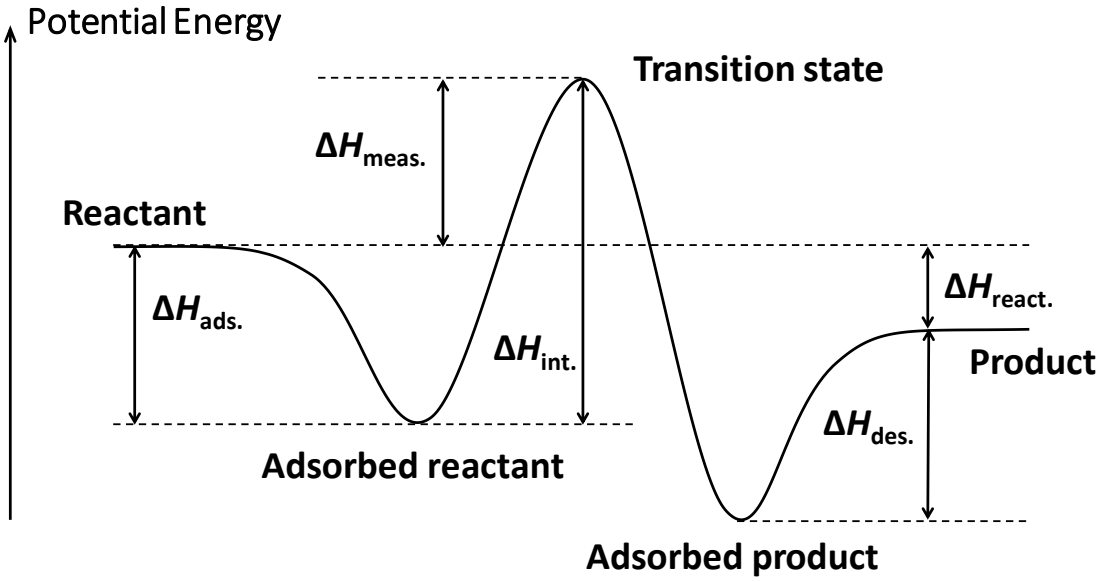

Figure 1.10. Energy diagram of a catalytic reaction.

Different models for adsorption have been established and described through isotherms, that is, the variation of the fractional coverage of the surface with the pressure of the adsorbate at a certain temperature. The most often used models include Langmuir isotherm, BET isotherm, etc.

The Langmuir isotherm is widely used to study the process of adsorption. Inherent within this model, there are three basic assumptions[109]:

(1) Adsorption cannot proceed beyond monolayer coverage.

(2) All sites are equivalent and the surface is uniform (that is, the surface is perfectly flat on a microscopic scale).

(3) The ability of a molecule to adsorb at a given site is independent of the occupation of neighbouring sites (that is, there are no interactions between adsorbed molecules).

Upon these assumptions, a mono-site Langmuir adsorption isotherm under equilibrium can be derived as:

$$\theta = \frac{K^{\ominus} \cdot p}{1 + K^{\ominus} \cdot p} \qquad \textbf{(Equation 1.1)}$$

where θ is the fractional occupation of the surface sites, p is the partial pressure of sorbate and $K^{\ominus}$ denotes equilibrium constant of adsorption.

If the initial layer of the sorped adsorbate can act as a substrate for further adsorption, then multilayer adsorption will proceed at high pressures. The isotherm mostly used for this multilayer adsorption was derived as the BET isotherm[110]:

$$V = \frac{V_{mon.} \cdot c \cdot p}{(p_0 - p) \cdot \{1 + (c-1) \cdot (p/p_0)\}} \qquad \textbf{(Equation 1.2 a)}$$

which can be reformed into:

$$\frac{p}{V \cdot (p_0 - p)} = \frac{1}{V_{mon.} \cdot c} + \frac{c-1}{V_{mon.} \cdot c} \cdot \frac{p}{p_0} \qquad \textbf{(Equation 1.2 b)}$$

where V and $V_{mon.}$ are the total adsorbed volume and the volume of the monolayer adsorbed gas, p and p_0 are the equilibrium and the saturation pressure of adsorbates, c is the BET constant:

$$c = e^{(\Delta H^{\ominus}_{des.} - \Delta H^{\ominus}_{vap.})/RT} \qquad \textbf{(Equation 1.3)}$$

where $\Delta H_{des.}^{\ominus}$ is the enthalpy of desorption from the initial sorbed monolayer, $\Delta H_{vap.}^{\ominus}$ is the enthalpy of vaporization of the liquid adsorbate, R is gas constant and T *is* absolute temperature. BET isotherms are widely used to determine the surface areas of solid with the adsorption of N_2.

Other isotherms such as Freundlich Isotherm, Temkin isotherm, etc. are also commonly used over restricted conditions[111], which will not be discussed in details here.

Heterogeneous catalysis normally depends on at least one reactant being adsorbed on the catalyst surface. For heterogeneous catalytic reactions, three types of mechanism are commonly defined in respect to the surface steps (**Figure 1.11**)[109]:

(1) Langmuir-Hinshelwood mechanism (LH mechanism)

Molecular fragments and atoms first adsorb on the surface of the catalyst and the surface catalyzed reaction takes place by encounters between these adsorbed species (**Figure 1.11 a**). Therefore, the expected rate law for a bimolecular reaction is derived as **Equation 1.4** in the extent of surface coverage:

$$A + B \longrightarrow P \qquad v = k\theta_A\theta_B \qquad \textbf{(Equation 1.4)}$$

If A and B follow Langmuir isotherms and adsorb without dissociation, then

$$\theta_A = \frac{K_A^{\ominus} p_A}{1+K_A^{\ominus} p_A+K_B^{\ominus} p_B} \qquad \theta_B = \frac{K_B^{\ominus} p_B}{1+K_A^{\ominus} p_A+K_B^{\ominus} p_B} \qquad \textbf{(Equation 1.5)}$$

so that the rate law is

$$v = \frac{k K_A^{\ominus} K_B^{\ominus} p_A p_B}{\left(1+K_A^{\ominus} p_A+K_B^{\ominus} p_B\right)^2} \qquad \textbf{(Equation 1.6)}$$

where k is rate constant, K_A and K_B are the equilibrium constant of adsorption for A and B, p_A and p_B are the partial pressure of A and B.

(2) Eley-Rideal mechanism (ER mechanism)

A gas-phase species react with another species already adsorbed on the surface (**Figure 1.11 b**). Then the expected rate law should be:

$$A + B \longrightarrow P \qquad v = k\theta_A p_B \qquad \textbf{(Equation 1.7)}$$

If the adsorption isotherm for A is given and follows a Langmuir isotherm in the pressure range of interest, then the rate law is:

$$v = \frac{kK^{\ominus} p_A p_B}{1 + K^{\ominus} p_A} \qquad \textbf{(Equation 1.8)}$$

(3) Mars van Krevelen mechanism

The reactant adsorbs on the surface and react with the lattice components such as O, S, Cl and H (**Figure 1.11 c**). The vacancy created by desorption of the product is refilled by the corresponding gas-phase components.

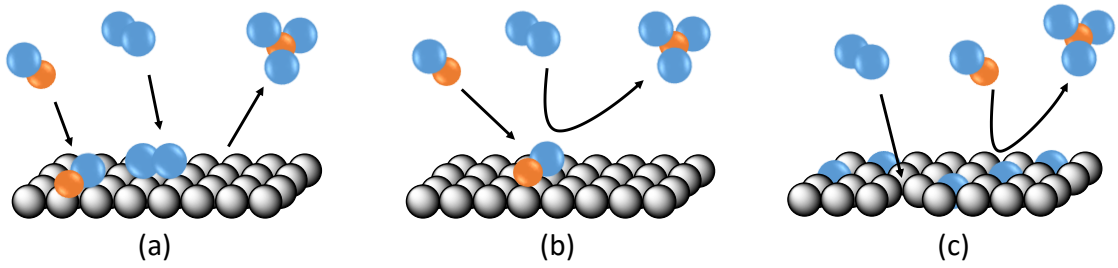

Figure 1.11. (a) Langmuir-Hinshelwood mechanism, (b) Eley-Rideal mechanism and (c) Mars van Krevelen mechanism.

For each mechanism, there is a specific equation for the rate law so when studying the surface reactions, it is crucial to first identify the reaction mechanism.

During the reaction process, it is hard to examine all the details of what the atoms and molecules are undergoing. However, it is widely accepted that they can collide and combine to form an unstable, high-energy complex[112]. This is the starting point of the transition state theory. The transition state theory (TST) is an attempt to explain the reaction constant of elementary chemical reactions. There are several approaches to the calculation and one of the most important approach is the Eyring equation[113,114]. Eyring equation describes changes in the reaction rate against temperature. The most common form of the equation is:

$$k=\frac{\kappa k_B T}{h}\exp(\frac{-\Delta^{\ddagger}G^{\ominus}}{RT})=\frac{\kappa k_B T}{h}\exp(\frac{-\Delta^{\ddagger}H^{\ominus}}{RT}+\frac{\Delta^{\ddagger}S^{\ominus}}{R}) \qquad \textbf{(Equation 1.9)}$$

where k is rate constant, κ is transmission coefficient (in the absence of information to the contrary, κ is assumed to be about 1), k_B is Boltzmann's constant, T *is* absolute temperature, h is Planck's constant, R is gas constant, $\Delta^{\ddagger}G^{\ominus}$ is Gibbs free energy of activation, $\Delta^{\ddagger}H^{\ominus}$ is enthalpy of activation and $\Delta^{\ddagger}S^{\ominus}$ is entropy of activation. This statement is usually based on a linearized form:

$$\ln\frac{k}{T}=\frac{-\Delta^{\ddagger}H^{\ominus}}{R}\cdot\frac{1}{T}+\ln\frac{\kappa k_B}{h}+\frac{\Delta^{\ddagger}S^{\ominus}}{R} \qquad \textbf{(Equation 1.10)}$$

Thus by plotting ln (k/T) versus 1/T, $\Delta^{\ddagger}H^{\ominus}$ and $\Delta^{\ddagger}S^{\ominus}$ can be obtained from the slope and the intercept, respectively[115].

1.2.2 Protolytic cracking of alkanes

Protolytic cracking of medium-range fractions of petroleum over acidic catalysts is responsible for the majority of manufacture of gasoline in the world[53]. The typical conditions for a catalytic cracking are under normal pressure and the temperature range is from 450 °C to 550 °C. Currently, Y zeolites and ZSM-5 are the two mostly employed catalysts in industry.

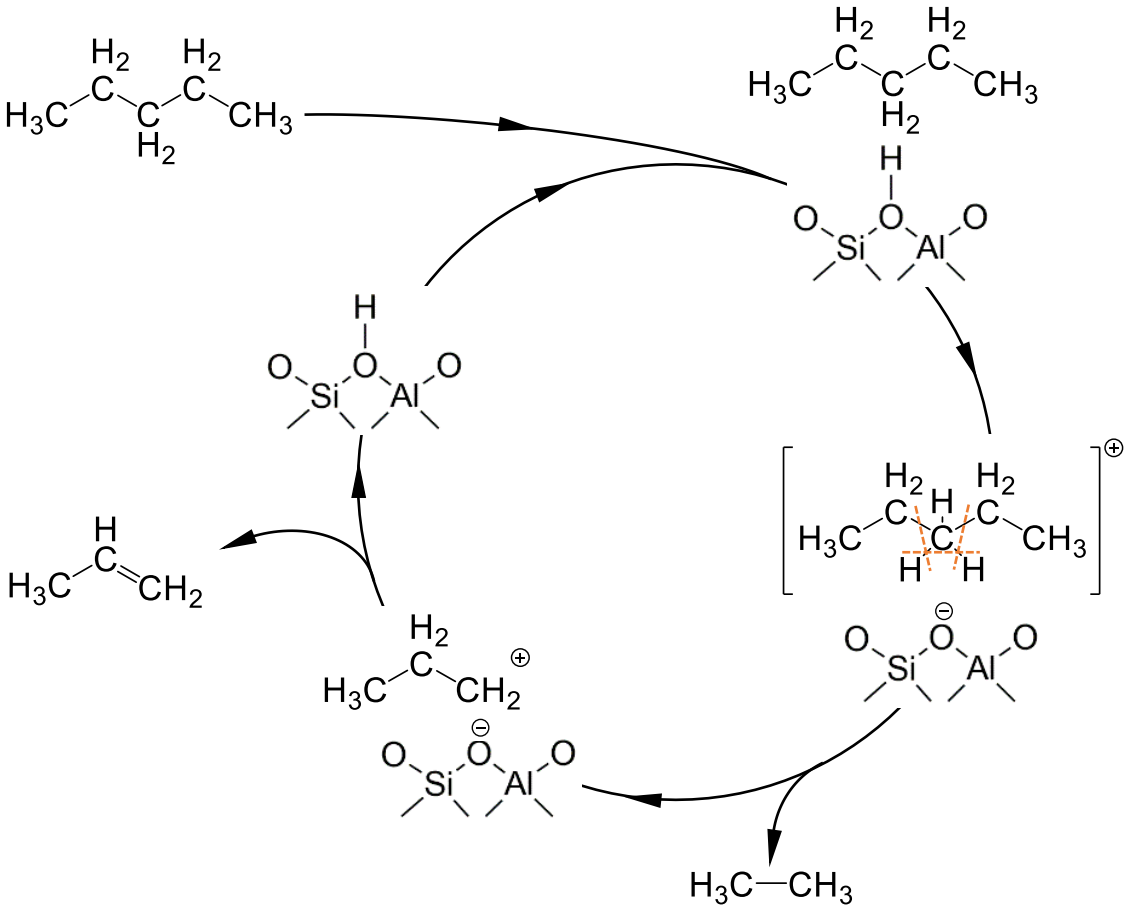

Scheme 1.5. Elementary steps of protolytic cracking of n-pentane on zeolites.

Studies of alkane cracking over acidic catalysts have demonstrated that alkanes are cracked and dehydrogenated via a monomolecular mechanism at low alkane partial pressures with low conversions[116]. Under these conditions, the reaction is first order in the alkane partial pressure and no diffusional transport effects exist for small alkanes such as n-hexane[117,118]. Therefore, monomolecular cracking of alkanes are ideal kinetic models for the study of intrinsic activity of these reaction on BAS.

Over ZSM-5 zeolite, the protolytic cracking follows a first order kinetic rate law[119]. The elementary steps (taking n-pentane cracking as an example) and the energy scheme involved in catalytic cracking of alkanes are shown in **Scheme 1.5** and **Figure 1.12**. The reaction starts with the adsorption of the gas-phase

alkane molecules on the BAS followed by the formation of the transition state. It is widely accepted nowadays that the transition state during a monomolecular cracking is a penta-coordinated carbonium ion according to the Haag-Dessau mechanism[116,119–121]. The Haag-Dessau mechanism provides that the BAS in zeolites are able to protonate the alkanes in an analogous way as inorganic super acids[122]. Following the carbonium ion formation, a molecule of alkane or H_2 formed under the cleavage of C – C or C – H bond and at the same time form a carbenium ion. The carbenium ion then turns to an olefin and closes the reaction cycle.

In a first order alkane cracking reaction, the measured reaction rate can be presented as:

$$\ln\frac{k_{meas.}}{T}=\frac{-\Delta H_{meas.}}{R}\cdot\frac{1}{T}+\ln\frac{\kappa k_B}{h}+\frac{\Delta S_{meas.}}{R} \qquad \textbf{(Equation 1.11)}$$

then the measured activation enthalpy and entropy can be obtained following:

$$rate_{meas.}=k_{meas.}\cdot p_{alkane} \qquad \textbf{(Equation 1.12)}$$

the intrinsic activation enthalpy and entropy can be calculated using **Equation 1.13**:

$$\Delta^{\ddagger}H_{int.}=\Delta H_{meas.}+\Delta H^{\ominus}_{ads.} \qquad \textbf{(Equation 1.13 a)}$$

$$\Delta^{\ddagger}S_{int.}=\Delta S_{meas.}+\Delta S^{\ominus}_{ads.} \qquad \textbf{(Equation 1.13 b)}$$

where $rate_{meas.}$ is the measured rate of the reaction, $k_{meas.}$ is the measured rate constant, p_{alkane} is the partial pressure of the alkane, $\Delta H_{meas.}$ is the measured enthalpy of activation, $\Delta S_{meas.}$ is the measured entropy of activation, $\Delta^{\ddagger}H_{int.}$ is

intrinsic enthalpy of activation and $\Delta S_{int.}$ is intrinsic entropy of activation, $\Delta H^{\Theta}_{ads.}$ is the adsorption enthalpy of alkane, which can be measured using calorimetry and $\Delta S^{\Theta}_{ads.}$ is the adsorption entropy of alkane, which can be calculated by **Equation 1.14**:

$$\Delta S^{\Theta}_{ads.} = \frac{\Delta H^{\Theta}_{ads}}{T} + R\ln(K^{\Theta}_{ads.}) \qquad \textbf{(Equation 1.14)}$$

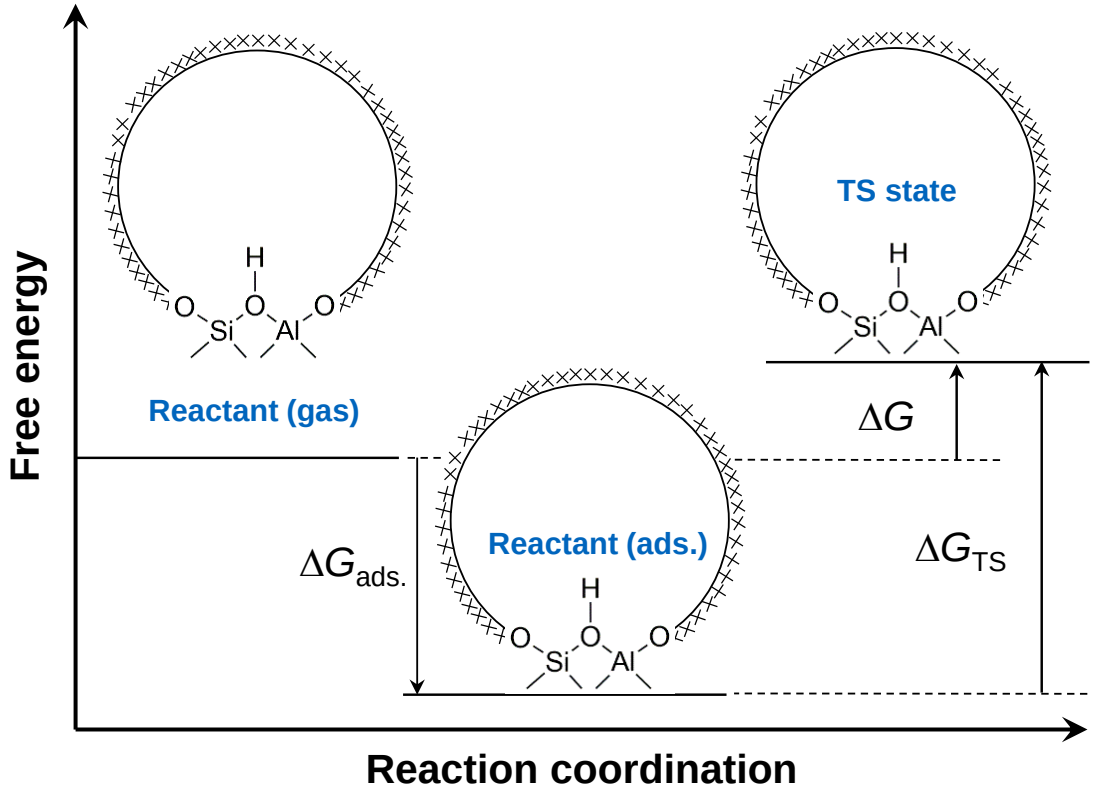

Figure 1.12. Energy scheme for protolytic cracking on zeolites.

The cracking rate increases exponentially with increasing carbon number of the alkane and over different framework types[51,123–125]. However, Narbeshuber et al. found that the intrinsic barrier of alkane cracking is independent of the chain length (**Table 1.1**)[124]. Moreover, the independency of intrinsic barrier of alkane was also found over different framework types, for example, the intrinsic

activation barriers for monomolecular propane cracking over MOR, FER, MFI, USY, BEA, FAU and MWW zeolites are comparable as 199 ± 11 kJ mol^{-1} [126]. Therefore, the changes on different chain lengths and different frameworks illustrate the role of confinement and entropy in the reaction. For the cracking reaction with increasing chain length over the same zeolite framework, an increment of adsorption energy (~12 kJ mol^{-1} per CH_2 group on H-MFI zeolites) is observed because of the larger number of van der Waals contacts between the alkane molecules and the confining voids[127,128]. This results in an entropy loss of the adsorption and leads to an additional entropy gain of the transition state consequently. A similar effect can be derived for the same cracking reaction over different zeolite frameworks, the partial confinement of the transition state due to a narrow voids (e.g., 8-MR side pocket compared to 12-MR channel) results in a significantly entropy gain, which in turn is responsible for the enhancement of the reaction activity[125].

Table 1.1. Heats of adsorption, apparent and intrinsic energies of activation of n-alkanes cracking over H-ZSM-5 at 773K[124].

Reactant	Heat of adsorption (kJ mol^{-1})	Apparent energy of activation (kJ mol^{-1})	Intrinsic energy of activation (kJ mol^{-1})
Propane	43	155	198
n-Butane	62	135	197
n-Pentane	74	120	194
n-Hexane	92	105	197

1.2.3 Promotion of cracking activity by extra framework Al

Cracking activity is sensitive to the environment around the BAS. A marked promotion effect has been found in the presence of extra-framework Al (EFAl)[48,63,89,129–133]. While some reports attribute this to an increased acid strength of BAS by the presence of EFAl[63,64,134,135], recent work from us[89,129] and some others[136–139] addressed the confined space under the proximity of EFAl to

BAS, which stabilizes the reaction transition states via a higher activation entropy[129].

Schallmoser et al. found that the catalytic activity of n-pentane cracking over MFI zeolites increased with increasing concentration of aluminium leading to increasing concentration of strong Brønsted acid sites (SBAS)[89]. There is a linear relationship between the normalized rate and the concentration of strong Brønsted acid sites for the samples with lower Al content (SBAS concentration lower than 400 μmol g^{-1}), while samples with higher SBAS concentration show conspicuous higher activity per SBAS indicating that a certain fraction of the SBAS is highly active. The higher activities on these samples are attributed to the extraframework Al species, which was proved by the constant normalized reaction rates after the selective removal of EFAl (**Figure 1.13** left).

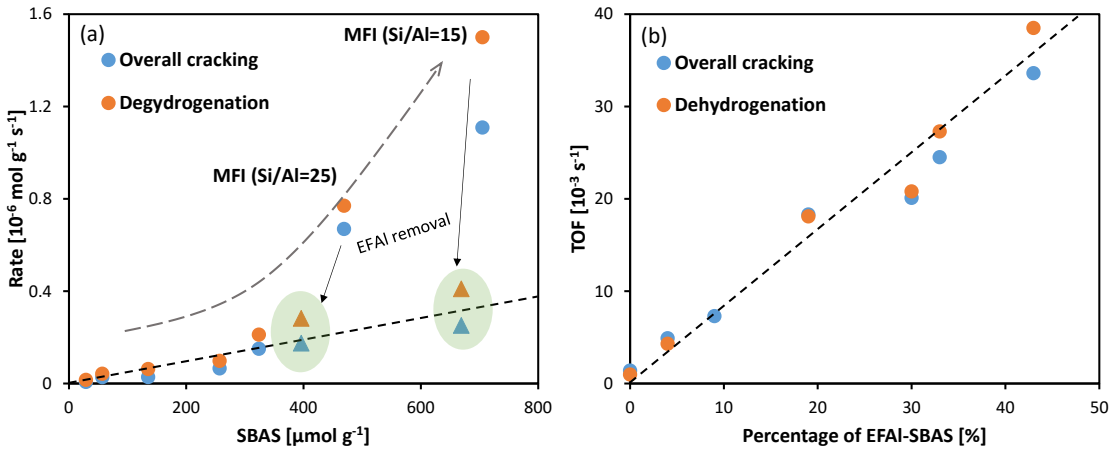

Figure 1.13. (a) Impact of AHFS modification on n-pentane cracking and dehydrogenation rates over MFI zeolites with different Si/Al ratios (adapted from Ref.[89], rounded symbols for the rates on MFI zeolites without EFAl removal and triangle symbols for the rates on MFI zeolites after EFAl removal) and (b) the promotion effect of n-pentane cracking and dehydrogenation over MFI zeolites by EFAl (adapted from Ref.[129]).

Following this study, Zhang el al. confirmed the proximity of EFAl and SBAS using infrared spectroscopy with pyridine adsorption and found that the promotion effect on the turnover frequency of n-pentane cracking and

dehydrogenation follows a linear relationship with the fraction of EFAl-SBAS paired sites (**Figure 1.13** right)[129]. The rates of overall cracking and dehydrogenation on EFAl-SBAS paired sites are 52- and 84-times higher than that on isolated SBAS. These enhancements are attributed to the stabilization of the transition states via a higher activation entropy related to a later transition state.

1.2.4 Studies on extra framework Si (EFSi)

Compared to the extensive studies on extra framework Al, there are few studies on Si as an extra framework species. As mentioned before, post treatments of Si are mostly used to block the BAS on the external surface or the pore mouth to increase reaction selectivity or create mesopores[140]. However, these modifications did not influence the BAS in the zeolite micropores. Here, inspired by the effect of EFAl, we decided to extend and probe the strategy for modifying BAS by alumina nanoclusters (EFAl)[141–145] by replacing EFAl with EFSi within a BAS environment and postulate that EFSi will also alter the properties of BAS.

1.3 Scope of the thesis

Even though the promotion effect on EFAl on catalytic cracking reaction is addressed to the more confined space leading a higher transition entropy, there is still argument due to the fact that EFAl as Lewis acidity could also provide additional effects as synergy. Therefore, silica cluster as a more neutral species is the optimal substitution to study the pure constrain effect by extra framework species in vicinity to the BAS.

It is hypothesized that an insertion of silica clusters into zeolite micropore channels, in particular close to BAS, are to induce changes in the chemical environment of the BAS, altering its intrinsic properties by confinement for

catalytic reactions. Therefore, to have an understanding of the influence of EFSi species in vicinity of BAS, the present study will be established as follows.

Initially, a new Si modification method is developed using silylamine molecule as the Si precursor to graft extra framework Si species in the vicinity of the Brønsted acid sites. In order to clarify the loading and the location of these extra framework Si species, various characterization methods (IR, elemental analysis, etc.) will be used. This modification method is turned out to be controllable on the location and the loading of Si clusters, which is enlightening to the graft of extensive species to a targeting location in the zeolite pores.

Then the adsorption property of zeolite in the presence of EFSi will be studied using different probe molecules. With this information, we try to reveal how the EFSi species influence the chemical environment around the BAS.

To elucidate the role of EFSi in catalytic activity, n-pentane cracking is selected as a model reaction. The elementary steps of this reaction including adsorption, different reaction pathways through different transition states will be discussed in details. The activation enthalpy and entropy will be determined and a transition-states-mimicking method using alkyl aminium ions will be used to explain the energy change of the reaction with the existence of EFSi.

Chapter 2. Experimental

2.1 Chemicals and materials

All the chemicals and materials were obtained from commercial suppliers and used as received if no special treatment is mentioned (**Table 2.1**).

Table 2.1. Chemicals and materials.

Chemical / material	Formula	Purity	CAS #	Manufacturer
NH_4-MFI (CBV 2314)	-	-	-	Zeolyst-International
Ammonia hexafluorosilicate	$(NH_4)_2SiF_6$	98%	16919-19-0	Sigma-Aldrich
n,n-Dimethyl-trimethyl-silylamine	$(CH_3)_3SiN(CH_3)_2$	95%	2083-91-2	Alfa Aesar
Hexane	$CH_3(CH_2)_4CH_3$	≥97.0%	110-54-3	Sigma-Aldrich
Pyridine	C_5H_5N	99.8%	110-86-1	Sigma-Aldrich
Ammonia	NH_3	≥99.9%	7664-41-7	Linde
n-Pentane	$CH_3(CH_2)_3CH_3$	≥99.0%	110-86-1	Sigma-Aldrich
n-Methylpropylamine	$CH_3CH_2CH_2NHCH_3$	96%	627-35-0	Sigma-Aldrich
Diethyl ether	$(CH_3CH_2)_2O$	≥99.7%	60-29-7	Sigma-Aldrich
Water	H_2O	Distilled	7732-18-5	Homemade
Diethylamine	$(C_2H_5)_2NH$	≥99.5%	109-89-7	Sigma-Aldrich
Synthetic air	-	-	-	Westfalen
Nitrogen	N_2	99.9%	7727-37-9	Westfalen

2.2 Sample preparation

2.2.1 Removal of extra-framework aluminum

NH_4-MFI (CBV 2314) with SiO_2/Al_2O_3 = 23 was dealuminated with $(NH_4)_2SiF_6$ (ammonia hexafluorosilicate, AHFS) to remove extra-framework Al (EFAl), following the procedure as previously reported[89]. NH_4-MFI was added to a solution of $(NH_4)_2SiF_6$ at 353 K (approximately 1 g catalyst per 40 ml solution) and then stirred for 5 h. The solution contained 3.2-fold excess of AHFS with respect to the Al content of the zeolite, which was 2.84 g (16 mmol) AHFS for 3.84 g NH_4-MFI (3.8 wt. % Al corresponding to 5 mmol). Afterwards, the sample was separated and washed with hot deionized water (over 353 K) for six times and calcined in a steam of synthetic air (100 ml min^{-1}, heating rate 10 K min^{-1}, 823 K) for 5 h. The obtained sample was in hydrogen form and designated as H-MFI.

2.2.2 Si grafting by silylamine post treatment

Extra-framework silica (EFSi) was introduced into H-MFI by adsorbing n,n-dimethyltrimethylsilylamine followed by calcination. The H-MFI (approx. 1 g sample per 5 ml solution) was added to a hexane solution of $(CH_3)_3SiN(CH_3)_2$ at room temperature and stirred overnight. Different EFSi loading is achieved by controlling the amount of $(CH_3)_3SiN(CH_3)_2$. For example, on EFSi-MFI-46% sample, the corresponding amount of $(CH_3)_3SiN(CH_3)_2$ in the solution was 300 µmol per gram H-MFI, which was 0.185 g (1.5 mmol) $(CH_3)_3SiN(CH_3)_2$ for 5 g H-MFI. Afterwards, the solid sample was washed three times with hexane and calcined in 100 ml min^{-1} air for 10 h at 823 K with a heating rate 1 K min^{-1}. The obtained material was designated as EFSi-MFI-X% (X% corresponding to the portion of EFSi-BAS on the samples).

The Si grafting is supposed to be conducted via a two-step process, adsorbing n, n-dimethyltrimethylsilylamine $(CH_3)_3SiN(CH_3)_2$ on BAS followed by calcination in air at 823 K (**Scheme 2.1**).

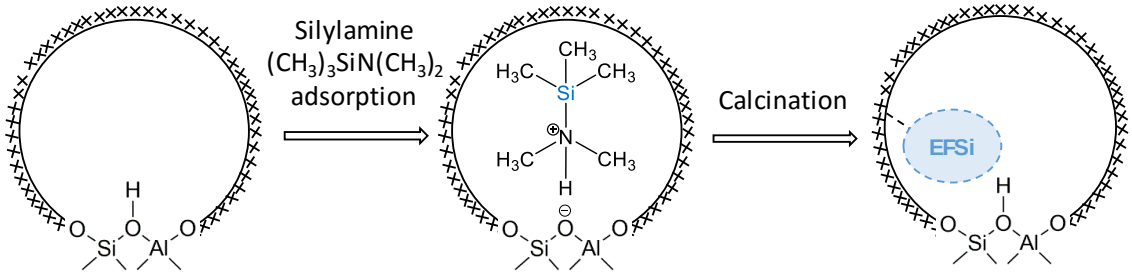

Scheme 2.1. EFSi introducing by adsorbing n, n-dimethyltrimethylsilylamine $(CH_3)_3SiN(CH_3)_2$ on BAS followed by calcination.

2.3 Catalyst characterization

2.3.1 X-ray diffraction

X-ray diffraction measurements were performed on a *Malvern Panalytical* X-ray diffractometer operating in the reflection mode with Cu-Kα radiation (45 kV, 40 mA). The measurements were carried out with the range of 2θ from 5 to 70 °.

2.3.2 Nitrogen physisorption

Specific surface area and micropore volume were determined from N_2 adsorption/desorption isotherms measured at liquid N_2 temperature (77 K) on an automated *PMI Sorptomatic 1990* instrument. The samples were outgassed in vacuum at 723 K for 2 h before the adsorption. The specific surface areas were calculated applying the Brunauer-Emmett-Teller (BET) theory and the pore volumes were determined by the t-plot method.

2.3.3 Elemental analysis

The elemental composition of the samples was determined by atomic absorption spectroscopy in a *Unicam M Series Flame-AAS* equipped with an *FS 95* auto-sampler and a *GF 95* graphite furnace. Samples were dissolved in a mixture of hydrofluoric acid (48%) and nitrohydrochloric acid at its boiling point prior to the measurements.

2.3.4 Titration of acid sites with pyridine

IR spectroscopy was used to determine the acid site concentrations of zeolites with pyridine as the probe molecule. All spectra were collected at 423 K on a *Nicolet 5700* FT-IR spectrometer. Zeolites were pressed into wafers and pre-treated in vacuum ($p < 10^{-5}$ mbar) at 723 K for 1 h. Then they were exposed to a pulse of ~ $3 \cdot 10^{-2}$ mbar pyridine for 10 min. After outgassing for 20 min to remove physisorbed pyridine, a spectrum was collected. A series of spectra under different BAS coverage were received by repeating this procedure until all the BAS had been titrated by pyridine. The concentration of total BAS was quantified based on the area of the band at 1545 cm^{-1} normalized to the wafer weight[146]. With a known integrated molar extinction coefficient of 0.73 cm μmol^{-1} for the band 1545 cm^{-1}, the integrated molar extinction coefficient for BAS-OH at 3610 cm^{-1} can be calculated from the slope of the peak area decrease of 3610 cm^{-1} as a function of the peak area increase of 1545 cm^{-1} on H-MFI, which is measured to be 2.65 cm μmol^{-1}.

2.3.5 Titration of acid sites with ammonia

IR spectroscopy was used to determine the acid site concentrations of zeolites with ammonia (NH_3) as the probe molecule. All spectra were collected at 423 K on a *Nicolet 5700* FT-IR spectrometer. Zeolites were pressed into wafers and pre-treated in vacuum ($p < 10^{-5}$ mbar) at 723 K for 1 h. Then they

were exposed to a pulse of ammonia for 10 min. After outgassing for 20 min to remove physisorbed ammonia, a spectrum was collected. A series of spectra under different BAS coverage were received by repeating this procedure until all the BAS had been titrated by ammonia.

Temperature programmed desorption (TPD) of NH_3 was performed in a 6–fold parallel reactor system. The solid catalysts were activated in vacuum at 723 K with a heating rate of 10 K min^{-1} for 1 h. NH_3 was adsorbed with a partial pressure of 1 mbar at 353 K. Subsequently, the samples were outgassed in vacuum for 2 h to remove physisorbed molecules. For the TPD measurement, the samples were heated up in vacuum from 353 to 1033 K with a temperature increment of 10 K min^{-1} to desorb NH_3. The desorbed NH_3 (channel m/z =17) were monitored by mass spectrometry (*Balzers QME 200*). For acid site quantification, a reference (HZSM-5 with Si/Al = 45 from Clariant) with known acidity (400 µmol g^{-1}) was used to calibrate the signal.

2.3.6 Adsorption of n-pentane

The adsorption isotherms of n-pentane on H-MFI and EFSi-MFIs were measured gravimetrically in a *Seteram TG-DSC 111* calorimeter connected to a high vacuum system. About 20 mg of the corresponding sample was placed in a quartz sample holder and activated at 723 K for 1 h under vacuum ($p < 10^{-4}$ mbar) with a heating rate of 10 K min^{-1}. After the samples were cooled to 333 K, n-pentane was introduced into the system by controllably dosing. The adsorbed n-pentane was determined in small pressure steps from $1 \cdot 10^{-2}$ to 40 mbar. The n-pentane uptake was determined by the increase of sample weight, and the released heat was obtained by integration of the heat flux signal.

The adsorption isotherms were analyzed in terms of a Langmuir adsorption model (**Equation 2.1**):

$$n = \frac{n_{max} \cdot K_{ads}^{\ominus} \cdot p}{1 + K_{ads}^{\ominus} \cdot p} \qquad \textbf{(Equation 2.1)}$$

where n is the amount of sorbate on the sample, n_{max} is the maximum uptake of sorbate, $K^{\ominus}_{ads}$ denotes equilibrium constant of adsorption and p is the normalized pressure (referred to p^0 = 1 bar).

The adsorption entropy ($\Delta S^{\ominus}_{ads}$) was calculated using van't Hoff type equation as **Equation 2.2**:

$$\Delta S^{\ominus}_{ads} = \frac{\Delta H^{\ominus}_{ads}}{T} + R \cdot \ln K^{\ominus}_{ads} \qquad \textbf{(Equation 2.2)}$$

where $\Delta S^{\ominus}_{ads}$ is standard adsorption entropy, $\Delta H^{\ominus}_{ads}$ is standard adsorption enthalpy, T is the absolute temperature and R is the universal gas constant.

IR spectra was conducted to evaluate pentane adsorption on a *Bruker Optics Vertex 70* spectrometer at a resolution of 4 cm^{-1}. Samples were prepared as self-supporting wafers and outgassed in vacuum ($p < 10^{-5}$ mbar) at 723 K for 1 h with a heating rate of 10 K min^{-1}. After cooling to 333 K, n-pentane was introduced into the system by controllably dosing. The adsorbed n-pentane was determined in small pressure steps from $1 \cdot 10^{-2}$ to 10 mbar. A series of spectra were collected under different pressure of n-pentane until all the BAS had been perturbed.

2.3.7 Adsorption of N-methylpropylamine and diethylamine

The adsorption of N-methylpropylamine and diethylamine on H-MFI and EFSi-MFI were also measured gravimetrically on a microbalance in a *Seteram TG-DSC 111* calorimeter connected to a high vacuum system. After pre-treatment of 20 mg samples at 723 K for 1 h under vacuum ($p < 10^{-4}$ mbar), the sample was cooled to 423 K. Afterwards, N-methylpropylamine or diethylamine was introduced into the system as pulses. By controlling the dosing pressure and

exposure time, approximately 0.08 mmol $mmol_{BAS}^{-1}$ was adsorbed in each pulse. The amine uptake was determined by the increase of sample weight and the released heat was obtained by integration of the heat flux.

IR spectra of adsorbed N-methylpropylamine and diethylamine was used to identify their adsorption site and the formed species on H-MFI and EFSi-MFI. All spectra were collected at 423 K on a *Vertex 70* spectrometer from *Bruker Optics*. Zeolite wafers were loaded into a homemade IR cell connected to a vacuum system. It was first pre-treated in vacuum ($p < 10^{-5}$ mbar) at 723 K for 1 h and cooled to 423 K. Then it was exposed to a pulse of $\sim 3 \cdot 10^{-2}$ mbar N-methylpropylamine or diethylamine for 10 min. After outgassing for 20 min to remove physisorbed amine, a spectrum was collected. A series of spectra under different uptake were received by repeating this procedure until all the BAS had been covered.

2.3.8 Adsorption of diethyl ether, water and methanol

Adsorption measurements of diethyl ether, water and methanol were conducted on a *Nicolet 5700* FT-IR spectrometer. Zeolites were pressed into wafers and pre-treated in vacuum ($p < 10^{-5}$ mbar) at 723 K for 1 h. For diethyl ether and methanol, the measurements were performed at 333 K. A series of spectra were collected under different pressure by controllable dosing. For water adsorption, spectra were collect at 423 K under different water partial pressure inside the infrared cell.

2.4 Catalytic reaction of n-pentane cracking

The protolytic cracking of n-pentane on H-MFI and EFSi-MFIs was conducted in a tubular flow reactor with a quartz tube with an internal diameter of 7 mm at ambient pressure. Catalyst pellets (300-500 µm) were activated in situ at 803 K with a heating ramp of 2 K min^{-1} for 2 h in 20 ml min^{-1} of synthetic air and then flushed for 30 min with 20 ml min^{-1} N_2. Reactant liquid stream was

introduced into the reactor via an evaporator and then mixed with N_2. The reaction was carried out in the temperature range between 753 and 793 K. Reactant and products were analyzed by online chromatographic measurements (*Superlco Q-Plot*, capillary column: 30 m × 0.53 mm × 2.0 μm) using an FID detector.

The reaction turnover frequency (TOF) was normalized to overall-BAS concentration of the formation of products.

The first order activation enthalpies ($\Delta H_{1st}^{\ddagger\Theta}$) and entropies ($\Delta S_{1st}^{\ddagger\Theta}$) were calculated from Eyring equation (**Equation 2.3**):

$$\ln\frac{k_{1st}h}{k_B T} = -\frac{\Delta H_{1st}^{\ddagger\Theta}}{R}\cdot\frac{1}{T} + \frac{\Delta S_{1st}^{\ddagger\Theta}}{R} \qquad \textbf{(Equation 2.3)}$$

where k_{1st} is the first order rate constant, k_B is Boltzmann's constant, T is absolute temperature, h is Planck's constant, R is gas constant.

Chapter 3. Synthesis, identification and quantification of EFSi-BAS and its adsorption properties.

3.1 Synthesis, identification and quantification of EFSi-BAS

3.1.1 The presence of EFSi

Extra framework silica was grafted in H-MFI pores via a two-step process. Initially, the amine group directs the silylamine $(CH_3)_3SiN(CH_3)_2$ to selectively interact with BAS forming aminium ion. This was concluded from the decrease of the intensity of the IR band assigned to the SiOHAl group (BAS-OH) at 3610 cm^{-1} and the appearance of the respective C-H vibration as well as N-H vibration band at 2300-3350 cm^{-1} and 1620 cm^{-1} on the IR spectra of the sample exposed to silylamine (**Figure 3.1 a** and **b**). Then the organic part of the precursor was completely removed during the following calcination in a stream of synthetic air, shown by the disappearance of C-H and N-H vibration bands in the IR spectra (**Figure 3.1 c**), linking the silica species on lattice oxygen not associated with BAS.

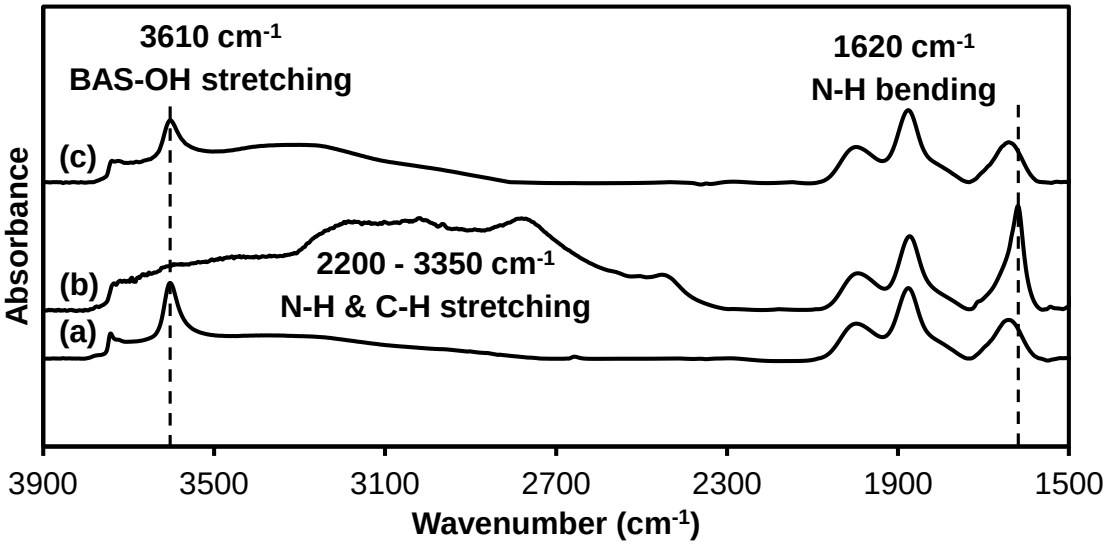

Figure 3.1. IR spectra for samples during EFSi grafting. (a) H-MFI, (b) H-MFI with adsorbed n,n-dimethyltrimethylsilylamine $(CH_3)_3SiN(CH_3)_2$ (65% loading corresponding to the Al content) and (c) after calcination to EFSi-MFI-61%. (Spectra taken at 423 K.)

It is noticeable that EFSi-MFI-61% sample (spectra c in **Figure 3.1**, with a theoretical EFSi loading of 65% corresponding to the Al content during the grafting treatment) showed no 3610 cm^{-1} band in the IR spectrum before calcination. This indicates that all the bridging SiOHAl groups (3610 cm^{-1}) were perturbed by the silylamine precursor at this point, leading a maximum EFSi loading for this grafting treatment.

The MFI samples before and after this EFSi-modification did not show differences in the X-ray diffractograms (**Figure 3.2**), the BET surface area is unchanged (374 ± 15 m^2 g^{-1}) and the micropore volume is unchanged (0.15-0.16 cm^2 g^{-1}) as well (**Figure 3.3**, **Table 3.1**). A small increase in the Si/Al ratio was observed with increasing EFSi grafting. This suggests that in addition to the pore modification, some extra crystalline Si species had been generated, as estimated by the small increase in the Si/Al ratio. These catalysts are denoted as EFSi-MFI-X% (X% for the portion of EFSi-BAS determined from pyridine titration in **Section 3.1.2**.

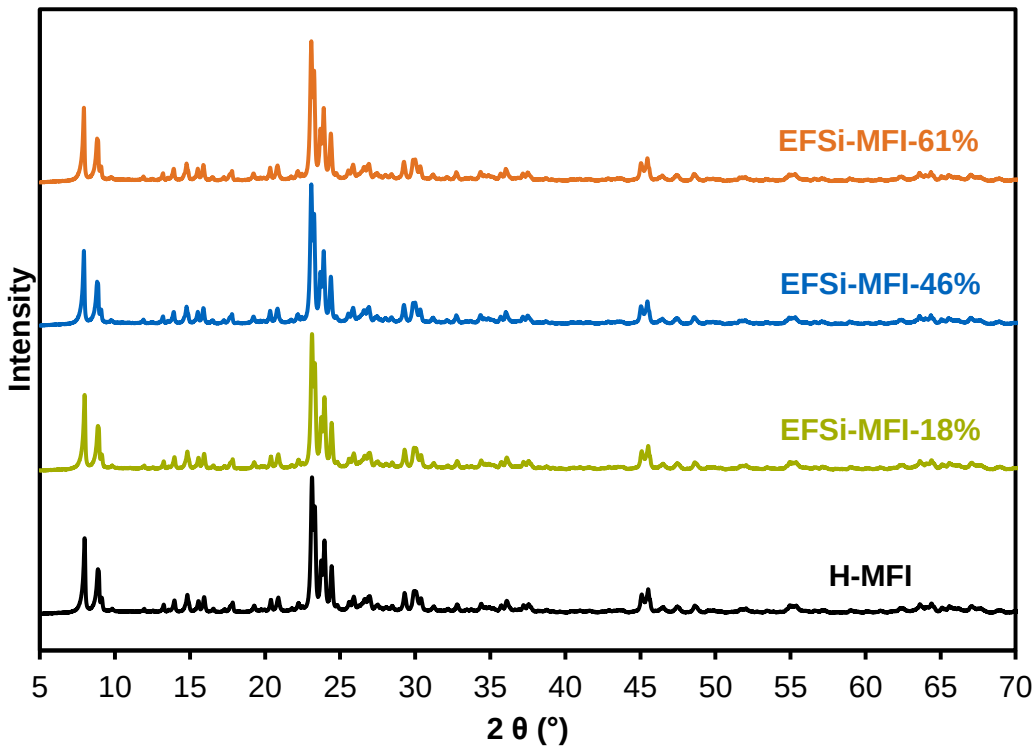

Figure 3.2. XRD patterns of H-MFI and EFSi-MFIs.

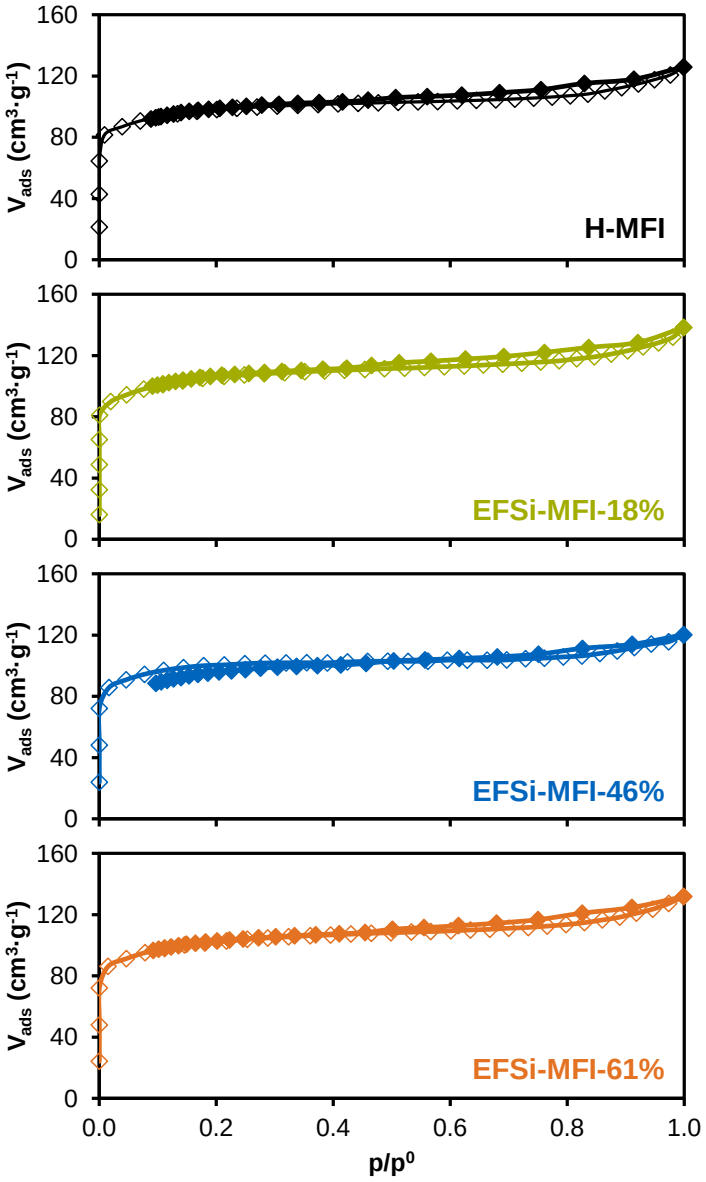

Figure 3.3. N_2 adsorption-desorption isotherms on H-MFI and EFSi-MFIs at 77 K.

Table 3.1. Physiochemical properties of H-MFI and EFSi-MFIs.

Sample	BET surface area ($m^2\ g^{-1}$)	Micropore volume ($cm^3\ g^{-1}$)	Si/Al	ΔSi/Al
H-MFI	359	0.15	24.6	-
EFSi-MFI-18%	388	0.16	24.7	0.1
EFSi-MFI-46%	370	0.15	25.1	0.5
EFSi-MFI-61%	374	0.15	25.3	0.7

The presence of the grafted EFSi was in a first step evaluated by infrared spectroscopy (**Figure 3.4**). In the OH stretching vibration region, the EFSi-MFI samples showed a higher intensity of the band at the wavenumber of 3720 cm^{-1}. This band is characteristic of the silanol (Si-OH) groups in the zeolite channels[147–149], proving the successful incorporation of EFSi into the micropores. The intensity of the band at 3610 cm^{-1} for bridging hydroxyl groups (SiOHAl groups, BAS-OH)[147,150] was lower for EFSi-MFI samples compared to H-MFI (**Figure 3.4**). This decrease is attributed either to a chemical blocking or to a perturbation of the BAS-OH groups by EFSi (**Scheme 3.1**), suggesting a close proximity between EFSi and BAS-OH groups. A new broad band between 3100 cm^{-1} to 3500 cm^{-1} suggests that the latter interpretation is more plausible and the broad band is tentatively assigned to a BAS-OH group weakly interacting with OH groups. The broadening of this band and the shift from 3610 cm^{-1} to 3100-3500 cm^{-1} are hypothesized to be caused by H-bonding between the BAS and the adjacent EFSi[151–153], which generally results in a decrease in the frequency accompanied by broadening and intensification of the band[154].

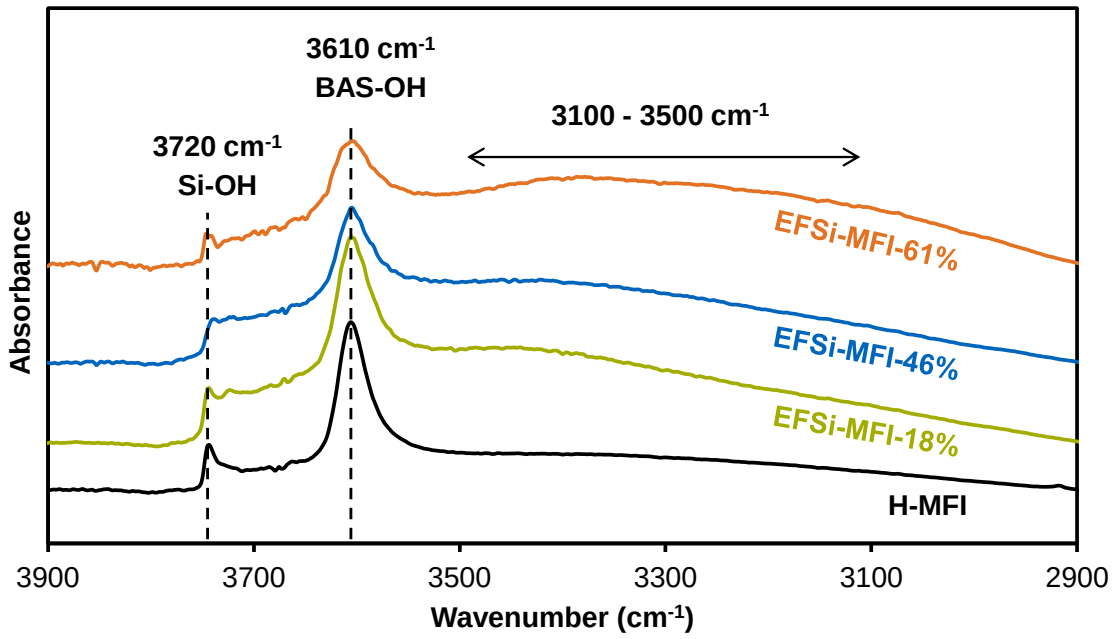

Figure 3.4. IR spectra of OH stretching vibration region of H-MFI and EFSi-MFIs.

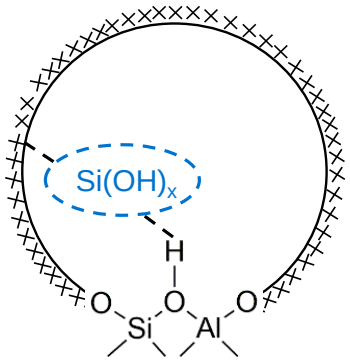

Scheme 3.1. BAS perturbed by a neighboring EFSi.

To exclude the possibility of chemically anchoring this group at the oxygen of the BAS, i.e., that the $Si(OH)_x$ replaces the proton of the bridging hydroxyl group linking an Al-O tetrahedron, pyridine adsorption was followed conducted in the next section.

3.1.2 Quantification of BAS and EFSi-BAS on EFSi-MFIs

Figure 3.5 shows the IR spectra of H-MFI and EFSi-MFIs with varying concentrations of adsorbed pyridine. With the exposure of H-MFI to aliquots of pyridine, the characteristic band of SiOHAl groups (BAS-OH 3610 cm^{-1}) decreased and concomitantly the band of pyridinium ion (HPy^+ 1545 cm^{-1}) appeared and increased in intensity (**Figure 3.5 a**). The decrease of the BAS-OH band (the concentration of the BAS that are interacting with pyridine) and the intensity of the HPy^+ band (the concentration of the pyridinium ions) for H-MFI were directly proportional (**Figure 3.5 e**). This suggests that pyridine adsorbs on all BAS forming a pyridinium ion with a stoichiometry of one pyridinium ion per BAS[71].With this, the integrated molar extinction coefficient for the vibrational band of BAS-OH at 3610 cm^{-1} is calculated to be 2.65 cm μmol^{-1}, 3.63 times higher than that of HPy^+ at 1540 cm^{-1} (0.73 cm μmol^{-1}).

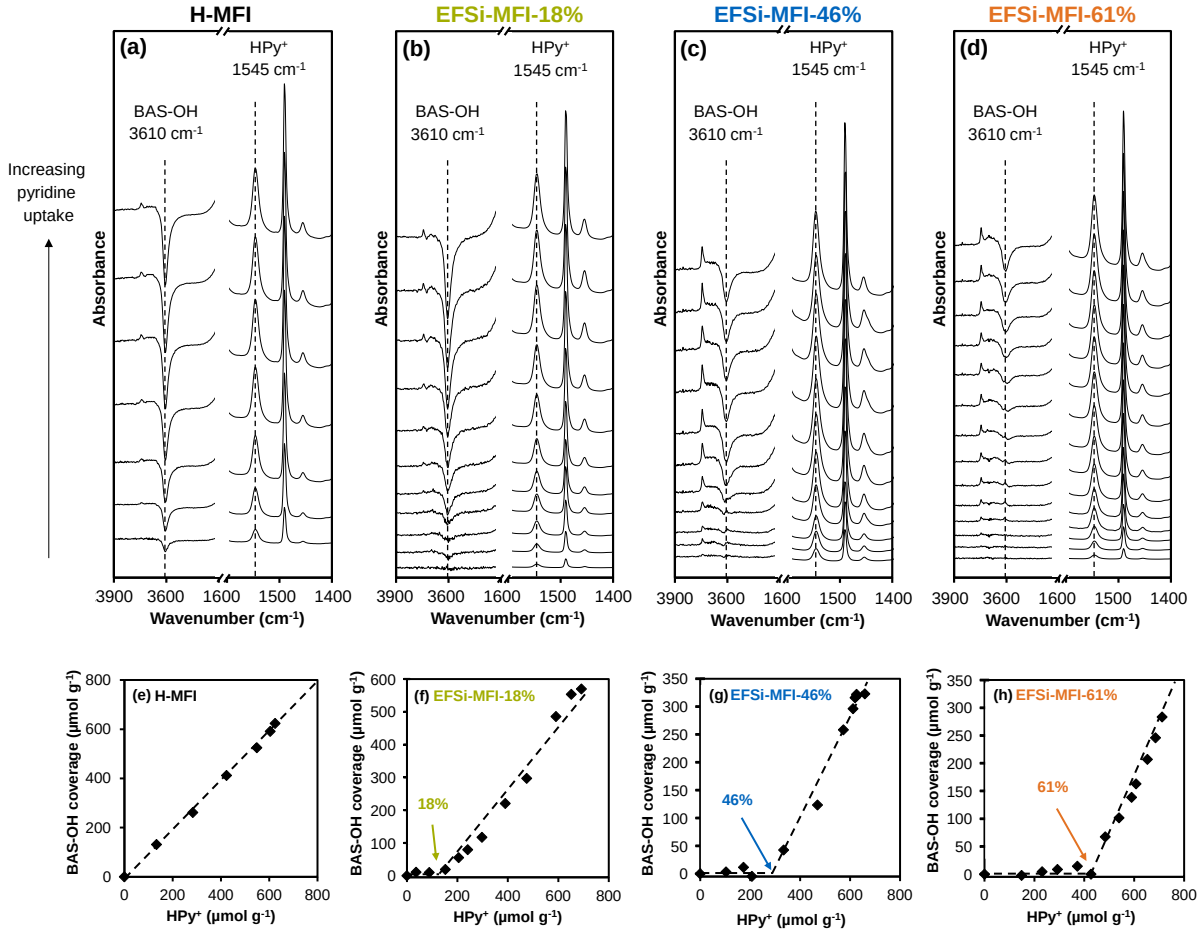

Figure 3.5. Pyridine adsorption on H-MFI and EFSi-MFIs. Difference IR spectra of OH stretching and NH bending vibration region for (a) H-MFI and (b) – (d) EFSi-MFIs with increasing pyridine uptake at 423K; BAS-OH (3610 cm^{-1}) coverage under different HPy^+ concentrations on (e) H-MFI and (f) – (h) EFSi-MFIs. (HPy^+ concentration determined from the peak area of 1545 cm^{-1} band; BAS-OH coverage determined from the peak area of 3610 cm^{-1} band.)

In contrast, the adsorption of pyridine on EFSi-MFIs exhibited two different regimes. Taking EFSi-MF-61% as an example, after the first aliquots of pyridine adsorbed, the band of the SiOHAl groups (BAS-OH) remained unchanged up to the formation of 430 µmol g^{-1} of HPy^+ (**Figure 3.5 d**). Only subsequently, the BAS-OH band began to decrease in intensity. The coverage of BAS-OH, (i.e., the decrease in intensity) increased then linearly with the HPy^+ concentrations, following a 1:1 ratio (**Figure 3.5 h**). EFSi-MFI-18% (**Figure 3.5 b** and **3.5 f**) and EFSi-MFI-46% (**Figure 3.5 c** and **3.5 g**) samples followed the same trend with the turning thresholds at 121 µmol g^{-1} and 294 µmol g^{-1} of HPy^+. These concentrations are equal to the theoretical EFSi loading during the Si grafting treatment (130 μmol_{Si} g^{-1} on EFSi-MFI-18%, 300 μmol_{Si} g^{-1} on EFSi-MFI-46% and 460 μmol_{Si} g^{-1} on EFSi-MFI-61%).

These two adsorption regimes suggest two different types of BAS on EFSi-MFI. Pyridine first adsorbed on the BAS having an adjacent EFSi (**Scheme 3.2 a**), this type of BAS was attributed to the EFSi-BAS. This EFSi-BAS site does not exhibit a BAS-OH band at 3610 cm^{-1}. The second regime was identical to the normal BAS, as observed with the parent H-MFI (**Scheme 3.2 b**). Thus in this regime, each adsorbed pyridine formed a HPy^+ and reduced proportionately the intensity of the BAS-OH band at 3610 cm^{-1}. The concentrations of EFSi-BAS and BAS were quantified by the corresponding pyridine uptake in the two regimes (**Figure 3.5 e-h**), *i. e*., on EFSi-MFI-61% sample, the first 430 µmol g^{-1} HPy^+ were formed on EFSi-BAS and the latter 280 µmol g^{-1} HPy^+ were on normal BAS. The concentrations of EFSi-BAS and BAS on all samples are summarized in **Table 3.2**. All these results allow to conclude that the EFSi species are not chemically bound to Brønsted acid sites, but rather break up a Si-O-Si bridge forming a silanol nest with the $Si(OH)_x$ group attached.

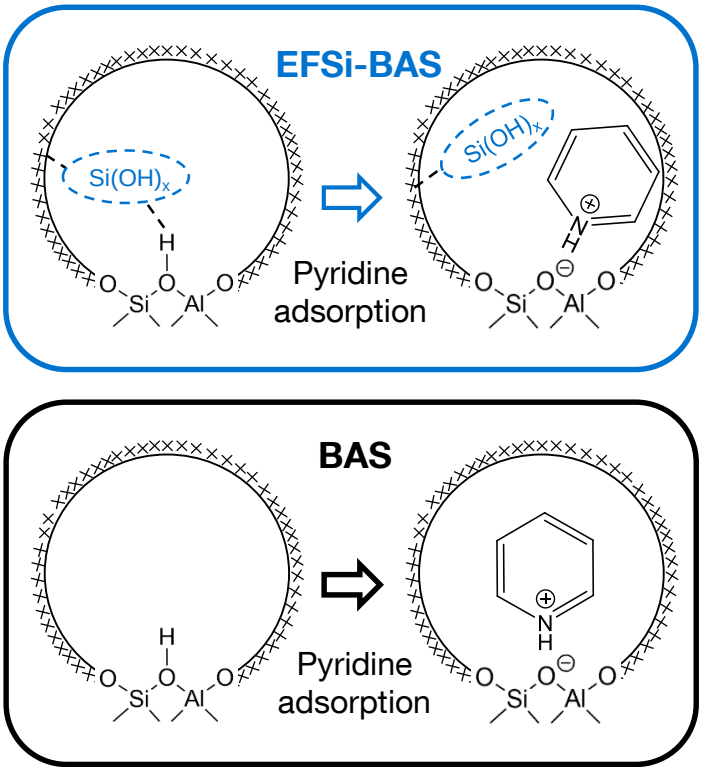

Scheme 3.2. Pyridine adsorption on (a) EFSi-BAS and (b) BAS.

Table 3.2. Acid site concentrations of H-MFI and EFSi-MFIs.

Sample	Acid site concentration (µmol g^{-1})			
	Overall BAS	BAS	EFSi-BAS	LAS
H-MFI	650	650	0	65
EFSi-MFI-18%	691	570	121 (18%)	90
EFSi-MFI-46%	640	346	294 (46%)	65
EFSi-MFI-61%	710	280	430 (61%)	72

3.2 Influence of EFSi on the adsorption properties

3.2.1 Acid strength of BAS and EFSi-BAS

The preferential adsorption of pyridine on EFSi-BAS discussed in **Section 3.1.2** may be attributed to: (1) stronger acid strength of EFSi-BAS comparing to normal BAS; (2) additional interaction between EFSi group and the aryl ring of pyridine molecule stabilizing the adsorbed state. To test the two possibilities, base molecules such as ammonia, diethylamine and N-methylpropylamine were employed as probe molecules to titrate the EFSi-BAS and normal BAS on EFSi-MFI-46%.

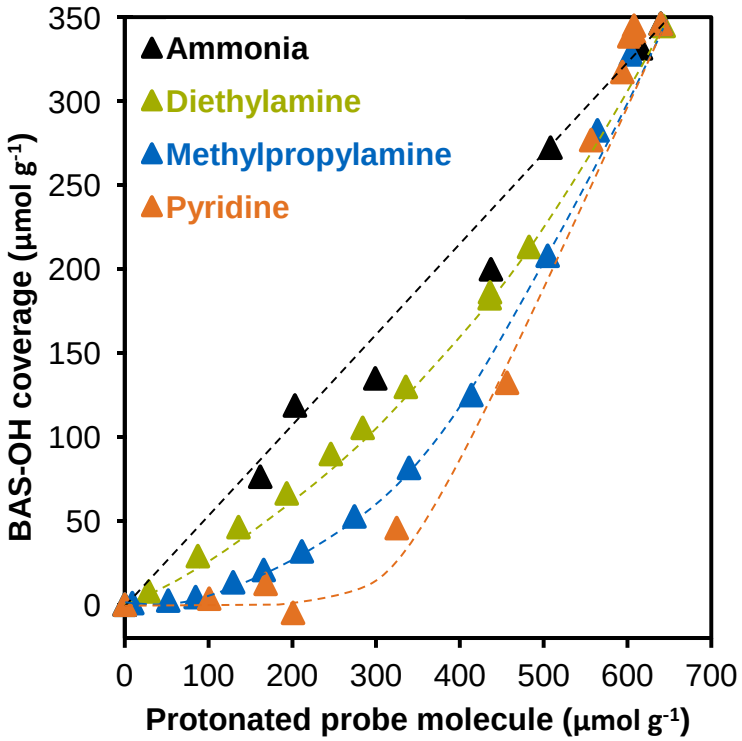

Figure 3.6. Ammonia, diethylamine, N-methylpropylamine and pyridine adsorption on EFSi-MFI-46% at 423 K. BAS-OH coverage (determined from the area decrease of band 3610 cm^{-1} on IR spectra) under different concentrations of protonated probe molecules, i.e. ammonium ion, diethylaminium ion, N-methylpropylaminium ion and pyridinium ion.

As shown in **Figure 3.6**, for ammonia adsorption, the BAS-OH coverage increased linearly with the concentration of formed ammonium ion (NH_4^+). This shows a simultaneously adsorption of ammonia on both BAS and EFSi-BAS, indicating the same acid strength of BAS and EFSi-BAS. This is further supported by NH_3-TPD results, which show the overlapping desorption curves of H-MFI, EFSi-MFI-18%, EFSi-MFI-46% and EFSi-MFI-61% (**Figure 3.7**).

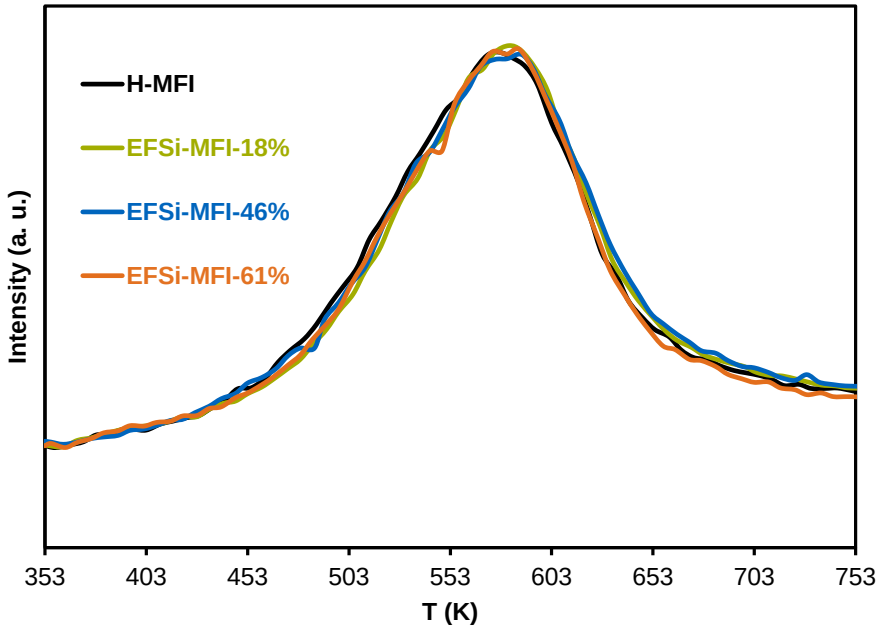

Figure 3.7. Temperature-programmed desorption of ammonia for all samples.

However, for base molecules with alkyl or aryl chains such as diethylamine, N-methylpropylamine and pyridine, the relation of BAS-OH coverage vs. the concentration of their protonated form deviates from linearity (**Figure 3.7**), indicating a preferential adsorption of these base molecules on EFSi-BAS. In particular, stronger preferential adsorption was found to be the more pronounced the bulkier the adsorbed base was, i.e., pyridine > N-methylpropylamine > diethylamine.

Combining these results leads to the conclusion that the presence of EFSi influences the environment of the BAS in proximity without changing the acid

strength. Such influence is speculated to be the result of additional van der Waals interactions between the EFSi and the organic alkyl/aryl chain of a guest molecule.

3.2.2 N-pentane adsorption on H-MFI and EFSi-MFI

To explore how the EFSi-BAS interacts with alkyl chains of an organic guest molecule, n-pentane as a sample of saturated hydrocarbon was adsorbed on H-MFI and EFSi-MFIs at 333 K and their IR spectra were used for characterization (**Figure 3.8** and **3.9**). On H-MFI (**Figure 3.8 a** and **3.9 a**), upon

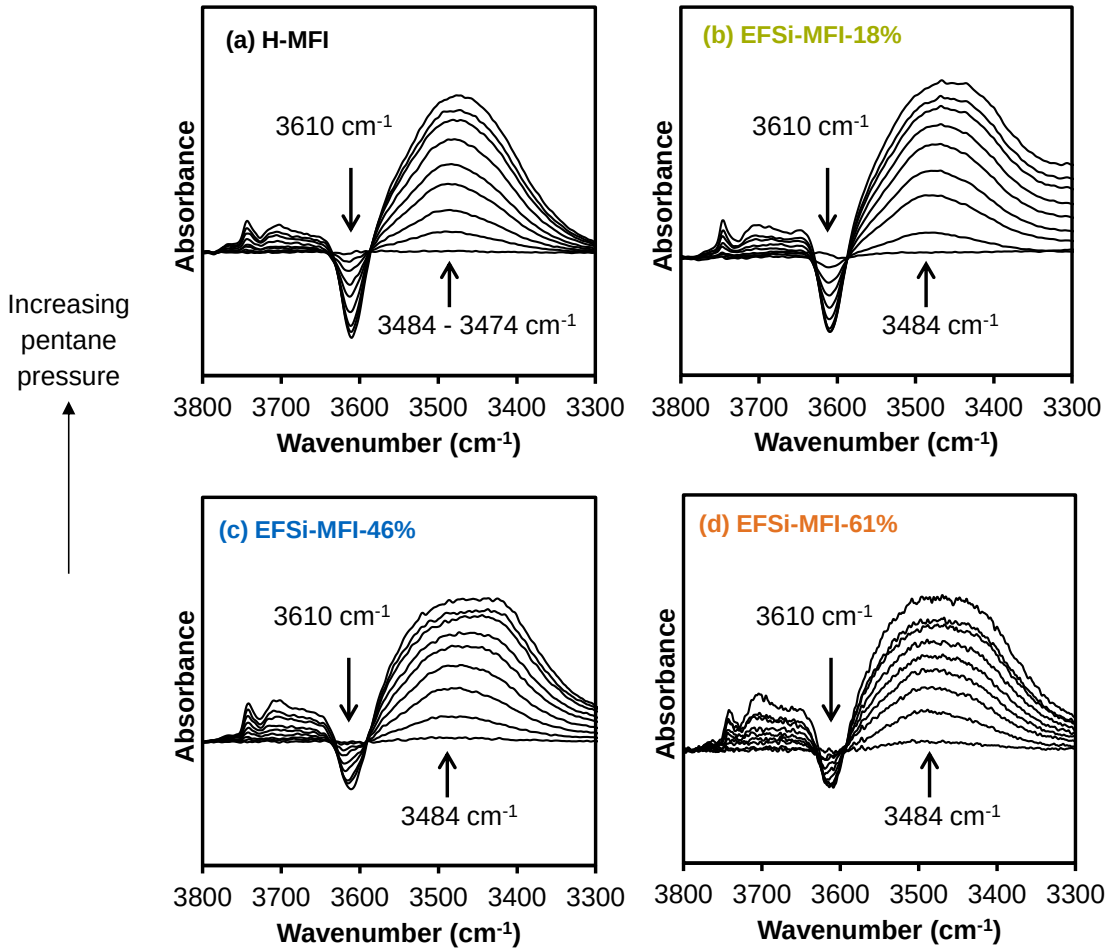

Figure 3.8. Pentane adsorption on H-MFI and EFSi-MFIs. Difference spectra of OH vibration region for with pentane adsorption at 333 K under different partial pressure.

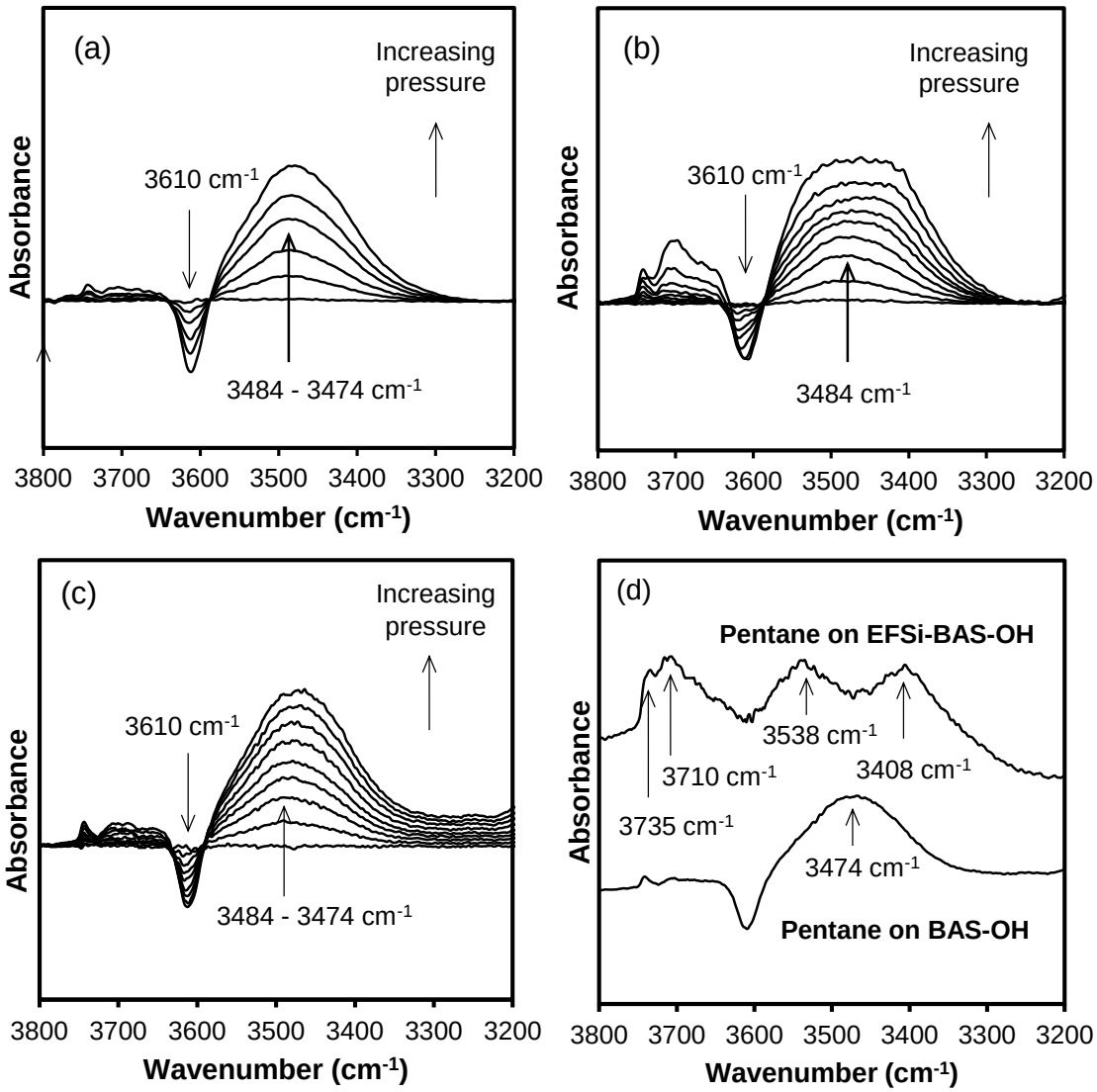

Figure 3.9. Difference spectra in OH stretching vibration region for (a) H-MFI, (b) EFSi-MFI-46% and (c) pre-pyridine-titrated EFSi-MFI-46% with sorbed pentane at 333 K under increasing pentane pressures up to the coverage* of ~346 µmol g-1 BAS-OH; (d) difference spectra between (b) and (c) showing the spectra of pentane on EFSi-BAS-OH, with the difference spectra of pentane on BAS-OH as reference. (*BAS-OH coverage determined from the peak area of 3610 cm^{-1} band.

n-pentane adsorption, the intensity of BAS-OH vibration at 3610 cm^{-1} decreased with increasing pentane pressure. Concurrently, a new band at 3484 cm^{-1} was observed. This band is attributed to the perturbed band of the BAS-OH interacting with n-pentane via hydrogen bonding. With increasing pressure, this

band gradually shifted to 3474 cm^{-1}, due to a stronger polarization of the bridging OH group by interaction with a second pentane molecule[128].

The decrease of BAS-OH band was also observed on EFSi-MFIs, however, the band centered at 3484 cm^{-1} was much broader and less intense compared to that on H-MFI (**Figure 3.8 b-d**). This implies the new bands from interaction of EFSi-BAS-OH and n-pentane partly overlaps with the band of BAS-OH with n-pentane in this region.

To distinguish the different perturbed O-H vibration bands with adsorbed pentane on EFSi-MFIs, a titration with pyridine was conducted to block all the EFSi-BAS in EFSi-MFI-46%. After that, only BAS in EFSi-MFI-46% was accessible to pentane, and it showed the band at 3484 cm^{-1}, which is identical to pentane adsorbed on the H-MFI sample (**Figure 3.9 c**).

The difference of the spectra with and without pyridine blocking EFSi-BAS allows to access the IR spectrum of the hydrogen bonding of n-pentane on EFSi-BAS (**Figure 3.9 d**). This difference spectra, of course, indicates that the adsorption of n-pentane on EFSi-BAS does not lead an intensity decrease of the band at 3610 cm^{-1}. This is simply because EFSi-BAS does not have this band. It shows, nevertheless, a pair of perturbed OH groups at 3408 cm^{-1} and 3538 cm^{-1}. These bands are attributed to the perturbed vibrations of bridge SiOHAl and Si-OH of the EFSi-BAS. It also shows a marked increase in the intensity of terminal Si-OH band at 3735 cm^{-1} and its perturbed band by n-pentane at 3710 cm^{-1} upon n-pentane adsorption on EFSi-BAS.

With these information, we propose the structure of EFSi-BAS constituted of a bridge SiOHAl interacting with geminal EFSi-OH via hydrogen bondings (**Scheme 3.3**). Prior to n-pentane adsorption, the geminal EFSi-OH and bridging SiOHAl forms a hydrogen bonding network, which red-shifts and broadens OH vibrational band and makes it hardly observable. The adsorbed n-pentane insert between the bridging SiOHAl group and the adjacent EFSi-OH, interrupting the hydrogen bonding network. It simultaneously perturbs both the vibration of the bridge SiOHAl and one EFSi-OH, inducing the band at 3408 cm^{-1} and 3538 cm^{-1}. The appearance of the bands at 3735 cm^{-1} or 3710 cm^{-1} are attributed to non-

interacting or very weakly interacting EFSi-OH groups. The lower wavenumber of the perturbed EFSi-BAS-OH vibration (3408 cm^{-1}), with respect to that of BAS-OH (3474 cm^{-1}), points to a stronger polarization of the EFSi-BAS-OH group by the adjacent EFSi.

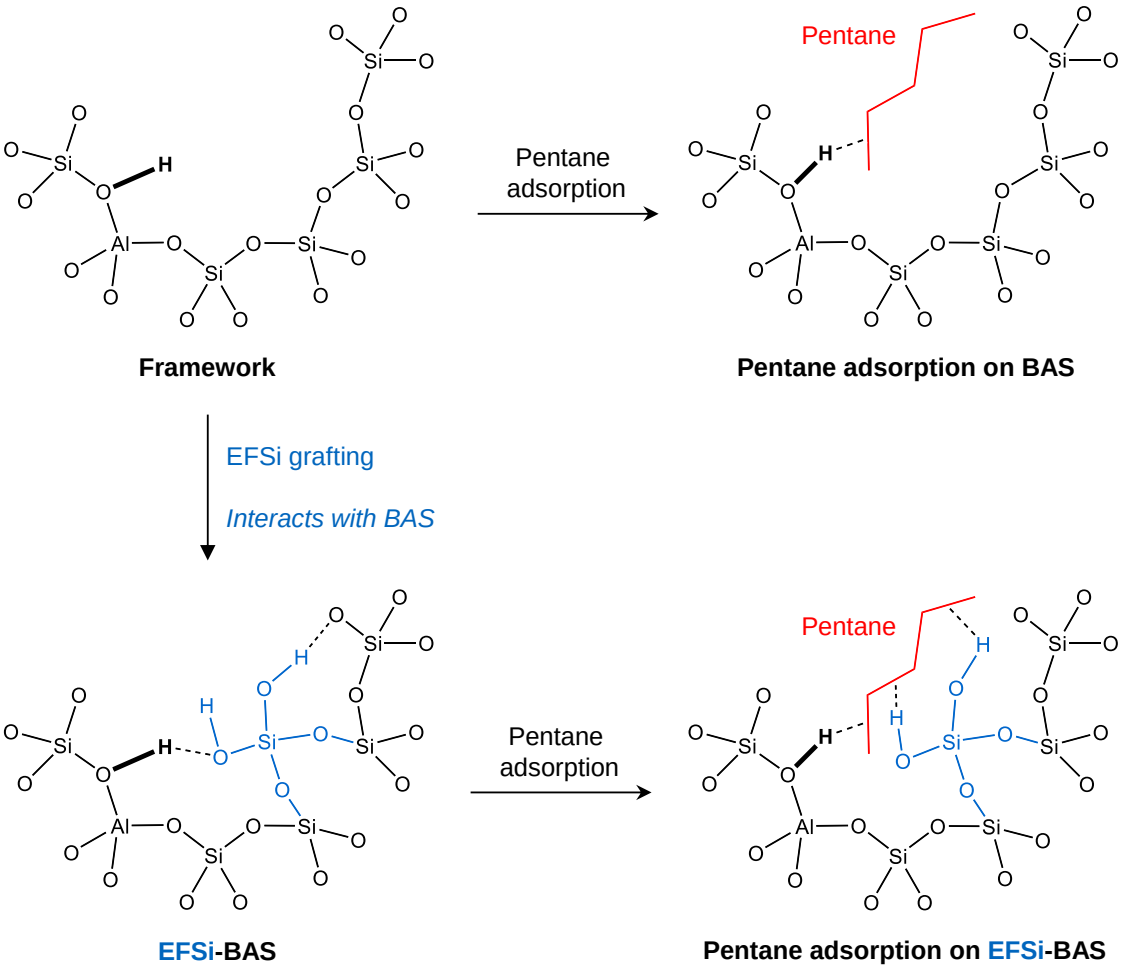

Scheme 3.3. The structure of grafted EFSi, EFSi-BAS and pentane sorption on BAS and EFSi-BAS.

3.2.3 N-methylpropylamine adsorption on H-MFI and EFSi-MFI

As discussed in **Section 3.1.2** and **3.2.1**, pyridine exhibits a two-regimes of adsorption on EFSi-MFIs (preferably adsorbs on EFSi-BAS and afterwards on BAS) while n-pentane adsorbs simultaneously on BAS and EFSi-BAS. This can be explained by the fact that the adsorption mechanism for n-pentane differs from pyridine. N-pentane adsorbs on the BAS dominantly by the Van der Waals force (i.e., about -12 kJ mol^{-1} per $–CH_2–$) along with a stabilizing interaction between the acid proton and the alkane molecule (i.e., -7 to -10 kJ mol^{-1} in H-ZSM-5)[127,155]. In general, a tighter fit of alkanes in zeolite pores leads to a stronger adsorption due to the higher contributions of the van der Waals interactions between the alkane and the zeolite. However, as a strong base, pyridine forms protonated pyridinium ion (HPy^+) with a positive charge on the BAS upon adsorption. The preferentially adsorption of pyridine on EFSi-BAS indicates that such an ion-paired form of HPy^+ and the negative charged zeolite structure (SiO^-Al) can be more stabilized by the EFSi in the vicinity of BAS.

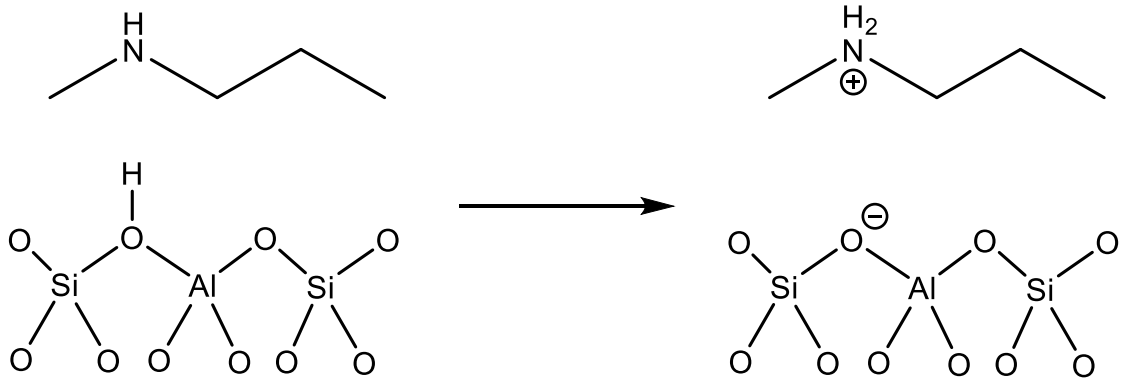

Scheme 3.4. N-methylpropylamine adsorption on the zeolitic BAS.

To prove this hypothesis, N-methylpropylamine adsorption was then conducted on H-MFI and EFSi-MFI-46% because of its similar chain structure to n-pentane and the same protonated adsorbed form on the BAS as pyridine

molecule (**Scheme 3.4**). **Figure 3.10** shows the IR spectra of H-MFI and EFSi-MFI-46% with varying adsorbed uptakes of N-methylpropylamine. On H-MFI, upon N-methylpropylamine titration, BAS-OH band (3610 cm^{-1}) decreased in intensity with a simultaneous increase in the N-H bending band at 1605 cm^{-1} for the N-H bending vibration (δNH_2) in N-methylpropylaminium ion[71,156–158] ($CH_3N^+H_2CH_2CH_2CH_3$, CN^+CCC for short, **Figure 3.10 a**). Plotting the BAS-OH

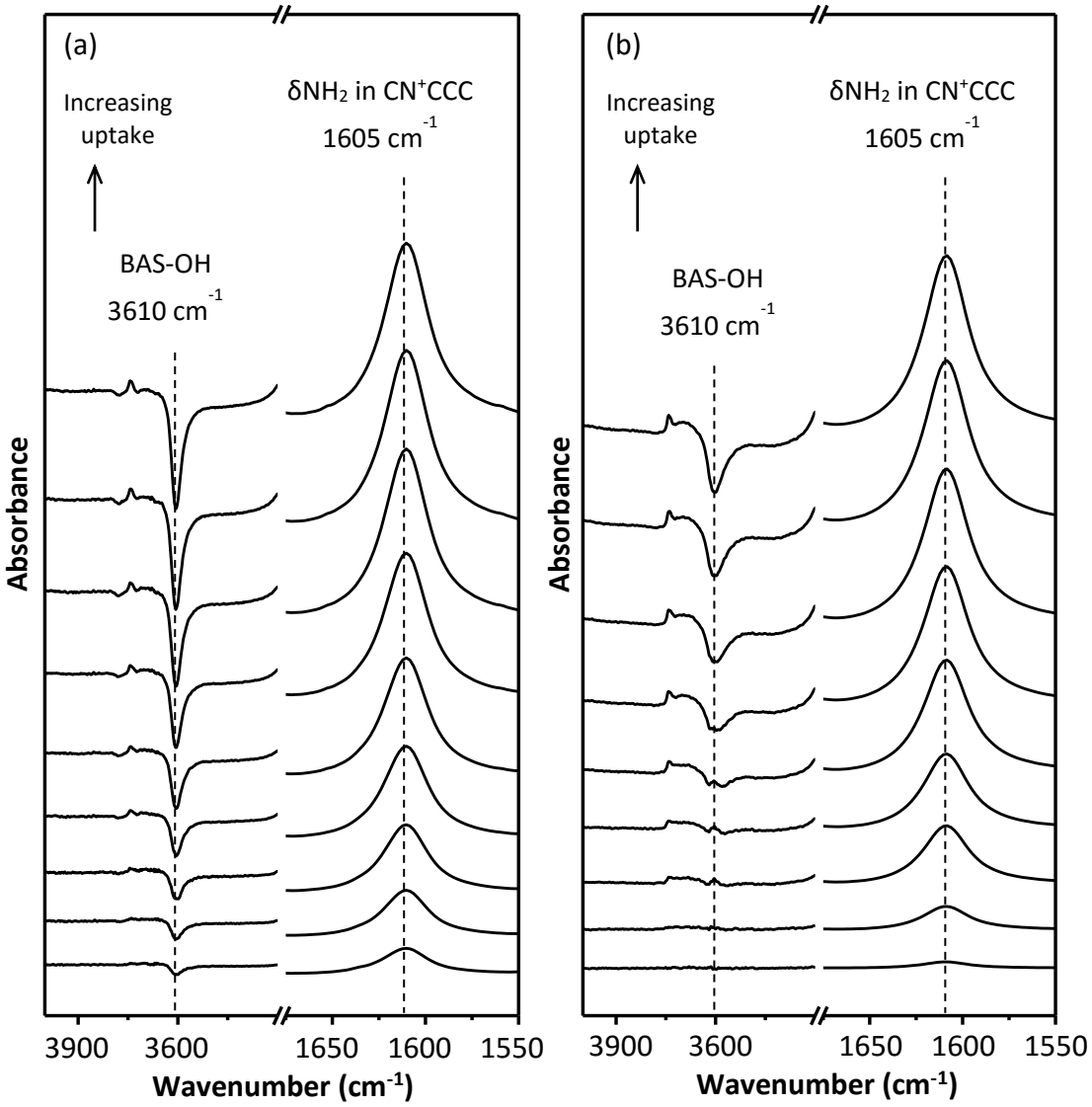

Figure 3.10. Difference IR spectra of O-H stretching and N-H bending vibration region (δNH_2) for (a) H-MFI and (b) EFSi-MFI-46% with increasing N-methylpropylamine uptake at 423 K.

coverage (determined from the peak area of 3610 cm^{-1}) as a function of the overall-BAS-OH coverage (determined from the peak area of 1605 cm^{-1}) on H-MFI gives a linear relationship same as the adsorption of pyridine on H-MFI (**Figure 3.11 a**). For EFSi-MFI, N-methylpropylamine did not show a clearly two-regime adsorption compared to pyridine adsorption (**Figure 3.10 b**). However, the curve for the coverage of BAS as a function of the coverage of overall-BAS shows that BAS coverage is always lower than the overall BAS coverage (**Figure 3.11 b**), indicating higher coverage on EFSi-BAS than normal BAS, especially under 45% coverage of the overall-BAS, which correlated to the proportion of EFSi-BAS (46%) in EFSi-MFI-46%. The preferential adsorption of N-methylpropylamine along with the similar preferential adsorption of pyridine **Section 3.1.2** on EFSi-BAS suggests that this kind of cationic sorbed species is more stabilized on the BAS with EFSi, or in other words, reveals that the proximity of EFSi contributes additional interaction with the guest base molecule.

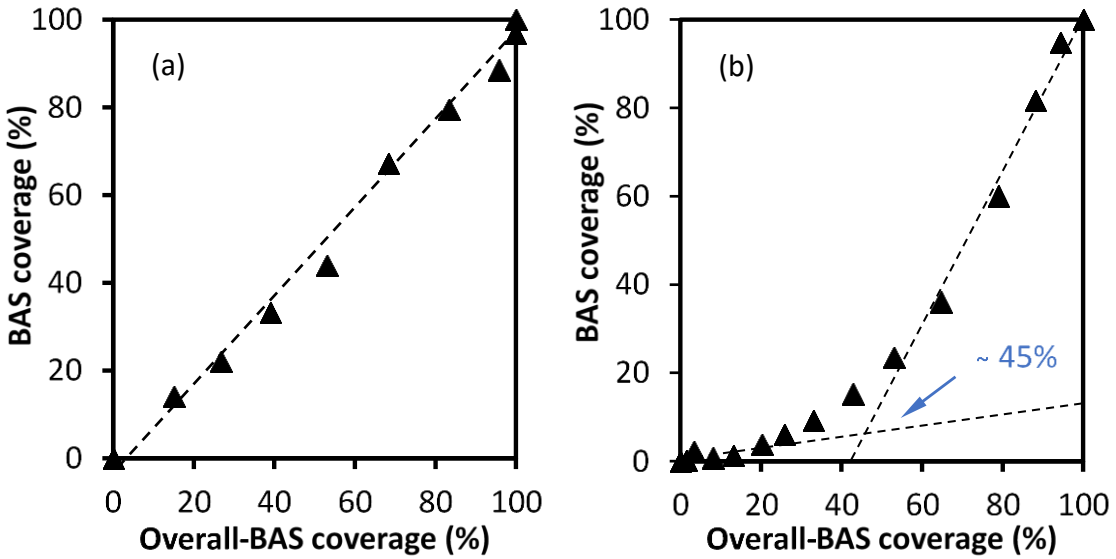

Figure 3.11. BAS coverage on (a) H-MFI and (b) EFSi-MFI-46% with increasing N-methylpropylamine uptake at 423 K. (Overall-BAS coverage determined from the peak area of 1605 cm^{-1} band for δNH_2; BAS-OH coverage determined from the peak area of 3610 cm^{-1} band.)

3.2.4 Diethyl ether adsorption on H-MFI and EFSi-MFI

Another model molecule for adsorption study is diethyl ether, which is a weaker base compared to pyridine and N-methylpropylamine. Diethyl ether also has a 5-membered chain similar to n-pentane and N-methylpropylamine. However, the study of the mechanism of ether adsorption on BAS has not been practiced as others.

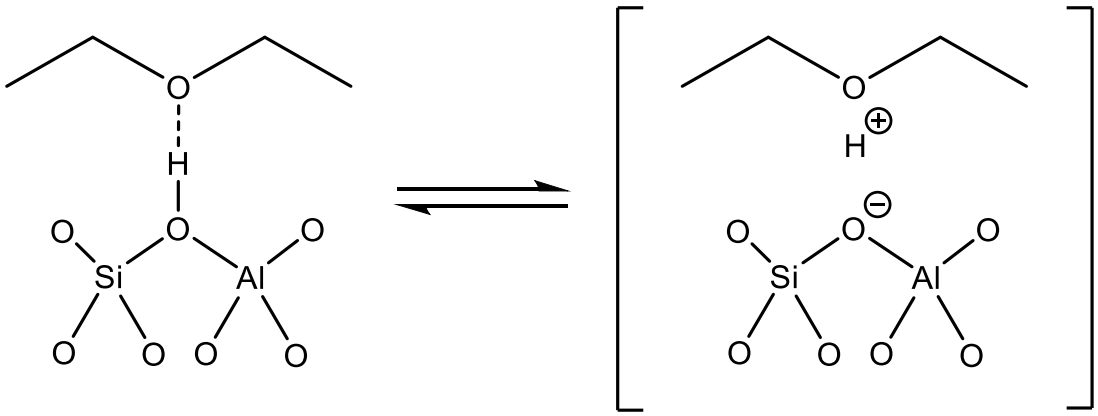

Scheme 3.5. Proposed structure of adsorbed diethyl ether on BAS-OH group of MFI (adapted from Ref. [159]).

Osuga et al. went through ethanol dehydration and diethyl ether adsorption on H-ZSM-5 zeolites on IR and found that diethyl ether adsorbs on the acidic OH groups of H-ZSM-5. A more complicated spectrum was found to be related to some specific interaction between diethyl ether and the acidic OH groups[159]. By further comparing the spectra of diethyl ether adsorption on H-ZSM-5 and D-ZSM-5, they confirmed that there is Fermi resonance between the OH groups and the ethyl groups of diethyl ether. Since it is commonly accepted that vibrational coupling only occurs in the same molecular, they came up with an ion-paired adsorbed species forming upon diethyl ether adsorption on SiOHAl groups (**Scheme 3.5**).

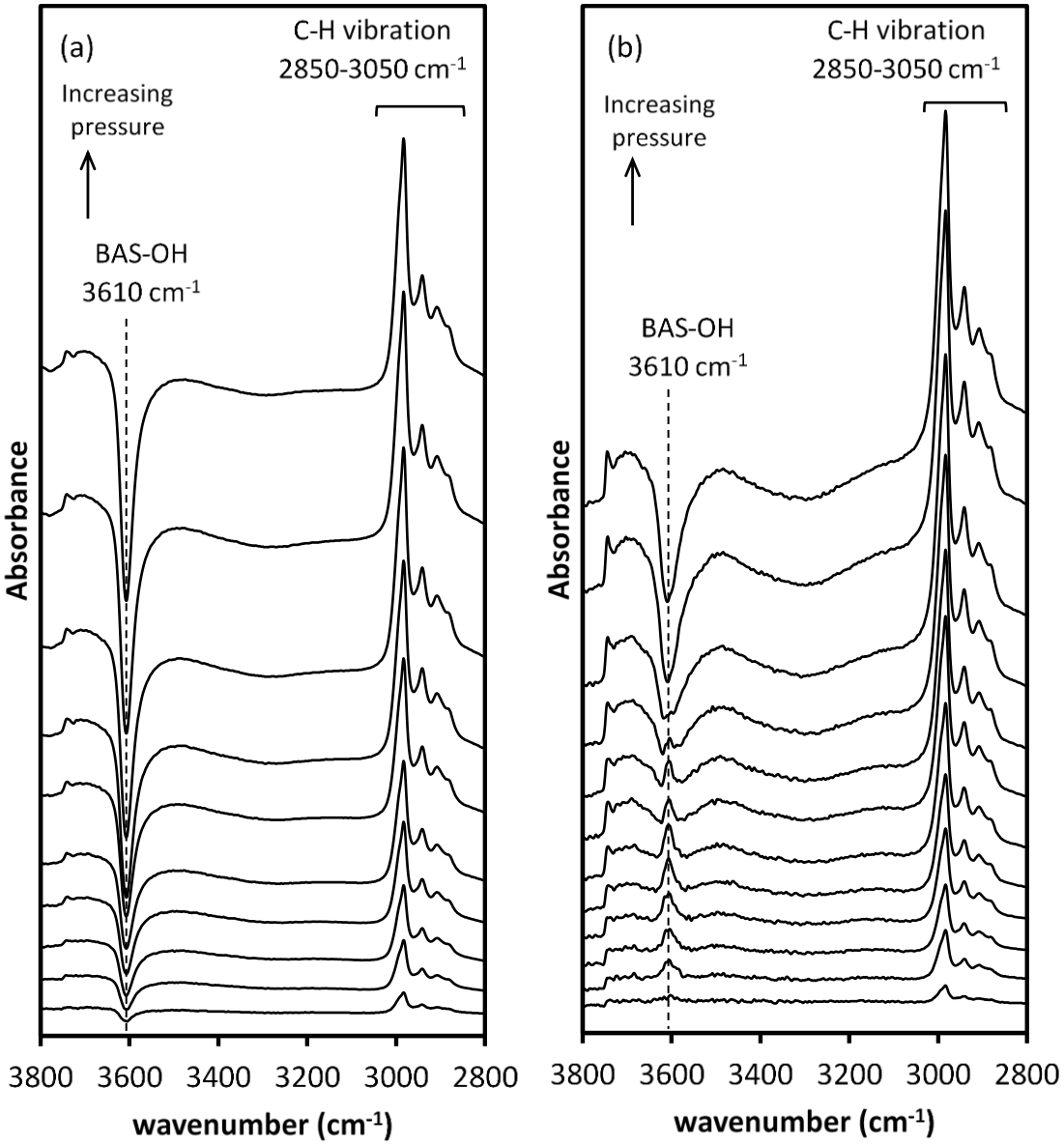

Figure 3.12. Difference IR spectra of O-H stretching and C-H stretching vibration region for (a) H-MFI and (b) EFSi-MFI-46% with increasing diethyl ether uptake at 333 K.

Figure 3.12 shows the difference spectra of diethyl ether adsorption on H-MFI and EFSi-MFI-46% at 333 K. As H-MFI was exposed to diethyl ether, the characteristic band at SiOHAl groups (BAS-OH 3610 cm^{-1}) decreased and concomitantly the band of C-H stretching vibration in the region of 2850-3050 cm^{-1} appeared and increased in intensity (**Figure 3.12 a, 3.13 a**). In contrast, the

adsorption of diethyl ether on EFSi-MFI-46% exhibited two different regimes as pyridine adsorption. During exposure to the first aliquots of diethyl ether, the band of the BAS-OH barely changed up to around 50% coverage of overall BAS-OH (determined from the area increase of C-H stretching vibration band in the region of 2850-3050 cm^{-1}) (**Figure 3.12 b, 3.13 b**), which is almost equivalent to the concentration of EFSi-BAS-46% (46% of overall BAS). Subsequently, the BAS-OH band began to decrease in intensity (**Figure 3.12 b, 3.13 b**). This similar performance of diethyl ether adsorption to pyridine adsorption suggests that the interaction between diethyl ether and BAS-OH is enhanced by the presence of EFSi in vicinity. The mechanism for this enhancement is not clear for now due to the controversial sorbed structure for ethers on acidic OH groups and calls for further study. Nevertheless, the two-regime adsorption of diethyl ether on EFSi-MFI confirms the enhancement of the stabilization of the adsorbed state of diethyl ether, which is most key to be attributed to the interaction between EFSi and the alkyl chain of diethyl ether.

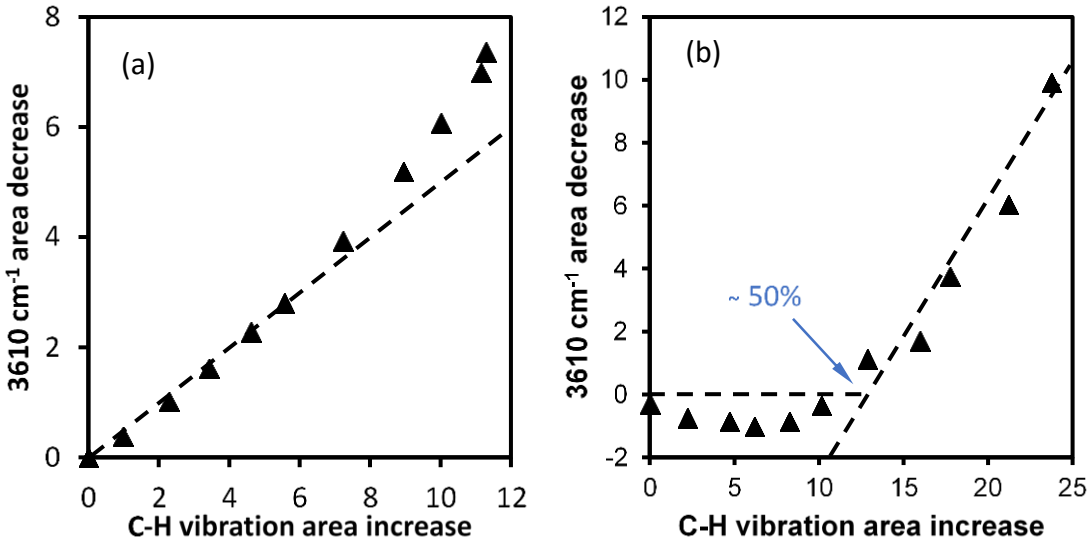

Figure 3.13. The band area decrease of 3610 cm^{-1} as a function of the band area increase of C-H vibration at 2850-3050 cm^{-1} on (c) H-MFI and (d) EFSi-MFI-46% upon diethyl ether adsorption at 333 K.

3.2.5 Water adsorption on H-MFI and EFSi-MFI

To further understand the properties of the BAS-OH groups on H-MFI and EFSi-MFI, water was adsorbed on both at 423 K with increasing water pressure. It is reported that the adsorption bands of IR for fundamental vibrations of non-interacted BAS-OH are located at 3610 cm^{-1} (O-H stretching, υOH), 1080 cm^{-1} (in-plane bending, δOH) and 300 cm^{-1} (out-plane bending, γOH)[160]. In practice, δOH and γOH bands could not be observed because of the extremely high intensity of the Si-O stretching vibration band from the zeolite framework at around 1100 cm^{-1} and the limitation of the mid-IR (400 cm^{-1}). However, with water adsorbed on the BAS-OH forming a hydrogen bond, the stretching band (3610 cm^{-1}, υOH) shifts to lower frequency while bending bands (1080 cm^{-1} for δOH and 300 cm^{-1} for γOH) shift to higher frequency[161]. These shifts are dependent on the strength of the hydrogen bond, generally, a more obvious shift occurs with a stronger hydrogen bond interaction. Therefore in the case of water adsorption on zeolite, the strong hydrogen bonding results in the overlap of the perturbed stretching band (υOH) and the overtones of bending bands (2 δOH and 2 γOH), splitting the perturbed stretching band (υOH) into three, the so-called ‘‘A, B, C triplet’’, by the Fermi resonance[160,161].

Figure 3.14 exhibits the difference spectra of water adsorption on H-MFI and EFSi-MFI-46% for the situation of forming 1:1 complexes, which are present when the number of adsorbed water molecules is lower than the number of available BAS-OH groups. On both samples, a negative band at 3610 cm^{-1} was observed for the water adsorption on SiOHAl groups. Meanwhile, the A, B, C triplet bands appeared and evolved increasingly in intensity at 2900 cm^{-1}, 2465 cm^{-1} and 1700 cm^{-1}, respectively. It is worth noting that on H-MFI, the intensity of A band (2900 cm^{-1}) is lower than B band (2465 cm^{-1}) while on EFSi-MFI-46% a contrary situation with a higher intensity of A band is presented. These intensity differences are proposed to be related to the presence of EFSi.

A more precise distinction between water adsorption on BAS and EFSi-BAS is revealed by subtracting the spectra of H-MFI from the one of EFSi-MFI with nearly one sorped water molecule per overall-BAS-OH (the uppermost

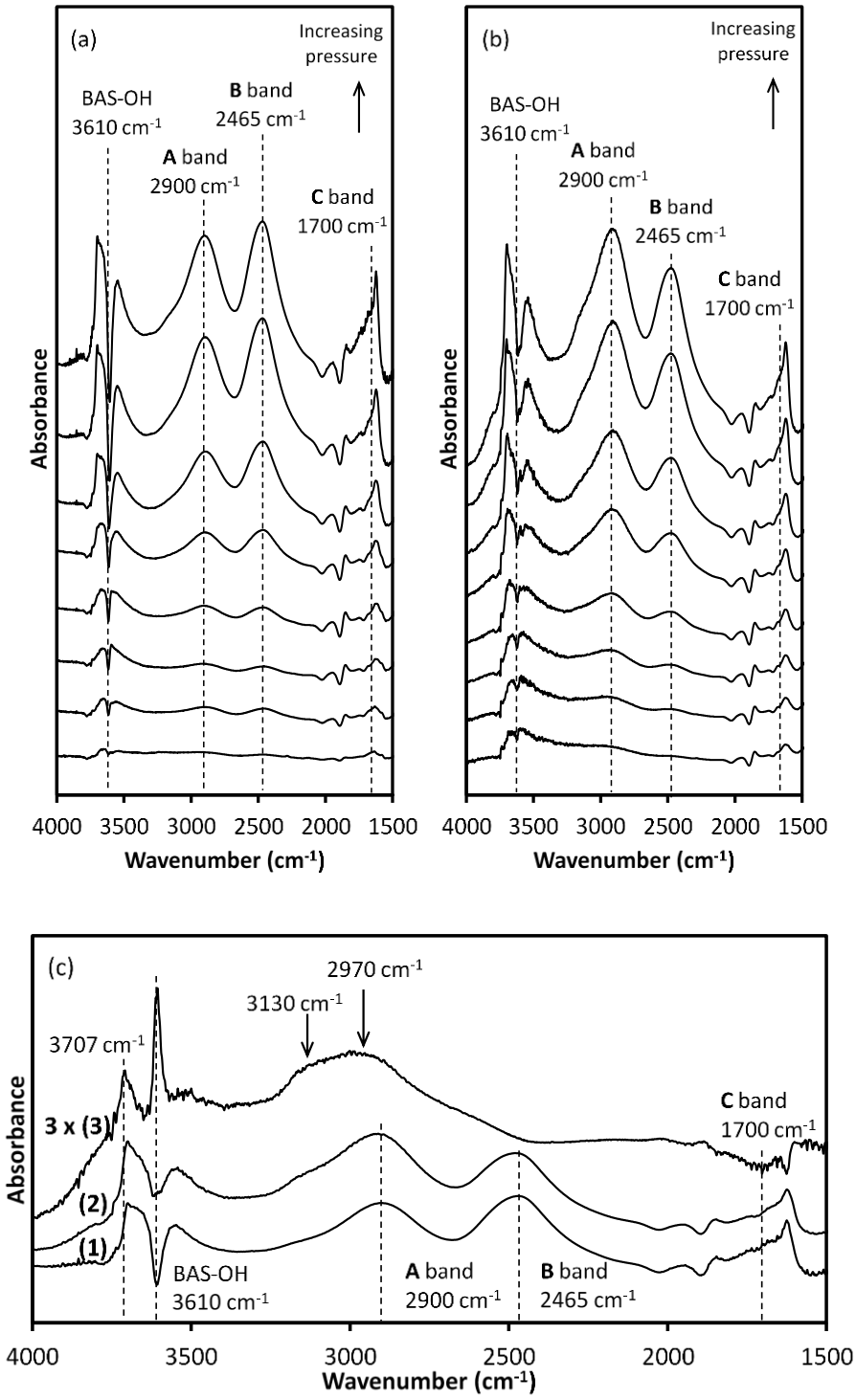

Figure 3.14. Difference IR spectra for (a) H-MFI, (b) EFSi-MFI-46% with increasing water adsorption up to one H_2O molecule per overall-BAS-OH group at 423 K and (c) difference spectra between (b) and (a) showing difference of H_2O adsorption on H-MFI and EFSi-MFI-46% under the coverage of around one H_2O molecule per overall-BAS-OH ((1) H-MFI with H_2O adsorption, (2) EFSi-MFI-46% with H_2O adsorption and (3) subtraction of spectra (1) from (2)).

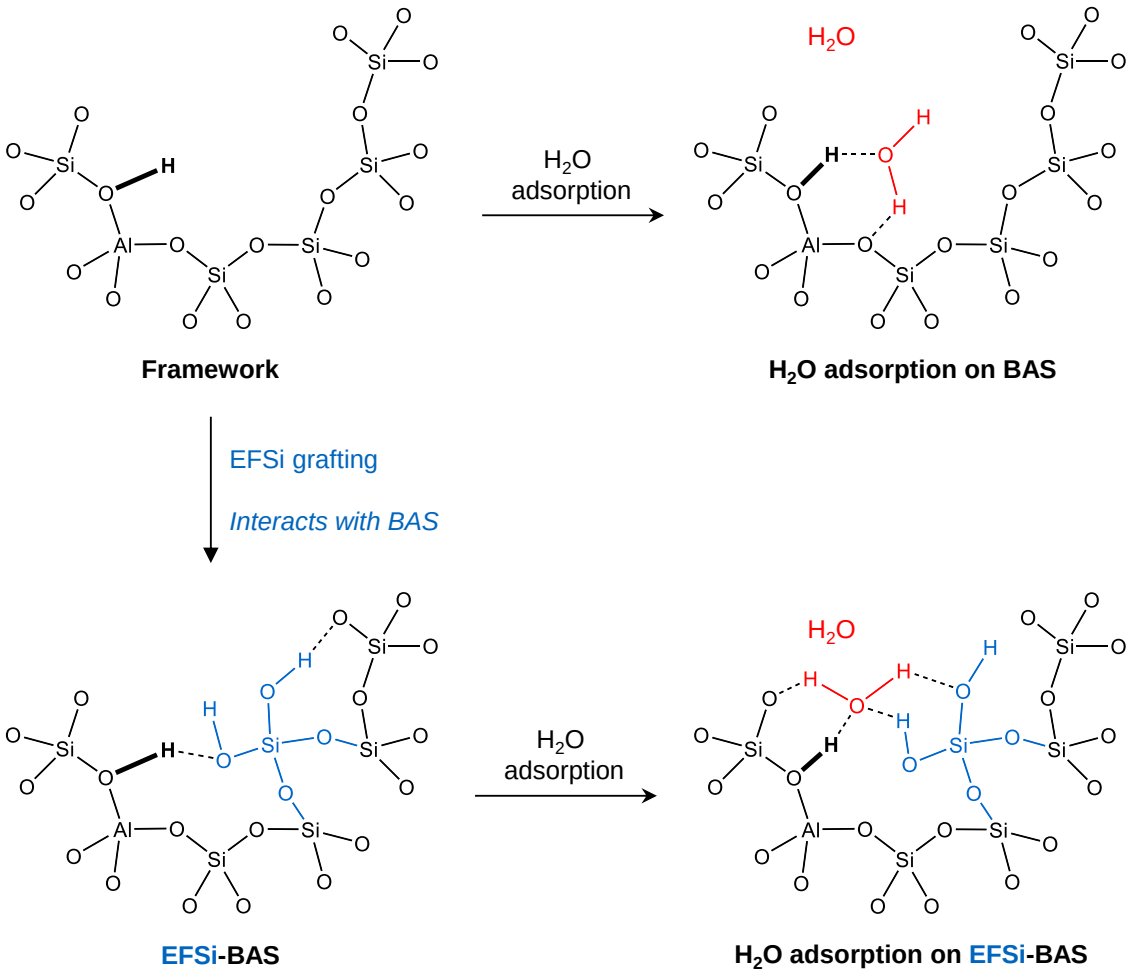

Scheme 3.6. Proposed structure of adsorbed water on BAS and EFSi-BAS.

spectra in **Figure 3.14 a** and **b**), which is shown in **Figure 3.14 c (3)** with the two original difference spectra (**Figure 3.14 c (1)** and **(2)**) as references. There are two obvious positive bands at 3707 cm^{-1} and 3610 cm^{-1}. The one at 3707 cm^{-1} is due to the normal Si-OH groups perturbed by H_2O[162]. The positive band at 3610 cm^{-1} is a result of the absence of EFSi-BAS-OH vibration at this wavenumber on EFSi-MFI-46% that can be proved by the band area (around 50% of the negative band area at 3610 cm^{-1} on H-MFI with sorped H_2O, **Figure 3.14 c (1)**). However, it is deduced that the fundamentally A, B, C triplet bands for perturbed BAS-OH vibration barely changed with the presence of EFSi, illustrating the identical interaction between H_2O molecule and BAS-OH regardless of the EFSi species

nearby. The relatively higher intensity of A band on EFSi-MFI is due to the two new bands at 2970 cm^{-1} and 3130 cm^{-1} (**Figure 3.14 c (3)**), which are attributed to the perturbed EFSi-OH groups. Considering the lower wavenumber of these EFSi-OH groups compared to the normal silanols in zeolites (3707 cm^{-1}) under the perturbation of water, we here propose the structure of EFSi-BAS with sorped H_2O as **Scheme 3.6**. The two Si-OH groups on EFSi species interact with the oxygen atom and the free hydrogen atom of H_2O molecule sorped on BAS-OH by hydrogen bond resulting in the two vibration bands at 2970 cm^{-1} and 3130 cm^{-1}. These lower wavenumbers are attributed to the strong hydrogen bonding interaction between EFSi-OH and sorped H_2O because of the more confined space creating by EFSi-BAS sites.

3.2.6 Methanol adsorption on H-MFI and EFSi-MFI

Difference IR spectra of adsorbed methanol under the pressure up to1 mbar on H-MFI and EFSi-MFI-46% are shown in **Figure 3.15**. On both samples, the intensity of the band 3610 cm^{-1} for BAS-OH decreased with the appearance of the CH stretching band in the region of 2650 – 3050 cm^{-1}. Similar A, B, C triplet bands to the case of water adsorption appeared and evolved increasingly until the band 3610 cm^{-1} fully disappeared. This entails that strong hydrogen bond formed between the SiOHAl group and the sorped methanol as a single molecule (**Scheme 3.7**)[163]. The relative stronger intensity of C band compared to A and B bands for methanol adsorption is attributed to the stronger hydrogen-bond interaction between the SiOHAl groups and methanol than water due to its higher proton affinity[164,165]. Consequently, the A, B, C triplet bands decreased in intensity with increasing methanol pressure because of the formation of large adsorbate clusters more than one methanol molecule per SiOHAl group[166].

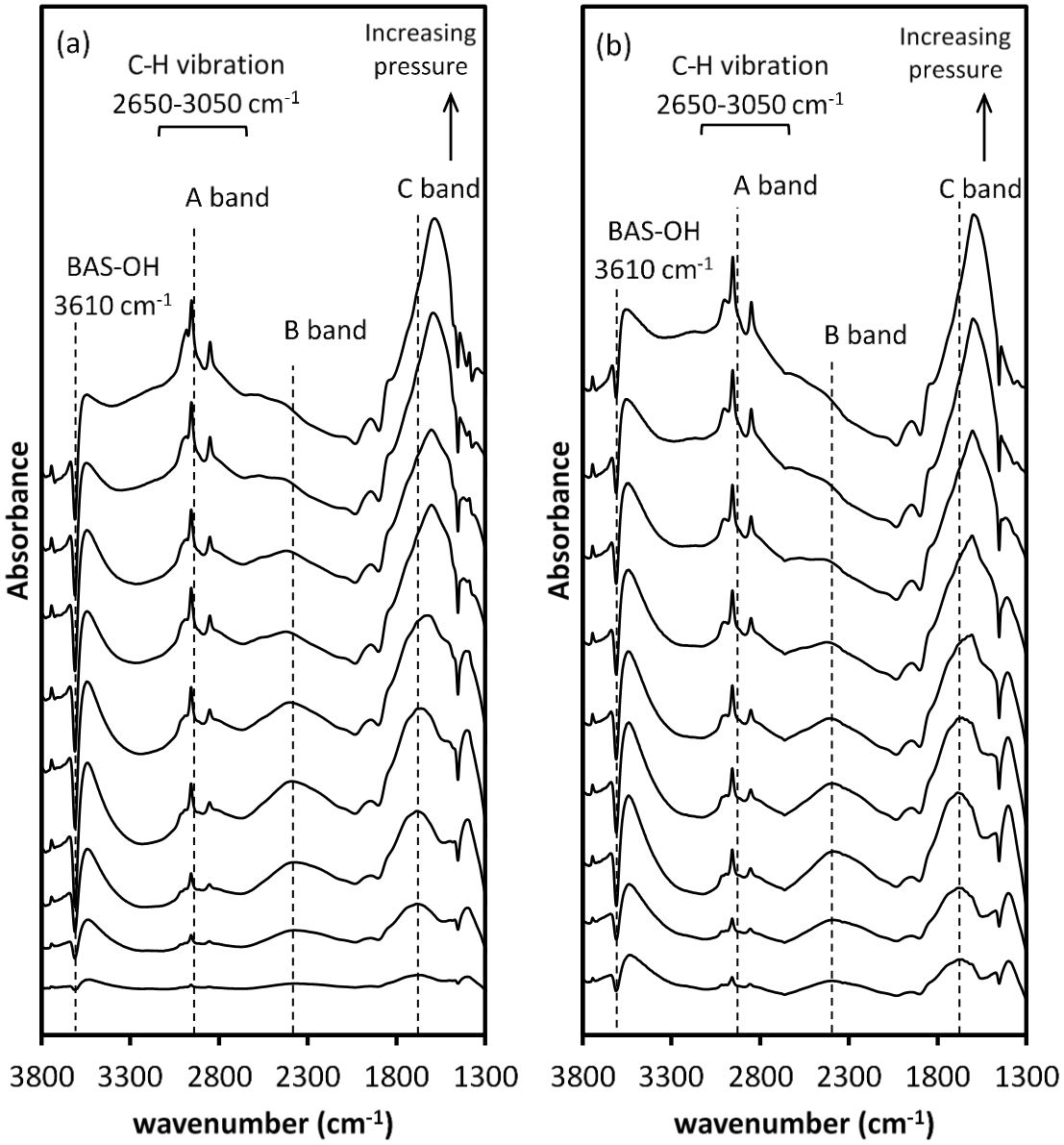

Figure 3.15. Difference IR spectra for (a) H-MFI, (b) EFSi-MFI-46% with increasing methanol pressure up to 1 mbar at 423 K.

Due to the overlap of CH stretching vibration and the A band, it is difficult in the case of methanol adsorption to distinguish the EFSi-OH groups perturbed by methanol compared with water adsorption, which is low in intensity and also in this region.

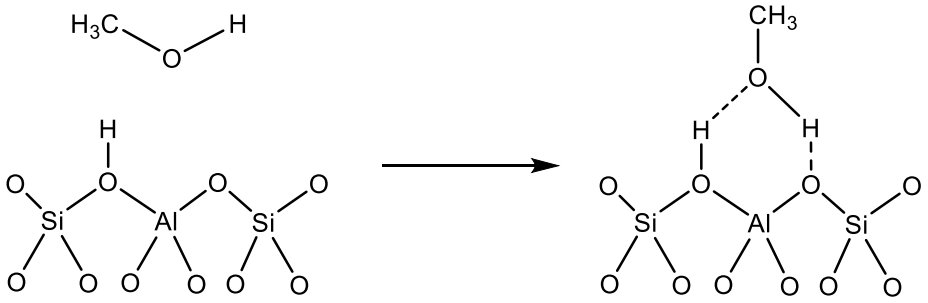

Scheme 3.7. Proposed structure of adsorbed methanol on SiOHAl groups.

3.3 Chapter summary

Extra framework Si (EFSi) was grafted in the vicinity of the BAS by a controllable post-treatment by adsorbing n,n-dimethyltrimethylsilylamine $(CH_3)_3SiN(CH_3)_2$ on BAS followed with calcination. The proximity of the introduced EFSi and the BAS was confirmed by the IR spectra of adsorbed various probe molecules, *e.g.*, pyridine, ammonia, alkyl-amines, n-pentane, diethyl ether, water and methanol.

A two-regime adsorption proceeded during pyridine adsorption on EFSi-MFI, pyridine preferentially adsorbed on EFSi-BAS and then on normal BAS. In this way, the concentrations of the normal BAS and EFSi-BAS were determined on EFSi-MFI samples.

Amines such as diethylamine and N-methylpropylamine also showed similar preferential adsorption on EFSi-BAS. In particular, stronger preferential adsorption was found to be the more pronounced the bulkier the adsorbed base was. Since the acid strength for normal BAS and EFSi-BAS are the same demonstrated by the simutaniously adsorption of ammonia on BAS and EFSi-BAS and the same TPD curves of adsorbed ammonia on all the samples, this preferential adsorption of pyridine and alkyl amines is speculated to be the result of additional van der Waals interactions of EFSi with the organic alkyl/aryl chain of a guest molecule.

Nevertheless, sorped n-pentane perturbed simultaneously both BAS and EFSi-BAS. By comparing the IR spectra of EFSi-MFI and pre-pyridine-titrated EFSi-MFI with n-pentane adsorption, a pair of perturbed O-H vibrational bands, centered at 3408 cm^{-1} and 3538 cm^{-1} were observed, attributed to perturbed vibrations of EFSi-BAS-OH and EFSi-OH. With this evidence, a proposed structure of EFSi-BAS constituted of a bridge SiOHAl interacting with geminal EFSi-OH via hydrogen bondings is given. The lower wavenumber of the perturbed EFSi-BAS-OH vibration (3408 cm^{-1}), with respect to that of BAS-OH (3474 cm^{-1}), indicates a stronger polarization of the EFSi-BAS-OH group by the adjacent EFSi.

Further adsorption with diethyl ether also provided a preferentially adsorption on EFSi-BAS, which confirmed the stabilization of its adsorbed state via additional van der Waals interactions between the EFSi and the organic alkyl/aryl chain.

Moreover, the two additional IR bands at 2970 cm^{-1} and 3130 cm^{-1} during water adsorption on EFSi-MFI compared with H-MFI are attributed to the perturbed EFSi-OH groups, therefore, a proposed scheme for H_2O adsorption on EFSi-BAS is given and somewhat proved the hypothetical structure of EFSi-BAS. However, due to the overlapping of CH vibration and A band, such perturbed EFSi-OH groups are hard to distinguish in methanol adsorption.

So far, these results leads to the conclusion that the proximity of grafted EFSi leads to hydrogen bonding and strengthens the binding with pyridine, alkyl amines and diethyl ether via van der Waals interaction with their aryl or alkyl chains. In contrast, for base molecules with no alkyl or aryl groups such as ammonia and very weak bases, such as n-pentane, their binding with BAS is barely affected by EFSi.

Chapter 4. Catalytic activity of EFSi-BAS in n-pentane cracking

4.1 The turn over frequency (TOF) of n-pentane cracking on BAS and EFSi-BAS

The protolytic cracking and dehydrogenation of n-pentane (**Scheme 4.1**) proceeds via three different cracking pathways, i.e., forming methane + butene (P1, $C_1 + C_4^=$), ethane + propene (P2, $C_2 + C_3^=$), propane + ethene (P3, $C_3 + C_2^=$) as well as one pathway for dehydrogenation. The catalytic activity of BAS on n-pentane cracking reaction has been well studied[53,89,129]. Zeolites in the proton form and in the absence of extra-framework species show equal reaction rates per BAS with different Si/Al ratios for pentane cracking and dehydrogenation[89].

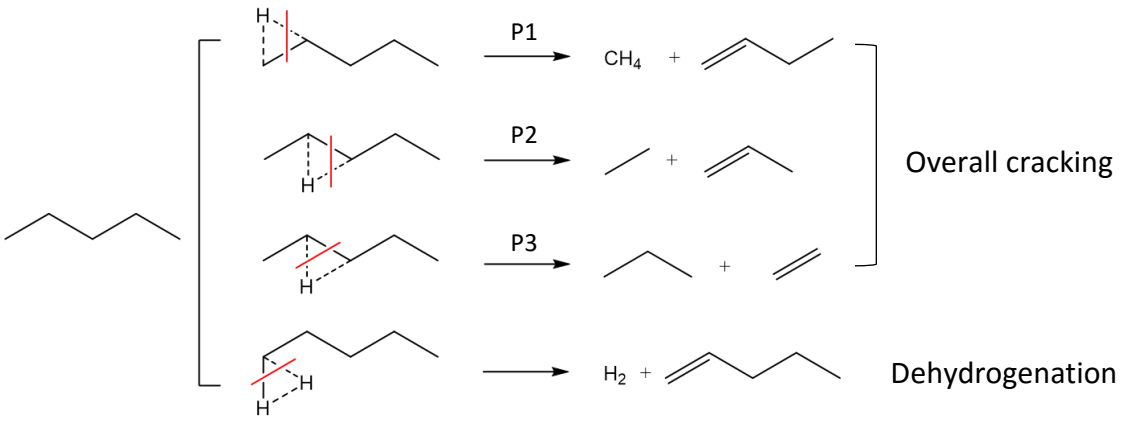

Scheme 4.1. Reaction pathways for n-pentane cracking on H-MFI. Red line indicates location of the bond scission. Dotted line represents the BAS proton coordinated with C or H in pentane as penta-coordinated carbon in transition state.

In the present work, for the kinetic study, the conditions of the reactions were precisely controlled to obtain the initial rates for all the reaction pathways on H-MFI and EFSi-MFI samples (**Figure 4.1**) and the reaction showed first order of n-pentane pressure for all the reaction pathways on H-MFI and EFSi-MFI (**Figure 4.2**).

The turn over frequencies (TOFs) of n-pentane on BAS of H-MFI for all pathways of cracking and dehydrogenation were measured at temperatures from 753 K to 793 K with 0.020 bar of n-pentane (**Table 4.1**). These results are

denoted as the TOF for BAS. The overall cracking and dehydrogenation TOFs on BAS at 753 K are 0.47 × 10^{-3} s^{-1} and 0.32 × 10^{-3} s^{-1}, similar to those reported in our previous study [129].

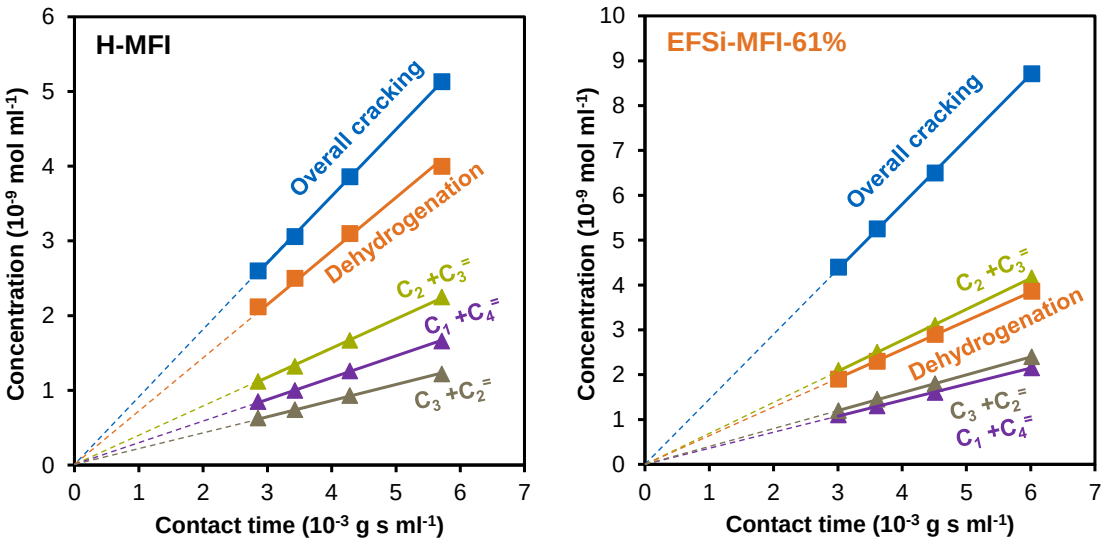

Figure 4.1. Concentration of products in different reaction pathways at different contact time (1-3% pentane conversion) in H-MFI and EFSi-MFI-61% samples at 793K.

EFSi-MFIs show higher TOFs in overall cracking as well as all the cracking pathways, increasing linearly with the concentration of EFSi-BAS in EFSi-MFI samples and similar dehydrogenation rates (**Figure 4.3**, **Table 4.2-4.4**). Obviously, the reaction rate on EFSi-MFI is higher than that on H-MFI; however, the catalytic activity of EFSi-MFI involves the contribution from both BAS and EFSi-BAS. By extrapolating the linear curve in **Figure 4.3** to EFSi-BAS portion of 100%, the TOF of EFSi-BAS is obtained and summarized in **Table 4.5**. Compared to BAS, the presence of EFSi increases the TOF for overall cracking from 0.47 × 10^{-3} s^{-1} to 1.1 × 10^{-3} s^{-1} at 753 K (**Table 4.6**). The TOFs on all different cracking pathways were promoted by 1.8 – 3.1 times at 753 K. The dehydrogenation rate was barely affected by EFSi at 753 K, while it decreased above 773 K (**Table 4.1** and **4.5**, **Figure 4.3**).

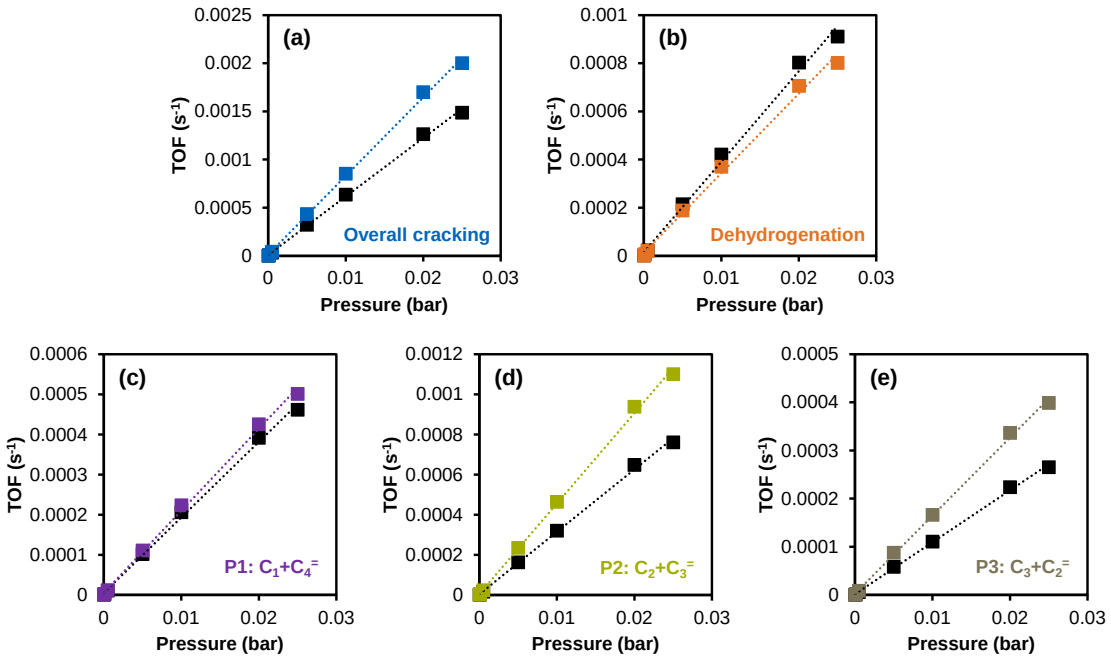

Figure 4.2. First-order reaction of (a) overall cracking, (b) dehydrogenation and (c) – (e) different cracking pathways on H-MFI (black symbols) and EFSi-MFI-46% (colored symbols) at 793 K.

Table 4.1. TOFs on different reaction pathways per BAS site (H-MFI) at 753 - 793 K with 0.020 bar of n-pentane.

T (K)	TOF_{BAS} (10^{-3} s^{-1})				
	P1	P2	P3	Overall[a]	Dehyd.[b]
753	0.13 ± 0.00	0.24 ± 0.00	0.10 ± 0.01	0.47 ± 0.05	0.32 ± 0.01
763	0.18 ± 0.01	0.30 ± 0.00	0.13 ± 0.00	0.61 ± 0.03	0.44 ± 0.01
773	0.23 ± 0.00	0.38 ± 0.00	0.18 ± 0.00	0.79 ± 0.02	0.56 ± 0.02
783	0.34 ± 0.02	0.47 ± 0.00	0.24 ± 0.02	1.0 ± 0.1	0.81 ± 0.05
793	0.45 ± 0.02	0.60 ± 0.01	0.33 ± 0.01	1.4 ± 0.1	1.1 ±0.0

[a] Overall cracking; [b] Dehydrogenation.

Table 4.2. TOFs on different reaction pathways in EFSi-MFI-18% at 753 - 793 K with 0.020 bar of n-pentane.

T (K)	$TOF_{EFSi\text{-}MFI\text{-}18\%}$ (10^{-3} s^{-1})				
	P1	P2	P3	Overall[a]	Dehyd.[b]
753	0.18 ± 0.00	0.34 ± 0.00	0.12 ± 0.01	0.63 ± 0.04	0.39 ± 0.00
763	0.24 ± 0.00	0.41 ± 0.01	0.17 ± 0.01	0.82 ± 0.04	0.45 ± 0.03
773	0.30 ± 0.00	0.51 ± 0.00	0.20 ± 0.01	1.0 ± 0.0	0.58 ± 0.03
783	0.34 ± 0.01	0.62 ± 0.01	0.24 ± 0.01	1.2 ±0.1	0.71 ± 0.03
793	0.44 ± 0.01	0.76 ± 0.01	0.35 ± 0.02	1.6 ± 0.1	0.92 ± 0.04

[a] Overall cracking; [b] Dehydrogenation.

Table 4.3. TOFs on different reaction pathways in EFSi-MFI-46% at 753 - 793 K with 0.020 bar of n-pentane.

T (K)	$TOF_{EFSi\text{-}MFI\text{-}46\%}$ (10^{-3} s^{-1})				
	P1	P2	P3	Overall[a]	Dehyd.[b]
753	0.19 ± 0.00	0.40 ± 0.00	0.19 ± 0.01	0.78 ± 0.05	0.34 ± 0.00
763	0.24 ± 0.00	0.48 ± 0.01	0.22 ± 0.01	0.94 ± 0.04	0.45 ± 0.03
773	0.30 ± 0.00	0.59 ± 0.00	0.28 ± 0.01	1.2 ± 0.0	0.57 ± 0.03
783	0.39 ± 0.01	0.72 ± 0.01	0.39 ± 0.01	1.5 ±0.1	0.74 ± 0.03
793	0.49 ± 0.01	0.87 ± 0.01	0.50 ± 0.02	1.9 ± 0.1	0.95 ± 0.04

[a] Overall cracking; [b] Dehydrogenation.

Table 4.4. TOFs on different reaction pathways in EFSi-MFI-61% at 753 - 793 K with 0.020 bar of n-pentane.

T (K)	$TOF_{EFSi\text{-}MFI\text{-}61\%}$ (10^{-3} s^{-1})				
	P1	P2	P3	Overall[a]	Dehyd.[b]
753	0.20 ± 0.00	0.45 ± 0.00	0.22 ± 0.01	0.88 ± 0.04	0.34 ± 0.00
763	0.26 ± 0.00	0.54 ± 0.01	0.25 ± 0.01	1.1 ± 0.0	0.45 ± 0.03
773	0.32 ± 0.01	0.66 ± 0.00	0.31 ± 0.01	1.3 ± 0.1	0.57 ± 0.03
783	0.41 ± 0.01	0.79 ± 0.01	0.44 ± 0.01	1.6 ±0.1	0.71 ± 0.03
793	0.50 ± 0.01	0.96 ± 0.01	0.55 ± 0.02	2.0 ± 0.1	0.91 ± 0.04

[a] Overall cracking; [b] Dehydrogenation.

Table 4.5. TOFs on different reaction pathways per EFSi-BAS site at 753 - 793 K with 0.020 bar of n-pentane.

T (K)	$TOF_{EFSi\text{-}BAS}$ (10^{-3} s^{-1})				
	P1	P2	P3	Overall[a]	Dehyd.[b]
753	0.24 ± 0.00	0.59 ± 0.00	0.31 ± 0.02	1.1 ± 0.1	0.35 ± 0.01
763	0.31 ± 0.01	0.69 ± 0.00	0.33 ± 0.01	1.3 ± 0.0	0.45 ± 0.02
773	0.38 ± 0.00	0.84 ± 0.00	0.40 ± 0.00	1.6 ± 0.0	0.57 ± 0.02
783	0.45 ± 0.01	1.0 ± 0.0	0.57 ± 0.02	2.0 ± 0.1	0.66 ± 0.03
793	0.54 ± 0.01	1.2 ± 0.0	0.70 ± 0.02	2.4 ± 0.1	0.79 ± 0.02

[a] Overall cracking; [b] Dehydrogenation.

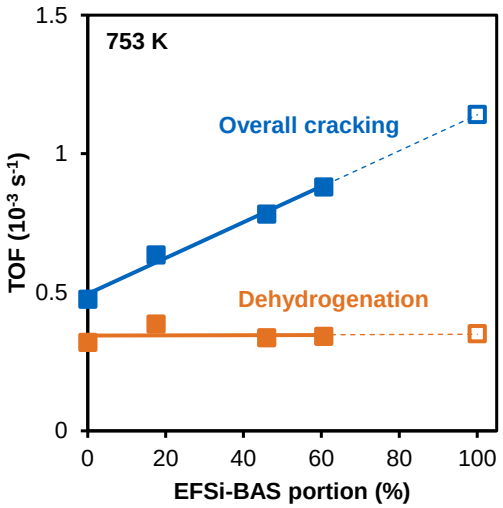
753 K
Overall cracking
Dehydrogenation
TOF (10-3 s-1)
EFSi-BAS portion (%)

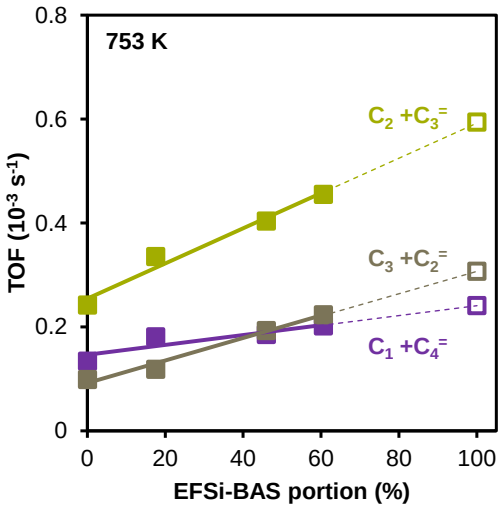
753 K
C2 +C3=
C3 +C2=
C1 +C4=
TOF (10-3 s-1)
EFSi-BAS portion (%)

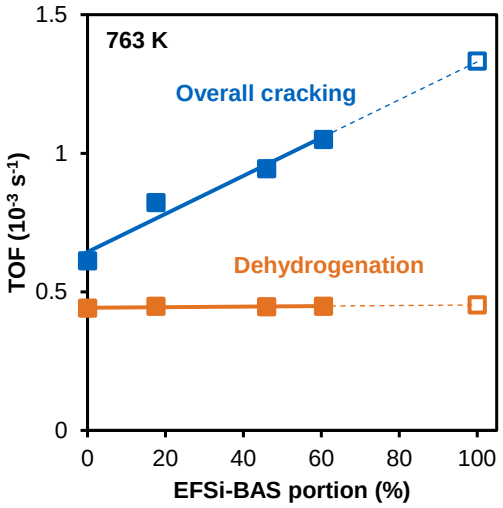
763 K
Overall cracking
Dehydrogenation
TOF (10-3 s-1)
EFSi-BAS portion (%)

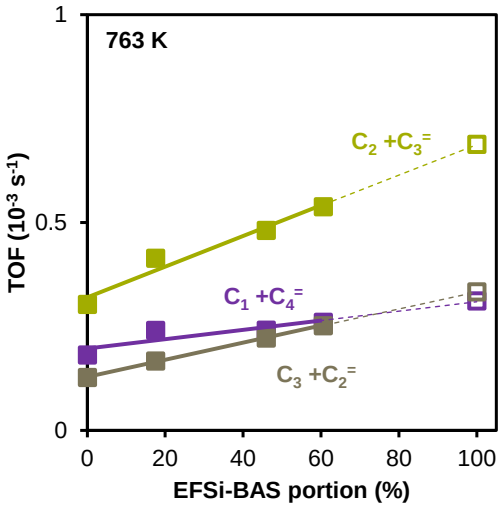
763 K
C2 +C3=
C1 +C4=
C3 +C2=
TOF (10-3 s-1)
EFSi-BAS portion (%)

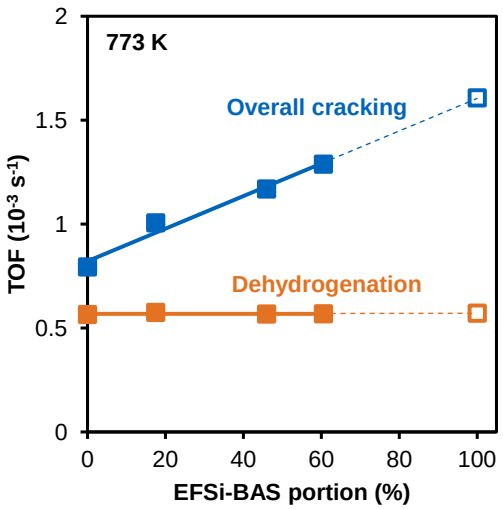
773 K
Overall cracking
Dehydrogenation
TOF (10-3 s-1)
EFSi-BAS portion (%)

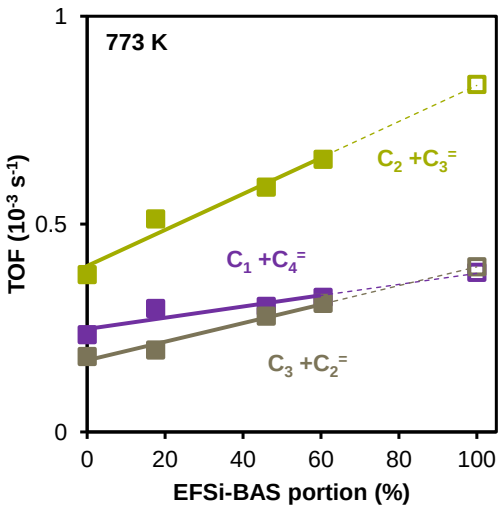
773 K
C2 +C3=
C1 +C4=
C3 +C2=
TOF (10-3 s-1)
EFSi-BAS portion (%)

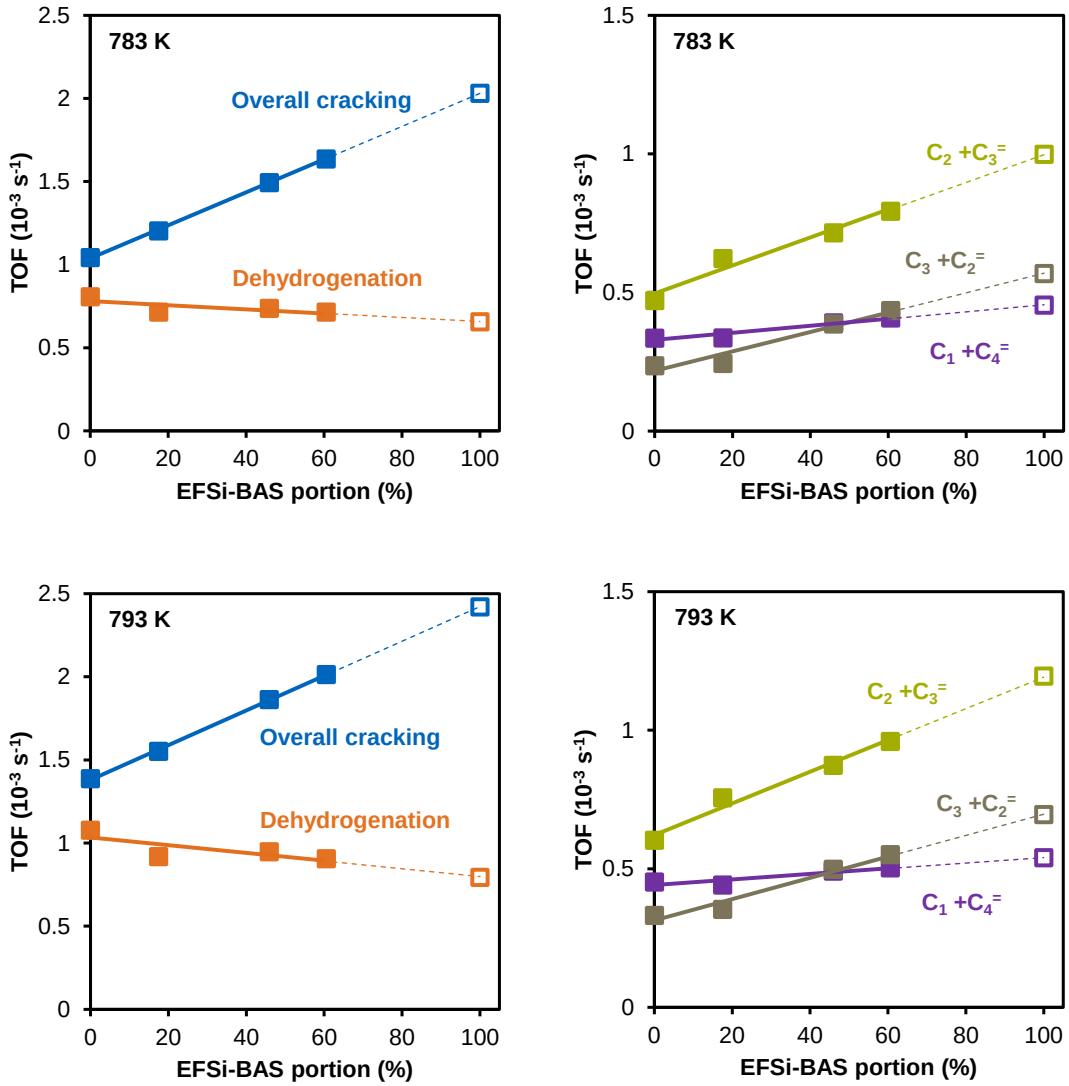

Figure 4.3. TOF as a function of EFSi-BAS percentage on the samples at different temperatures. Solid symbols (■) for experimentally measured TOF, hollow symbols (□) for extrapolated TOF to 100% EFSi-BAS.

Table 4.6. Comparison of TOFs on different reaction pathways per BAS and EFSi-BAS at 753 K with 0.020 bar of n-pentane.

Active site	TOF (10^{-3} s^{-1})				
	P1	P2	P3	Overall[a]	Dehyd.[b]
BAS	0.13 ± 0.00	0.24 ± 0.00	0.10 ± 0.01	0.47 ± 0.05	0.32 ± 0.01
EFSi-BAS	0.24 ± 0.00	0.59 ± 0.00	0.31 ± 0.02	1.1 ± 0.1	0.35 ± 0.01

[a] Overall cracking; [b] Dehydrogenation.

4.2 Analysis of reaction barriers and transition states in n-pentane cracking

4.2.1 Adsorption of n-pentane

As the first step of the reaction. n-pentane adsorption has been discussed in the **Section 3.2.2** for its IR properties, nevertheless, an energetic understanding for this procedure is indispensable to comprehend the intrinsic steps undergoing the reaction.

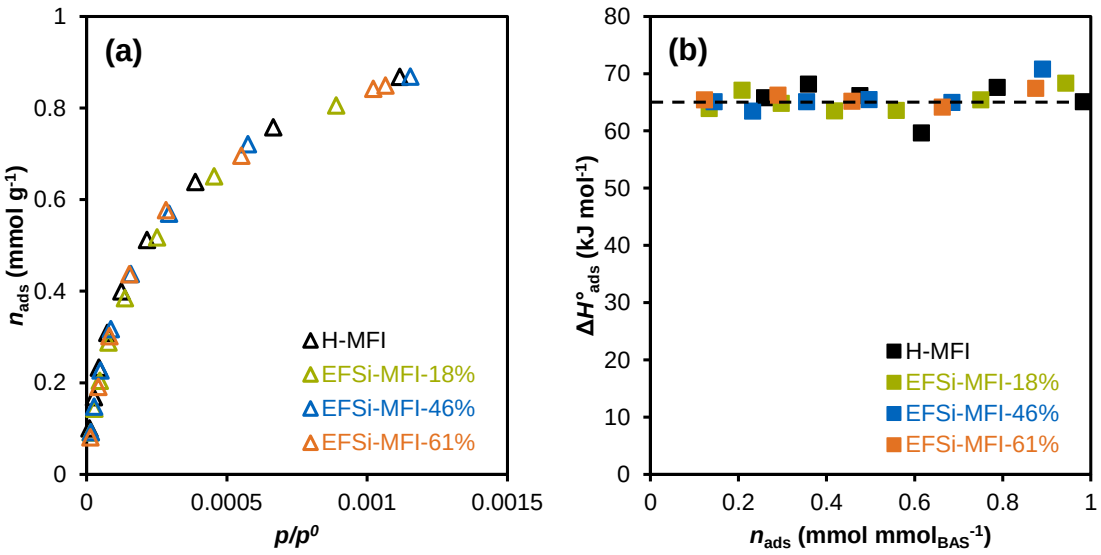

Figure 4.4. (a) Adsorption isotherms of n-pentane and (b) the heat of adsorption as a function of the concentration of adsorbed n-pentane on H-MFI and EFSi-MFIs at 333 K.

Consequently, the adsorption isotherms of n-pentane on all the samples were measured on a microbalance and they all follow a Langmuir type adsorption (**Figure 4.4 a**). Below 1.5 mbar of pentane, the adsorption isotherms on H-MFI and all three EFSi-MFI samples were identical (**Figure 4.4 a**). By fitting with Langmuir adsorption equation, all the samples show similar adsorption constants K_{ads}^{Θ}, 7.4 × 10^3 for H-MFI and ~6.8 × 10^3 for EFSi-MFI samples (**Table 4.7**). The

heat of adsorption measured by calorimetry was ~65 kJ mol^{-1} for all samples (**Figure 4.4 b**), which agrees well with the values reported earlier for MFI zeolites[89]. The adsorption entropy is then calculated by van't Hoff type equation (**Equation 2.2**). As the adsorption constants and the enthalpies ($\Delta H^{\ominus}_{ads}$) and entropies ($\Delta S^{\ominus}_{ads}$) of n-pentane sorption on H-MFI and EFSi-MFIs were identical (**Table 4.7**), we conclude that the differences in the thermodynamic properties of sorbed n-pentane are too small to discern despite the differences in their interaction modes (see **Scheme.3.3**).

Table 4.7. Adsorption properties of n-pentane on H-MFI and EFSi-MFIs at 333 K.

Sample	$K^{\ominus}_{ads} \times 10^3$	$\Delta H^{\ominus}_{ads}$ (kJ mol^{-1})	$\Delta S^{\ominus}_{ads}$ (J mol^{-1} K^{-1})
H-MFI	7.4 ± 1.0	-65 ± 3	-121 ± 6
EFSi-MFI-18%	6.9 ± 0.7	-65 ± 2	-122 ± 4
EFSi-MFI-46%	6.7 ± 0.6	-66 ± 2	-125 ± 4
EFSi-MFI-61%	6.8 ± 0.4	-66 ± 1	-125 ± 2

4.2.2 Analysis of the reaction barriers in n-pentane cracking

The TOFs and corresponding first order rate constants at different temperatures for both BAS and EFSi-BAS (**Tables 4.1** and **4.5**) were used to determine the first order activation enthalpies ($\Delta H^{\ddagger\ominus}_{1st}$) and entropies ($\Delta S^{\ddagger\ominus}_{1st}$) (**Figure 4.5**, **Table 4.8**). Compared to the BAS, the $\Delta H^{\ddagger\ominus}_{1st}$ for the overall cracking is 37 kJ mol^{-1} lower on EFSi-BAS, for the dehydrogenation pathway it is 51 kJ mol^{-1} lower. Since the adsorbed state of n-pentane has the same energy on both sites, the lower activation enthalpy is concluded to represent an enthalpic stabilization of the transition state on EFSi-BAS compared to BAS. The

significantly lower $\Delta S_{1st}^{\ddagger\Theta}$ with EFSi-BAS suggests that the formed carbonium ion in the transition state is bound significantly tighter to the zeolite than for the parent MFI.

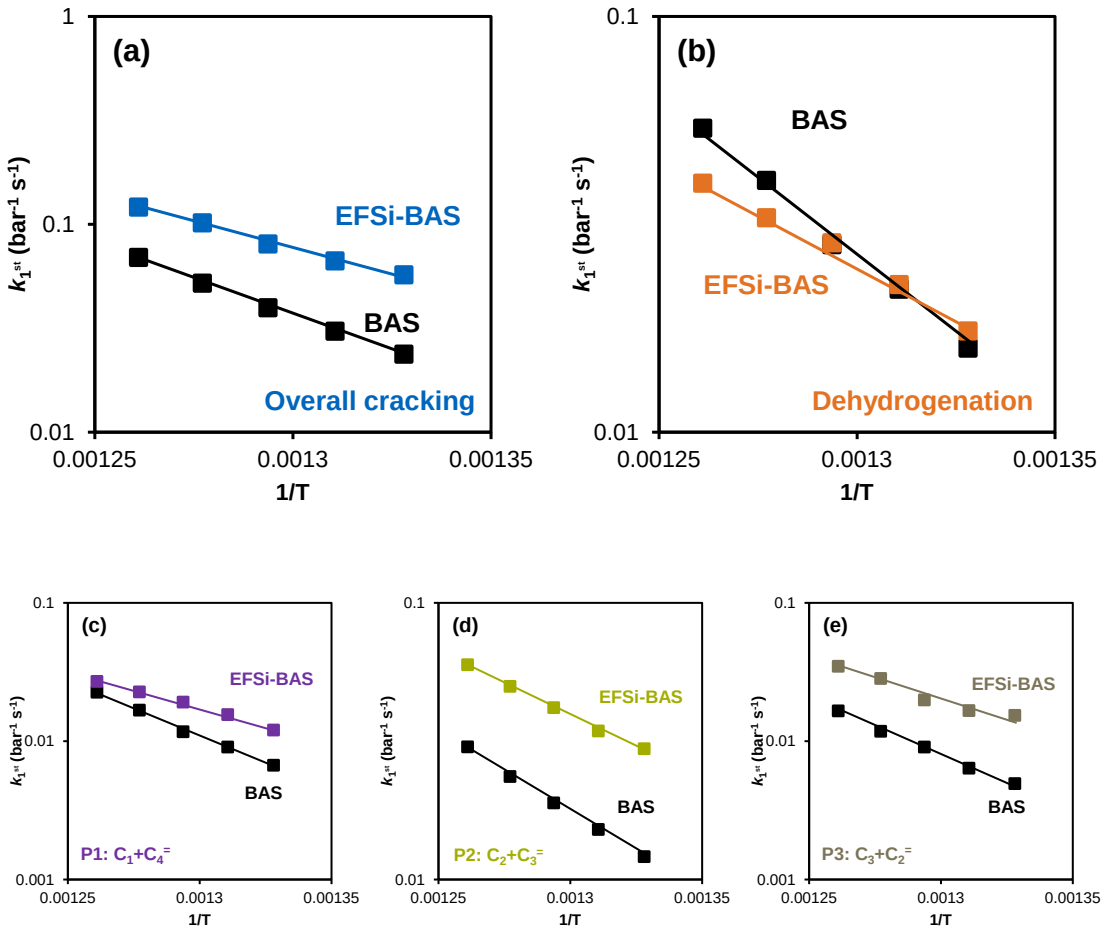

Figure 4.5. Arrhenius plots of n-pentane cracking, shown by first order rate constant. (a) Overall cracking, (b) dehydrogenation and (c) – (e) different cracking pathways on BAS (black synbols) and EFSi-BAS (colored symbols). .

The difference to the role of extra-lattice alumina, enhancing the catalytic activity for cracking, should be highlighted at this point. The rate enhancement by extra-framework Al in close proximity to the BAS (EFAl-BAS)[89,129], is caused mainly by a higher transition entropy, overcompensating a minor destabilization in the transition state enthalpy, while in this case of extra-framework Si the transition enthalpy was markedly lower.

Table 4.8. First order activation enthalpy and entropy of n-pentane cracking and dehydrogenation on BAS/EFSi-BAS.

Active site	$\Delta H_{1st}^{\ddagger\Theta}$ (kJ mol^{-1})					$\Delta S_{1st}^{\ddagger\Theta}$ (J mol^{-1} K^{-1})				
	P1	P2	P3	Overall[a]	Dehyd.[b]	P1	P2	P3	Overall[a]	Dehyd.[b]
BAS	145 ± 5	106 ± 2	144 ± 5	126 ± 2	144 ± 5	-102 ± 9	-149 ± 7	-106 ± 9	-116 ± 7	-95 ± 8
EFSi-BAS	93 ± 3	81 ± 2	101 ± 12	89 ±4	93 ± 10	-166 ± 5	-174 ± 3	-154 ± 11	-158 ± 5	-160 ± 8
Difference[c]	52 ± 6	25 ± 3	43 ± 13	37 ± 4	51 ± 11	-64 ± 10	-25 ± 7	-48 ± 14	-42 ± 9	-65 ± 11

[a] Overall cracking; [b] Dehydrogenation; [c] Difference value between EFSi-BAS and BAS.

4.2.3 Analysis of the transition states in n-pentane cracking

The presence of EFSi in proximity to the BAS leads to significant larger decrease of $\Delta H_{1st}^{\ddagger\ominus}$ in the P1 and P3 pathways (52 kJ mol^{-1}and 43 kJ mol^{-1}, respectively, **Table 4.8**), while the decrease in the P2 pathway is smaller (25 kJ mol^{-1}). This suggests different transition states for cracking pathways. As shown in **Scheme 4.2**, both P1 and P3 pathways go through a C2 carbonium ion like transition state (C ··· C$^+$—C—C—C and C—C$^+$ ··· C—C—C), while P2 pathway passes through a C3 carbonium ion like transition state (C—C ··· C$^+$—C—C).

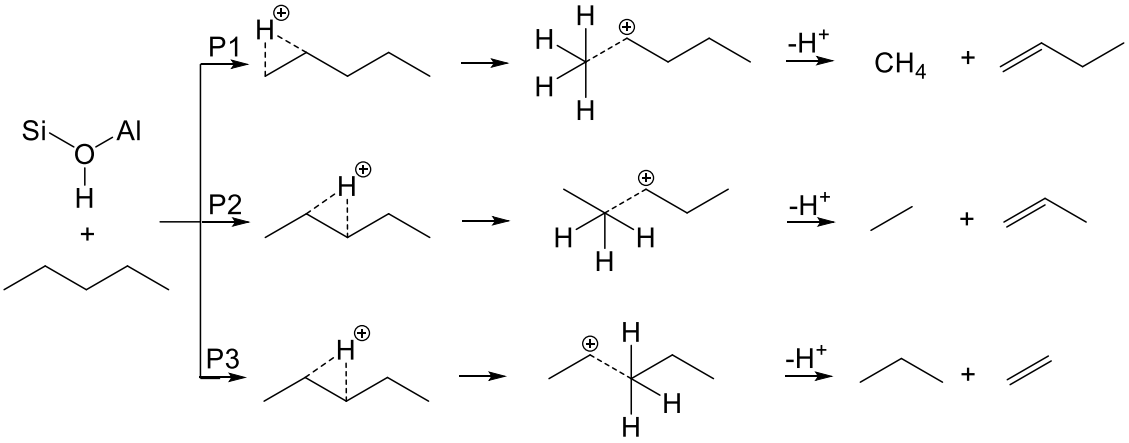

Scheme 4.2. Cracking pathways going through C2 and C3 carbonium ion.

To explore possible subtle steric effects, we used alkyl amines that lead to aminium ions with substituents that are analogous to the substituents of the formed carbonium ions. Adsorption of N-methylpropylamine (CNCCC) and diethylamine (CCNCC) on BAS forms N-methylpropylaminium ion (CN$^+$CCC) and diethylaminium ion (CCN$^+$CC), which simulate C2 carbonium ion like transition state (CC$^+$CCC) for P1/P3 and C3 carbonium ion like transition state (CCC$^+$CC) for P2 cracking pathways (**Scheme 4.3**) because of the similar structures and the same position of the positive charges in the molecules. The

adsorption enthalpies of CNCCC and CCNCC on H-MFI and EFSi-MFI were used to explore steric factors of the carbocation stabilization.

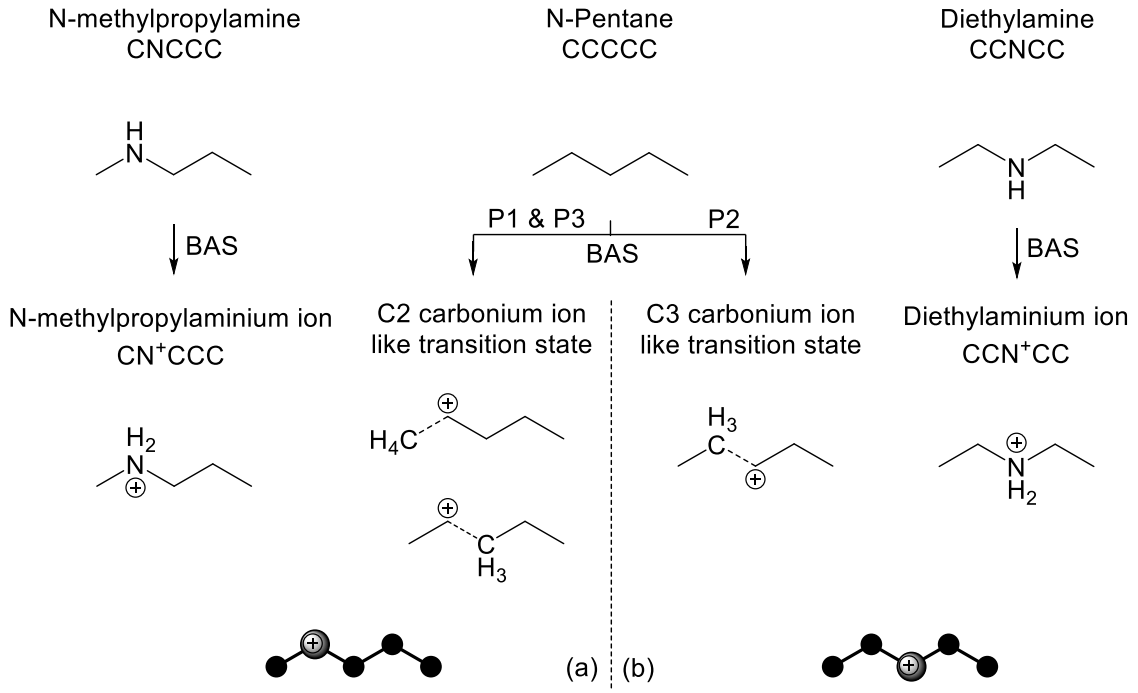

Scheme 4.3. Amine adsorption on BAS simulating different transition states in n-pentane cracking. (a) N-Methylpropylamine adsorption on BAS simulating the C2 carbonium ion like transition state for P1 and P3 cracking pathways and (b) diethylamine adsorption on BAS simulating the C3 carbonium ion like transition state for P2 cracking pathway.

Figure 4.6 shows the calorimetrically measured differential heat and integral heat of adsorption of CNCCC (**Fig. 4.6 a**) and CCNCC (**Fig. 4.6 b**) as a function of their uptake on H-MFI and EFSi-MFI-46% samples at 423 K. Under the amine uptake of 0.2 mol mol_{BAS}^{-1}, the integral heat showed a linear increase with the uptake, thus the heats of adsorption for CNCCC and CCNCC were calculated from the slopes, being 226 and 250 kJ mol^{-1} for CNCCC on H-MFI and EFSi-MFI-46%, and 217 and 230 kJ mol^{-1} for CCNCC on H-MFI and EFSi-MFI-46%, respectively. The heat of adsorption for both amines on H-MFI is in good agreement with the reported results[72,167]. Both amines showed higher

adsorption heats on EFSi-MFI than on H-MFI, indicating a stronger interaction of the corresponding aminium ions on EFSi-BAS.

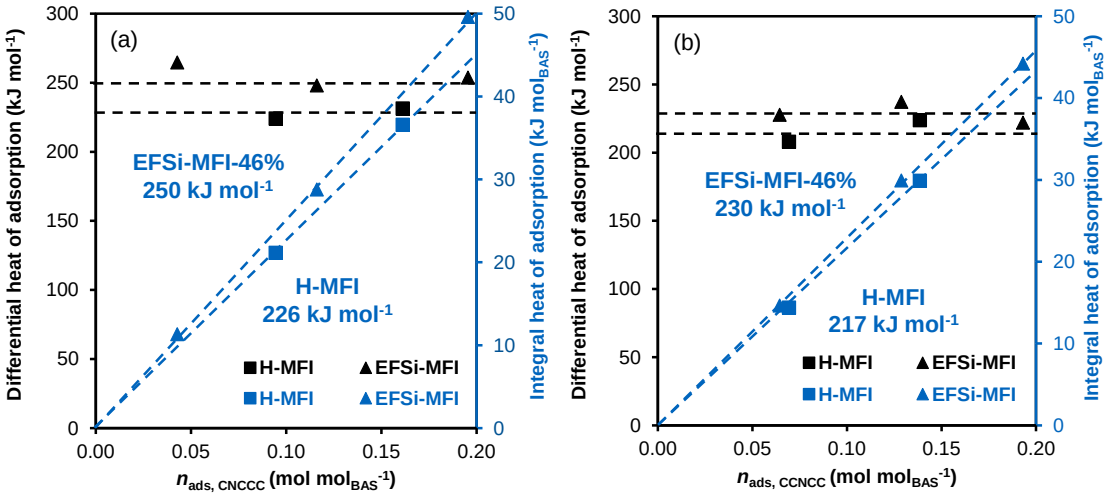

Figure 4.6. Adsorption heat of amines on H-MFi and EFSi-MFI-46%. Differential heat of adsorption (black symbols) and integral heat of adsorption (blue symbols) of (a) N-methylpropylamine (CNCCC) and (b) diethylamine (CCNCC) on H-/EFSi-MFI at 423K.

As the heat of adsorption of EFSi-MFI entails both BAS and EFSi-BAS, the specific contributions of BAS and EFSi-BAS to the heat of adsorption were determined via the coverages. IR spectra during adsorption of CNCCC and CCNCC on EFSi-MFI-46% show the fraction of covered BAS and EFSi-BAS at a specific amine uptake (**Figure 4.7**). The concentration of the covered overall BAS was equal to concentration of aminium ion, which is characteristic by the N-H bending band at 1605 cm^{-1} [71]. The concentration of covered BAS was determined by the area decrease of the band at 3610 cm^{-1}. Their difference is the concentration of covered EFSi-BAS (**Equation 4.1**):

$$\theta_{\text{EFSi-BAS}}\cdot[\text{EFSi-BAS}]=\theta_{\text{Overall-BAS}}\cdot[\text{Overall-BAS}]-\theta_{\text{BAS}}\cdot[\text{BAS}] \quad (\textbf{Equation 4.1})$$

where $\theta_{EFSi\text{-}BAS}$, $\theta_{Overall\text{-}BAS}$ and θ_{BAS} are the coverage of EFSi-BAS, overall BAS and BAS under a certain amine uptake, [EFSi-BAS], [Overall-BAS] and [BAS] are the concentrations of EFSi-BAS, overall BAS and BAS on EFSi-MFI.

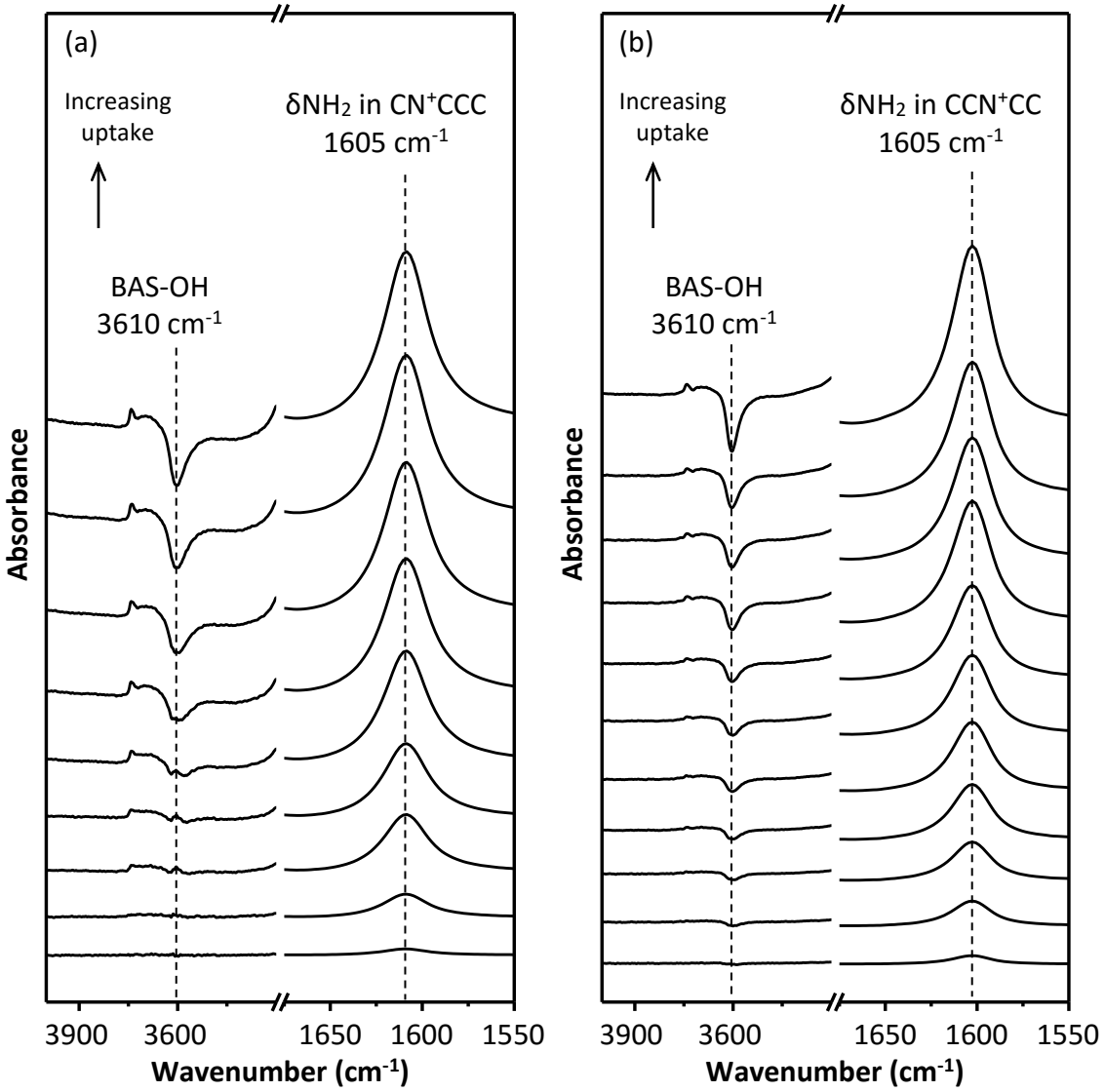

Figure 4.7. Difference IR spectra of O-H stretching vibration region and N-H bending vibration region for (a) C2 (N-methylpropylamine, CNCCC) and (b) C3 (diethylamine, CCNCC) on EFSi-MFI-46% with increasing amine uptake at 423K.

Using only the linear portion of the isotherm below 15 % coverage of the total BAS (**Figure 4.8**), along with the adsorption heat for both amines on BAS

(adsorption heat on H-MFI), the adsorption heat of CNCCC and CCNCC on EFSi-BAS were calculated by **Equation 4.2**:

$$Q_{\text{ads, EFSi-BAS}} = \frac{Q_{\text{ads, Overall-BAS}} \cdot \theta_{\text{Overall-BAS}} \cdot [\text{Overall-BAS}] - Q_{\text{ads, BAS}} \cdot \theta_{\text{BAS}} \cdot [\text{BAS}]}{\theta_{\text{EFSi-BAS}} \cdot [\text{EFSi-BAS}]} \quad \textbf{(Equation 4.2)}$$

where $Q_{\text{ads,Overall-BAS}}$ is the calorimetrically measured differential heat of adsorption on EFSi-MFI, $Q_{\text{ads,BAS}}$ is the differential heat of adsorption on BAS which is obtained by that on H-MFI, and the $Q_{\text{ads,EFSi-BAS}}$ is the differential heat of adsorption on EFSi-BAS.

The adsorption heat of CNCCC and CCNCC on BAS and EFSi-BAS are summarized in **Table 4.9**. Both amines show higher adsorption heat on EFSi-BAS than on BAS (CNCCC: 226 kJ mol^{-1} on BAS and 257 kJ mol^{-1} on EFSi-BAS; CCNCC: 217 kJ mol^{-1} on BAS and 237 kJ mol^{-1} on EFSi-BAS), highlighting the

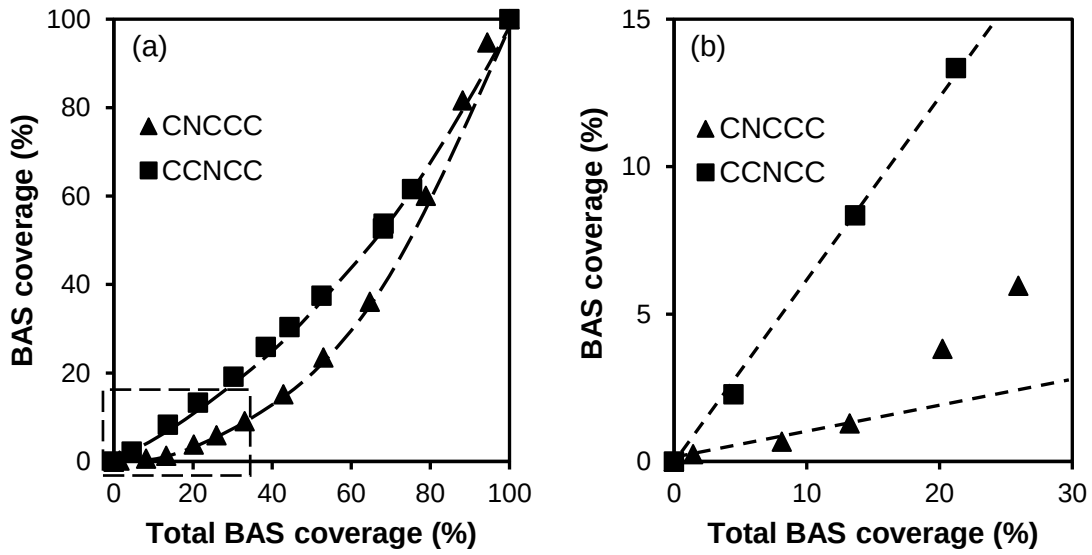

Figure 4.8. BAS coverage (%) as a function of overall BAS coverage (%) for CNCCC (■) and CCNCC (▲) adsorption on EFSi-MFI. (a) Overall scale up to fully coverage of total BAS and (b) amplified scale below 30% coverage of total BAS. (Total BAS coverage determined from the peak area of 1605 cm^{-1} band; BAS coverage determined from the peak area of 3610 cm^{-1} band.)

Table 4.9. Adsorption heat for N-methylpropylamine (CNCCC) and diethylamine (CCNCC) on H-MFI and EFSi-MFI-46% at 423K.

Entry	Active site	ΔQ_{ads} (kJ mol^{-1})	
		CNCCC	CCNCC
1	H-MFI (**BAS**)	226	217
2	EFSi-MFI-46%	250	230
3	**EFSi-BAS**	257	237
4	$\Delta Q_{ads,\ \textbf{EFSi-BAS}} - \Delta Q_{ads,\ \textbf{BAS}}$	31	20

differences of the enthalpic stabilizations. It is remarkable that the more symmetric amine showed a weaker interaction with the BAS in spite of their same proton affinity (~ 950 kJ mol^{-1})[168], suggesting that the more symmetric molecule faces a less tight binding. As previously discussed with n-pentane cracking on EFSi-BAS, the better enthalpic stabilization of the carbonium ion like transition state by the presence of EFSi causes the higher catalytic activity. This is in line with the enthalpic stabilization of aminium ion by the presence of EFSi. The higher increase of adsorption enthalpy of CNCCC on EFSi-BAS (31 kJ mol^{-1}, **Table 4.9 Entry 4**) than of CCNCC (20 kJ mol^{-1}, **Table 4.9 Entry 4**) mirrors the larger transition enthalpy decrease of C2 carbonium ion like transition state (CC^{+}CCC) in the P1 and P3 cracking pathways than that of C3 carbonium ion like transition state (CCC^{+}CC) in the P2 cracking pathway. This reaffirms the hypothesis that the cracking pathways are differentiated with the new sites along the differences of the transition enthalpy.

4.3 Chapter summary

The EFSi-BAS show a higher rate of cracking of n-pentane by enthalpically stabilizing the transition state. The enthalpy of C2 carbonium ion like transition state (CC^{+}CCC), associated with the cracking pathways producing

methane and propane, decreased by 43~52 kJ mol^{-1}, while the C3 carbonium ion like transition state ($CCC^{+}CC$), associated with the pathway leading to ethane, the P2 cracking pathway, decreased by 25 kJ mol^{-1}. The dehydrogenation transition enthalpy also decreased by 51 kJ mol^{-1}, but the rate was identical.

N-methylpropylamine and diethylamine were adsorbed on H-MFI and EFSi-MFI-46% simulating C2 and C3 carbonium ion like transition state undergoing n-pentane cracking. Using the analogy of the stabilization of alkyl aminium ions we hypothesize that the differences in the cracking rates of the different pathways are caused by steric constraints for the bulkier carbonium ions. The higher adsorption enthalpy for both amines on EFSi-BAS indicates that EFSi can stabilize better the transition state intermediates. Thus, EFSi grafting in vicinity of the BAS can change the chemical environment of the active sites, leading a significant decrease of the intrinsic enthalpy of n-pentane cracking, which, in turn, increases the reaction rates.

Chapter 5. Summary and conclusion

Novel BAS are generated via anchoring of EFSi species in vicinity of BAS in H-MFI zeolite. In this novel Brønsted acid site, the bridging OH group (SiOHAl) is a neighbor to the newly generated $Si(OH)_x$ groups. The proximity of the EFSi species and the BAS has been proved by IR spectra adsorbing different probe molecules such as pyridine, n-pentane, etc..

The modification of grafting EFSi keeps the micropore volume and BET surface area of the MFI sample and makes no difference in the acid strength of the anchored BAS, showing the same TPD curves of the adsorbed ammonia. Moreover, the combined physisorption and polarization induced hydrogen bonding showed equal strength for n-pentane on both normal BAS and EFSi-BAS. In accordance of the IR spectra with n-pentane and water adsorption on EFSi-MFI, a proposed structure of the new EFSi-BAS sites was given.

However, the proximity of both functional groups of EFSi and BAS leads to hydrogen bonding and strengthens the interaction with bases such as pyridine, alkyl amines and diethyl ether. The binding strength of these bases was stronger on these EFSi-BAS sites, which is reflected by the preferential adsorption of these probe molecules on EFSi-BAS. The stronger binding of pyridine, alkyl amines and diethyl ether is attributed to a more constrained environment created by the grafted EFSi groups, introducing additional van der Waals interaction with the alkyl or aryl chain of the base probe molecules.

The EFSi-BAS show a higher rate of cracking of n-pentane by enthalpically stabilizing the transition state. Using the analogy of the stabilization of alkyl aminium ions, the differences in the changes of activation energy on different pathways are hypothesized to be caused by the specific steric constraints for different transition carbonium ions.

Thus, the modification of the pore environment by $Si(OH)_x$ groups leads to Brønsted acid sites with more steric constraints, which are able to stabilize the transition states of n-pentane cracking via a significant decrement of the transition enthalpy, which, in turn, increases the reaction rates.

References

1. Breck, D. W. & Smith, J. V. Molecular sieves. *Sci. Am.* **200**, 85–96 (1959).

2. Turro, N. J. From boiling stones to smart crystals: Supramolecular and magnetic isotope control of radical-radical reactions in zeolites. *Acc. Chem. Res.* **33**, 637–646 (2000).

3. Ramesh, K. & Reddy, D. D. Zeolites and their potential uses in agriculture. in *Advances in agronomy* **113**, 219–241 (Elsevier, 2011).

4. Cundy, C. S. & Cox, P. A. The hydrothermal synthesis of zeolites: history and development from the earliest days to the present time. *Chem. Rev.* **103**, 663–702 (2003).

5. Rabenau, A. The role of hydrothermal synthesis in preparative chemistry. *Angew. Chemie Int. Ed. English* **24**, 1026–1040 (1985).

6. Morey, G. W. & Ingerson, F. E. The pneumatolytic and hydrothermal alteration and synthesis of silicates. *Econ. Geol.* **32**, 607–761 (1937).

7. Baerlocher, C., Olson, D. H. & Meier, W. M. *Atlas of Zeolite framework types (formerly: Atlas of Zeolite structure types)*. (Elsevier, 2001).

8. Barrer, R. M. 33. Synthesis of a zeolitic mineral with chabazite-like sorptive properties. *J. Chem. Soc.* 127–132 (1948).

9. Barrer, R. M., Hinds, L. & White, E. A. 299. The hydrothermal chemistry of silicates. Part III. Reactions of analcite and leucite. *J. Chem. Soc.* 1466–1475 (1953).

10. Barrer, R. M. & Marcilly, C. Hydrothermal chemistry of silicates. Part XV. Synthesis and nature of some salt-bearing aluminosilicates. *J. Chem. Soc. A Inorganic, Phys. Theor.* 2735–2745 (1970).

11. Wadlinger, R. L., Kerr, G. T. & Rosinski, E. Patent 3,308,069, 1967.(b) Plank.

12. Argauer, R. J. & Landolt, G. R. US Patent 3,702,886 (1972). (1977).

13. Flanigen, E. M. *et al.* Silicalite, a new hydrophobic crystalline silica molecular sieve. *Nature* **271**, 512 (1978).

14. Flanigen, E. M. & Patton, R. Patent 4,073,865, 1978.

15. Wilson, S. T., Lok, B. M., Messina, C. A., Cannan, T. R. & Flanigen, E. M. Aluminophosphate molecular sieves: a new class of microporous crystalline inorganic solids. *J. Am. Chem. Soc.* **104**, 1146–1147 (1982).

16. Dutta, P. K. & Shieh, D. C. Crystallization of zeolite A: A spectroscopic study. *J. Phys. Chem.* **90**, 2331–2334 (1986).

17. Di Renzo, F., Cambon, H. & Dutartre, R. A 28-year-old synthesis of micelle-templated mesoporous silica. *Microporous Mater.* **10**, 283–286 (1997).

18. Xu, W., Dong, J., Li, J., Li, J. & Wu, F. A novel method for the preparation of zeolite ZSM-5. *J. Chem. Soc. Chem. Commun.* 755–756 (1990).

19. Murayama, N., Yamamoto, H. & Shibata, J. Mechanism of zeolite synthesis from coal fly ash by alkali hydrothermal reaction. *Int. J. Miner. Process.* **64**, 1–17 (2002).

20. Cooper, E. R. *et al.* Ionic liquids and eutectic mixtures as solvent and template in synthesis of zeolite analogues. *Nature* **430**, 1012 (2004).

21. Cejka, J., Corma, A. & Zones, S. *Zeolites and catalysis: synthesis, reactions and applications*. (John Wiley & Sons, 2010).

22. Cundy, C. S. & Cox, P. A. The hydrothermal synthesis of zeolites: Precursors, intermediates and reaction mechanism. *Microporous mesoporous Mater.* **82**, 1–78 (2005).

23. Groen, J. C., Peffer, L. A. A., Moulijn, J. A. & Pérez-Ramırez, J. On the introduction of intracrystalline mesoporosity in zeolites upon desilication in alkaline medium. *Microporous Mesoporous Mater.* **69**, 29–34 (2004).

24. Groen, J. C., Moulijn, J. A. & Pérez-Ramírez, J. Alkaline posttreatment of MFI

zeolites. From accelerated screening to scale-up. *Ind. Eng. Chem. Res.* **46**, 4193–4201 (2007).

25. Pophale, R., Cheeseman, P. A. & Deem, M. W. A database of new zeolite-like materials. *Phys. Chem. Chem. Phys.* **13**, 12407–12412 (2011).

26. McCusker, C. B. and L. B. No Title. *Database of Zeolite Structures* http://www.iza-structure.org/databases/

27. Meier, W. M. & Moeck, H. J. The topology of three-dimensional 4-connected nets: classification of zeolite framework types using coordination sequences. *J. Solid State Chem.* **27**, 349–355 (1979).

28. Davis, M. E. The Quest for Extra-Large Pore, Crystalline Molecular Sieves. *Chem. Eur. J.* **3**, 1745–1750 (1997).

29. Dusselier, M. & Davis, M. E. Small-pore zeolites: synthesis and catalysis. *Chem. Rev.* **118**, 5265–5329 (2018).

30. Kumar, R., Rao, G. N. & Ratnasamy, P. Influence of the pore geometry of medium pore zeolites ZSM-5,-22,-23,-48 and-50 on shape selectivity in reactions of aromatic hydrocarbons. in *Studies in Surface Science and Catalysis* **49**, 1141–1150 (Elsevier, 1989).

31. Jiang, J., Yu, J. & Corma, A. Extra-large-pore zeolites: bridging the gap between micro and mesoporous structures. *Angew. Chemie Int. Ed.* **49**, 3120–3145 (2010).

32. Newsam, J. M. The zeolite cage structure. *Science (80-.).* **231**, 1093–1099 (1986).

33. Csicsery, S. M. Shape-selective catalysis in zeolites. *Zeolites* **4**, 202–213 (1984).

34. Smit, B. & Maesen, T. L. M. Towards a molecular understanding of shape selectivity. *Nature* **451**, 671–678 (2008).

35. Smit, B. & Maesen, T. L. M. Molecular simulations of zeolites: Adsorption, diffusion, and shape selectivity. *Chem. Rev.* **108**, 4125–4184 (2008).

36. Corma, A. Inorganic solid acids and their use in acid-catalyzed hydrocarbon

reactions. *Chem. Rev.* **95**, 559–614 (1995).

37. Weitkamp, J. Zeolites and catalysis. *Solid State Ionics* **131**, 175–188 (2000).

38. Dapsens, P. Y., Mondelli, C. & Pérez-Ramírez, J. Design of Lewis-acid centres in zeolitic matrices for the conversion of renewables. *Chem. Soc. Rev.* **44**, 7025–7043 (2015).

39. Almutairi, S. M. T., Mezari, B., Pidko, E. A., Magusin, P. C. M. M. & Hensen, E. J. M. Influence of steaming on the acidity and the methanol conversion reaction of HZSM-5 zeolite. *J. Catal.* **307**, 194–203 (2013).

40. Holzinger, J., Beato, P., Lundegaard, L. F. & Skibsted, J. Distribution of Aluminum over the Tetrahedral Sites in ZSM-5 Zeolites and Their Evolution after Steam Treatment. *J. Phys. Chem. C* **122**, 15595–15613 (2018).

41. Barrer, R. M. & Townsend, R. P. Transition metal ion exchange in zeolites. Part 1.—Thermodynamics of exchange of hydrated Mn 2+, Co 2+, Ni 2+, Cu 2+ and Zn 2+ ions in ammonium mordenite. *J. Chem. Soc. Faraday Trans. 1 Phys. Chem. Condens. Phases* **72**, 661–673 (1976).

42. Li, G. & Pidko, E. A. The nature and catalytic function of cation sites in zeolites: a computational perspective. *ChemCatChem* **11**, 134–156 (2019).

43. Kokotailo, G. T., Lawton, S. L., Olson, D. H. & Meier, W. M. Structure of synthetic zeolite ZSM-5. *Nature* **272**, 437–438 (1978).

44. Jacobs, P. A., Beyer, H. K. & Valyon, J. Properties of the end members in the Pentasil-family of zeolites: characterization as adsorbents. *Zeolites* **1**, 161–168 (1981).

45. Ch. Baerlocher and L.B. McCusker. Database of Zeolite Structures. *Http://www.iza-structure.org/databases/*

46. Dyer, A. An introduction to zeolite molecular sieves. (1988).

47. Rahimi, N. & Karimzadeh, R. Catalytic cracking of hydrocarbons over modified

ZSM-5 zeolites to produce light olefins: A review. *Appl. Catal. A Gen.* **398**, 1–17 (2011).

48. Babitz, S. M. M. *et al.* Monomolecular cracking of n-hexane on Y, MOR, and ZSM-5 zeolites. *Appl. Catal. A Gen.* **179**, 71–86 (1999).

49. Weitkamp, J., Jacobs, P. A. & Martens, J. A. Isomerization and hydrocracking of C9 through C16 n-alkanes on Pt/HZSM-5 zeolite. *Appl. Catal.* **8**, 123–141 (1983).

50. Young, L. B., Butter, S. A. & Kaeding, W. W. Shape selective reactions with zeolite catalysts: III. Selectivity in xylene isomerization, toluene-methanol alkylation, and toluene disproportionation over ZSM-5 zeolite catalysts. *J. Catal.* **76**, 418–432 (1982).

51. Xu, B., Sievers, C., Hong, S. B., Prins, R. & van Bokhoven, J. A. Catalytic activity of Brønsted acid sites in zeolites: Intrinsic activity, rate-limiting step, and influence of the local structure of the acid sites. *J. Catal.* **244**, 163–168 (2006).

52. Ward, J. W. The nature of active sites on zeolites: V. In situ spectroscopic observations of hydrogen Y zeolite during cumene cracking. *J. Catal.* **11**, 259–260 (1968).

53. Kissin, Y. V. Chemical Mechanisms of Catalytic Cracking over Solid Acidic Catalysts: Alkanes and Alkenes. *Catal. Rev. - Sci. Eng.* **43**, 85–146 (2001).

54. Ozaki, A. & Kimura, K. The effective site on acid catalysts revealed in n-butene isomerization. *J. Catal.* **3**, 395–405 (1964).

55. Asuquo, R. A., Edermirth, G. & Lercher, J. A. n-Butane Isomerization over Acidic Mordenite. *J. Catal.* **155**, 376–382 (1995).

56. Feller, A. & Lercher, J. A. Chemistry and technology of isobutane/alkene alkylation catalyzed by liquid and solid acids. *ChemInform* **35**, no-no (2004).

57. Shirazi, L., Jamshidi, E. & Ghasemi, M. R. The effect of Si/Al ratio of ZSM-5 zeolite on its morphology, acidity and crystal size. *Cryst. Res. Technol. J. Exp. Ind. Crystallogr.* **43**, 1300–1306 (2008).

58. Burkett, S. L. & Davis, M. E. Mechanisms of structure direction in the synthesis of pure-silica zeolites. 1. Synthesis of TPA/Si-ZSM-5. *Chem. Mater.* **7**, 920–928 (1995).

59. Dědeček, J., Kaucký, D., Wichterlová, B. & Gonsiorová, O. Co 2+ ions as probes of Al distribution in the framework of zeolites. ZSM-5 study. *Phys. Chem. Chem. Phys.* **4**, 5406–5413 (2002).

60. Sazama, P. *et al.* Effect of aluminium distribution in the framework of ZSM-5 on hydrocarbon transformation. Cracking of 1-butene. *J. Catal.* **254**, 180–189 (2008).

61. Janda, A. & Bell, A. T. Effects of Si/Al ratio on the distribution of framework Al and on the rates of alkane monomolecular cracking and dehydrogenation in H-MFI. *J. Am. Chem. Soc.* **135**, 19193–19207 (2013).

62. Naccache, C., Ren, C. F. & Coudurier, G. Strength of Acid Sites in Zeolites Using Uv-Visible Spectroscopy: Effect of Al Content. *Stud. Surf. Sci. Catal.* **49**, 661–668 (1989).

63. Masuda, T., Fujikata, Y., Mukai, S. R. & Hashimoto, K. Changes in catalytic activity of MFI-type zeolites caused by dealumination in a steam atmosphere. *Appl. Catal. A Gen.* **172**, 73–83 (1998).

64. Li, S. *et al.* Brønsted/Lewis acid synergy in dealuminated HY zeolite: a combined solid-state NMR and theoretical calculation study. *J. Am. Chem. Soc.* **129**, 11161–11171 (2007).

65. Chu, C. T., Chang, C. D. & Si, C. Al. Isomorphous Substitution in Zeolite Frameworks. 1. Acidity. *J. Phys. Chem.* 1569–1571 (1985). doi:10.1021/j100255a005

66. Losch, P. *et al.* Proton mobility, intrinsic acid strength, and acid site location in zeolites revealed by varying temperature infrared spectroscopy and density functional theory studies. *J. Am. Chem. Soc.* **140**, 17790–17799 (2018).

67. Jones, A. J., Carr, R. T., Zones, S. I. & Iglesia, E. Acid strength and solvation in

catalysis by MFI zeolites and effects of the identity, concentration and location of framework heteroatoms. *J. Catal.* **312**, 58–68 (2014).

68. Ward, J. W. The nature of active sites on zeolites. VIII. Rare earth Y zeolite. *J. Catal.* **13**, 321–327 (1969).

69. Xiaoning, W. *et al.* Effects of Light Rare Earth on Acidity and Catalytic Performance of HZSM-5 Zeolite for Catalytic Cracking of Butane to Light Olefins. *J. Rare Earths* **25**, 321–328 (2007).

70. Martins, A., Silva, J. M. & Ribeiro, M. F. Influence of rare earth elements on the acid and metal sites of Pt/HBEA catalyst for short chain n-alkane hydroisomerization. *Appl. Catal. A Gen.* **466**, 293–299 (2013).

71. Parrillo, D. J., Adamo, A. T., Kokotailo, G. T. & Gorte, R. J. Amine adsorption in H-ZSM-5. *Appl. Catal.* **67**, 107–118 (1990).

72. Parrillo, D. J., Lee, C. & Gorte, R. J. Heats of adsorption for ammonia and pyridine in H-ZSM-5: evidence for identical Brønsted-acid sites. *Appl. Catal. A, Gen.* **110**, 67–74 (1994).

73. Hidalgo, C. V, Itoh, H., Hattori, T., Niwa, M. & Murakami, Y. Measurement of the acidity of various zeolites by temperature-programmed desorption of ammonia. *J. Catal.* **85**, 362–369 (1984).

74. Katada, N., Igi, H., Kim, J.-H. & Niwa, M. Determination of the acidic properties of zeolite by theoretical analysis of temperature-programmed desorption of ammonia based on adsorption equilibrium. *J. Phys. Chem. B* **101**, 5969–5977 (1997).

75. Niwa, M. & Katada, N. Measurements of acidic property of zeolites by temperature programmed desorption of ammonia. *Catal. Surv. from Asia* **1**, 215–226 (1997).

76. Richardson, R. L. & Benson, S. W. A study of the surface acidity of cracking catalyst. *J. Phys. Chem.* **61**, 405–411 (1957).

77. Lercher, J. A., Gründling, C. & Eder-Mirth, G. Infrared studies of the surface acidity of oxides and zeolites using adsorbed probe molecules. *Catal. Today* **27**, 353–376 (1996).

78. Parry, E. P. An infrared study of pyridine adsorbed on acidic solids. Characterization of surface acidity. *J. Catal.* **2**, 371–379 (1963).

79. Basila, M. R., Kantner, T. R. & Rhee, K. H. The Nature of the Acidic Sites on a Silica-Alumina. Characterization by Infrared Spectroscopic Studies of Trimethylamine and Pyridine Chemisorption1. *J. Phys. Chem.* **68**, 3197–3207 (1964).

80. Emeis, C. A. Determination of integrated molar extinction coefficients for infrared absorption bands of pyridine adsorbed on solid acid catalysts. *J. Catal.* **141**, 347–354 (1993).

81. Fleischer, U., Kutzelnigg, W., Bleiber, A. & Sauer, J. 1H NMR Chemical Shift and Intrinsic Acidity of Hydroxyl Groups. Ab Initio Calculations on Catalytically Active Sites and Gas-Phase Molecules. *J. Am. Chem. Soc.* **115**, 7833–7838 (1993).

82. Pinto, R. R. *et al.* Correlating NH3-TPD and 1H MAS NMR measurements of zeolite acidity: Proposal of an acidity scale. *Appl. Catal. A Gen.* **284**, 39–46 (2005).

83. Gabrienko, A. A. *et al.* Direct Measurement of Zeolite Brønsted Acidity by FTIR Spectroscopy: Solid-State 1H MAS NMR Approach for Reliable Determination of the Integrated Molar Absorption Coefficients. *J. Phys. Chem. C* **122**, 25386–25395 (2018).

84. Wang, M. *et al.* Genesis and Stability of Hydronium Ions in Zeolite Channels. *J. Am. Chem. Soc.* **141**, 3444–3455 (2019).

85. Fenzke, D., Hunger, M. & Pfeifer, H. Determination of nuclear distances and chemical-shift anisotropy from 1H MAS NMR sideband patterns of surface OH groups. *J. Magn. Reson.* **95**, 477–483 (1991).

86. Klinowski, J. Solid-State NMR Studies of Molecular Sieve Catalysts. *Chem. Rev.* **91**, 1459–1479 (1991).

87. Hunger, M., Anderson, M. W., Ojo, A. & Pfeifer, H. Study of the geometry and location of the bridging OH groups in aluminosilicate and silicoaluminophosphate type zeolites using 1H MAS NMR sideband analysis and CP/MAS NMR. *Microporous Mater.* **1**, 17–32 (1993).

88. Hunger, M. Multinuclear solid-state NMR studies of acidic and non-acidic hydroxyl protons in zeolites. *Solid State Nuclear Magnetic Resonance* **6**, 1–29 (1996).

89. Schallmoser, S. *et al.* Impact of the local environment of Brønsted acid sites in ZSM-5 on the catalytic activity in n-pentane cracking. *J. Catal.* **316**, 93–102 (2014).

90. Müller, M., Harvey, G. & Prins, R. Comparison of the dealumination of zeolites beta, mordenite, ZSM-5 and ferrierite by thermal treatment, leaching with oxalic acid and treatment with SiCl4 by 1H, 29Si and 27Al MAS NMR. *Microporous mesoporous Mater.* **34**, 135–147 (2000).

91. Kawai, T. & Tsutsumi, K. Evaluation of the secondary pore structure of hydrothermally-and acid-treated faujasite type zeolites. *Adsorption* **4**, 225–231 (1998).

92. Karwacki, L. *et al.* Morphology-dependent zeolite intergrowth structures leading to distinct internal and outer-surface molecular diffusion barriers. *Nat. Mater.* **8**, 959 (2009).

93. Carvalho, A. P., de Carvalho, M. B. & Pires, J. Degree of crystallinity of dealuminated offretites determined by X-ray diffraction and by a new method based on nitrogen adsorption. *Zeolites* **19**, 382–386 (1997).

94. Groen, J. C., Moulijn, J. A. & Pérez-Ramírez, J. Desilication: on the controlled generation of mesoporosity in MFI zeolites. *J. Mater. Chem.* **16**, 2121–2131 (2006).

95. Verboekend, D. & Pérez-Ramírez, J. Design of hierarchical zeolite catalysts by desilication. *Catal. Sci. Technol.* **1**, 879–890 (2011).

96. Silaghi, M.-C., Chizallet, C. & Raybaud, P. Challenges on molecular aspects of dealumination and desilication of zeolites. *Microporous Mesoporous Mater.* **191**, 82–96 (2014).

97. O'Connor, C. T., Möller, K. P. & Manstein, H. The effect of silanisation on the catalytic and sorption properties of zeolites. *KONA Powder Part. J.* **25**, 230–236 (2007).

98. Tago, T., Iwakai, K., Morita, K., Tanaka, K. & Masuda, T. Control of acid-site location of ZSM-5 zeolite membrane and its application to the MTO reaction. *Catal. today* **105**, 662–666 (2005).

99. Niwa, M., Kato, M., Hattori, T. & Murakami, Y. Fine control of the pore-opening size of zeolite ZSM-5 by chemical vapor deposition of silicon methoxide. *J. Phys. Chem.* **90**, 6233–6237 (1986).

100. Zheng, S., Heydenrych, H. R., Röger, H. P., Jentys, A. & Lercher, J. A. On the enhanced selectivity of HZSM-5 modified by chemical liquid deposition. *Top. Catal.* **22**, 101–106 (2003).

101. Malola, S., Svelle, S., Bleken, F. L. & Swang, O. Detailed reaction paths for zeolite dealumination and desilication from density functional calculations. *Angew. Chemie Int. Ed.* **51**, 652–655 (2012).

102. Fogler, H. S. External diffusion effects on heterogeneous reactions. *Elem. Chem. React. Eng.* 757–801 (2006).

103. Klaewkla, R., Arend, M. & Hoelderich, W. F. A review of mass transfer controlling the reaction rate in heterogeneous catalytic systems. in *Mass transfer-Advanced aspects* (IntechOpen, 2011).

104. Davis, M. E. & Davis, R. J. Effects of Transport Limitations on Rates of Solid-Catalyzed Reactions. *Fundam. Chem. React. Eng.* **1**, (2003).

105. Van der Mynsbrugge, J. *et al.* Understanding Brønsted-Acid Catalyzed Monomolecular Reactions of Alkanes in Zeolite Pores by Combining Insights from

Experiment and Theory. *ChemPhysChem* **19**, 338 (2018).

106. Kreuzer, H. J. & Gortel, Z. W. *Physisorption kinetics*. **1**, (Springer Science & Business Media, 2012).

107. Austin Taylor, H. & Thon, N. Kinetics of Chemisorption. *J. Am. Chem. Soc.* **74**, 4169–4173 (1952).

108. Low, M. J. D. Kinetics of chemisorption of gases on solids. *Chem. Rev.* **60**, 267–312 (1960).

109. Moelwyn-Hughes, E. A. & Lewis, D. *Physical Chemistry*. *Journal of The Electrochemical Society* **107**, (1960).

110. Brunauer, S., Emmett, P. H. & Teller, E. Adsorption of Gases in Multimolecular Layers. *J. Am. Chem. Soc.* **60**, 309–319 (1938).

111. Dada, A. O., Olalekan, A. P., Olatunya, A. M. & Dada, O. Langmuir, Freundlich, Temkin and Dubinin–Radushkevich isotherms studies of equilibrium sorption of Zn2+ unto phosphoric acid modified rice husk. *IOSR J. Appl. Chem.* **3**, 38–45 (2012).

112. Dambrowitz, K. A. & Kuznicki, S. M. Henry Eyring: A model life. *Bull. Hist. Chem.* **35**, 46 (2010).

113. Eyring, H. The activated complex in chemical reactions. *J. Chem. Phys.* **3**, 107–115 (1935).

114. Eyring, H. The activated complex and the absolute rate of chemical reactions. *Chem. Rev.* **17**, 65–77 (1935).

115. Lente, G., Fábián, I. & Poë, A. J. A common misconception about the Eyring equation. *New J. Chem.* **29**, 759–760 (2005).

116. Kotrel, S., Knözinger, H. & Gates, B. C. The Haag–Dessau mechanism of protolytic cracking of alkanes. *Microporous Mesoporous Mater.* **35**, 11–20 (2000).

117. Konno, H. *et al.* Kinetics of n-hexane cracking over ZSM-5 zeolites - Effect of

crystal size on effectiveness factor and catalyst lifetime. *Chem. Eng. J.* **207**–**208**, 490–496 (2012).

118. Xu, S., Zhang, X., Cheng, D. guo, Chen, F. & Ren, X. Effect of hierarchical ZSM-5 zeolite crystal size on diffusion and catalytic performance of n-heptane cracking. *Front. Chem. Sci. Eng.* **12**, 780–789 (2018).

119. Haag, W. O., Dessau, R. M. & Lago, R. M. Kinetics and mechanism of paraffin cracking with zeolite catalysts. in *Studies in Surface Science and Catalysis* **60**, 255–265 (Elsevier, 1991).

120. Olah, G. A. Stable carbocations. CXVIII. General concept and structure of carbocations based on differentiation of trivalent (classical) carbenium ions from three-center bound penta-of tetracoordinated (nonclassical) carbonium ions. Role of carbocations in electrophi. *J. Am. Chem. Soc.* **94**, 808–820 (1972).

121. Corma, A. & Orchillés, A. V. Current views on the mechanism of catalytic cracking. *Microporous mesoporous Mater.* **35**, 21–30 (2000).

122. Krannila, H., Haag, W. O. & Gates, B. C. Monomolecular and bimolecular mechanisms of paraffin cracking: n-butane cracking catalyzed by HZSM-5. *J. Catal.* **135**, 115–124 (1992).

123. Haag, W. O. Catalysis by zeolites–science and technology. in *Studies in Surface Science and Catalysis* **84**, 1375–1394 (Elsevier, 1994).

124. Narbeshuber, T. F., Vinek, H. & Lercher, J. A. Monomolecular conversion of light alkanes over H-ZSM-5. *J. Catal.* **157**, 388–395 (1995).

125. Gounder, R. & Iglesia, E. Catalytic consequences of spatial constraints and acid site location for monomolecular alkane activation on zeolites. *J. Am. Chem. Soc.* **131**, 1958–1971 (2009).

126. Gounder, R. & Iglesia, E. The catalytic diversity of zeolites: Confinement and solvation effects within voids of molecular dimensions. *Chem. Commun.* **49**, 3491–3509 (2013).

127. Eder, F. & Lercher, J. A. Alkane sorption in molecular sieves: The contribution of ordering, intermolecular interactions, and sorption on Brønsted acid sites. *Zeolites* **18**, 75–81 (1997).

128. Eder, F., Stockenhuber, M. & Lercher, J. A. Brønsted Acid Site and Pore Controlled Siting of Alkane Sorption in Acidic Molecular Sieves. *J. Phys. Chem. B* **101**, 5414–5419 (1997).

129. Zhang, Y. *et al.* Promotion of protolytic pentane conversion on H-MFI zeolite by proximity of extra-framework aluminum oxide and Brønsted acid sites. *J. Catal.* **370**, 424–433 (2019).

130. Lago, R. M. M. *et al.* The nature of the catalytic sites in HZSM-5 - Activity enhancement. in *Studies in Surface Science and Catalysis* **28**, 677–684 (Elsevier, 1986).

131. van Bokhoven, J. A. *et al.* An explanation for the enhanced activity for light alkane conversion in mildly steam dealuminated mordenite: The dominant role of adsorption. *J. Catal.* **202**, 129–140 (2001).

132. Van Bokhoven, J. A. *et al.* Observation of a compensation relation for monomolecular alkane cracking by zeolites: The dominant role of reactant sorption. *J. Catal.* **224**, 50–59 (2004).

133. Yu, Z. *et al.* Brønsted/lewis acid synergy in H–ZSM-5 and H–MOR zeolites studied by 1H and 27Al DQ-MAS solid-state NMR spectroscopy. *J. Phys. Chem. C* **115**, 22320–22327 (2011).

134. Haag, W. O. Catalysis by Zeolites – Science and Technology. *Stud. Surf. Sci. Catal.* **84**, 1375–1394 (1994).

135. Li, S. *et al.* Probing the spatial proximities among acid sites in dealuminated H-Y zeolite by solid-state NMR spectroscopy. *J. Phys. Chem. C* **112**, 14486–14494 (2008).

136. Gounder, R., Jones, A. J., Carr, R. T. & Iglesia, E. Solvation and acid strength effects

on catalysis by faujasite zeolites. *J. Catal.* **286**, 214–223 (2012).

137. Silaghi, M.-C., Chizallet, C., Sauer, J. & Raybaud, P. Dealumination mechanisms of zeolites and extra-framework aluminum confinement. *J. Catal.* **339**, 242–255 (2016).

138. Xue, N. *et al.* Hydrolysis of zeolite framework aluminum and its impact on acid catalyzed alkane reactions. *J. Catal.* **365**, 359–366 (2018).

139. Zheng, J. *et al.* A periodic DFT study of the synergistic mechanisms between extra-framework aluminum species and Brønsted acid sites in HY zeolites. *Ind. Eng. Chem. Res.* (2020).

140. Der Voort, P. Van & Vansant, E. F. Silylation of the silica surface a review. *J. Liq. Chromatogr. Relat. Technol.* **19**, 2723–2752 (1996).

141. Vasques, M. H., Ramoa Ribeiro, F., Gnep, N. & Guisnet, M. Effects of steaming on the shape selectivity and on the acidity of HZSM 5. *React. Kinet. Catal. Lett.* **38**, 301–306 (1989).

142. Gola, A. *et al.* Effect of leaching agent in the dealumination of stabilized Y zeolites. *Microporous Mesoporous Mater.* **40**, 73–83 (2000).

143. Lutz, W. Zeolite Y: Synthesis, modification, and properties - A case revisited. *Advances in Materials Science and Engineering* **2014**, (2014).

144. Agudelo, J. L., Hensen, E. J. M., Giraldo, S. A. & Hoyos, L. J. Influence of steam-calcination and acid leaching treatment on the VGO hydrocracking performance of faujasite zeolite. *Fuel Process. Technol.* **133**, 89–96 (2015).

145. Wang, L. *et al.* Understanding structure-function relationships in HZSM-5 zeolite catalysts for photocatalytic oxidation of isopropyl alcohol. *J. Catal.* **377**, 322–331 (2019).

146. Jentys, A., Kleestorfer, K. & Vinek, H. Concentration of surface hydroxyl groups on MCM-41. *Microporous Mesoporous Mater.* **27**, 321–328 (1999).

147. Vansant, E. E., Van Der Voort, P. & Vrancken, K. C. *Characterization and Chemical Modification of the Silica Surface*. *Studies in Surface Science and Catalysis* **93**, (1995).

148. Zecchina, A. *et al.* Low-temperature Fourier-transform infrared investigation of the interaction of CO with nanosized ZSM5 and silicalite. *J. Chem. Soc. Faraday Trans.* **88**, 2959–2969 (1992).

149. Trombetta, M., Armaroli, T., Gutièrrez Alejandre, A., Ramirez Solis, J. & Busca, G. An FT-IR study of the internal and external surfaces of HZSM5 zeolite. *Appl. Catal. A Gen.* **192**, 125–136 (2000).

150. Guisnet, M., Ayrault, P., Coutanceau, C., Alvarez, M. F. & Datka, J. Acid properties of dealuminated beta zeolites studied by IR spectroscopy. *J. Chem. Soc. - Faraday Trans.* **93**, 1661–1665 (1997).

151. Zholobenko, V. L., Kustov, L. M., Borovkov, V. Y. & Kazansky, V. B. A new type of acidic hydroxyl groups in ZSM-5 zeolite and in mordenite according to diffuse reflectance i.r. spectroscopy. *Zeolites* **8**, 175–178 (1988).

152. Jentys, A., Warecka, G., Derewinski, M. & Lercher, J. A. Adsorption of water on ZSM 5 zeolites. *J. Phys. Chem.* **93**, 4837–4843 (1989).

153. Loeffler, E. *et al.* Study of different states of nonframework aluminum in hydrothermally dealuminated HZSM-5 zeolites using diffuse reflectance i.r. spectroscopy. *Zeolites* **10**, 266–271 (1990).

154. Larkin, P. *Infrared and Raman spectroscopy: principles and spectral interpretation*. (Elsevier, 2017).

155. De Moor, B. A., Reyniers, M.-F., Gobin, O. C., Lercher, J. A. & Marin, G. B. Adsorption of C2− C8 n-Alkanes in Zeolites. *J. Phys. Chem. C* **115**, 1204–1219 (2010).

156. Keskinen, K. M. *et al.* New Methods for Characterization of the External Surface of ZSM-5-Zeolites. *Stud. Surf. Sci. Catal.* **84**, 875–882 (1994).

157. Boronat, M. & Corma, A. What is measured when measuring acidity in zeolites with probe molecules? *ACS Catal.* acscatal.8b04317 (2019). doi:10.1021/acscatal.8b04317

158. Larrubia, M. A., Ramis, G. & Busca, G. An FT-IR study of the adsorption and oxidation of N-containing compounds over Fe2O3-TiO2 SCR catalysts. *Appl. Catal. B Environ.* **30**, 101–110 (2001).

159. Osuga, R., Yokoi, T. & Kondo, J. N. IR observation of activated ether species on acidic OH groups on H-ZSM-5 zeolites. *Mol. Catal.* **477**, (2019).

160. Jobic, H., Tuel, A., Krossner, M. & Sauer, J. Water in interaction with acid sites in H-ZSM-5 zeolite does not form hydroxonium ions. A comparison between neutron scattering results and ab initio calculations. *J. Phys. Chem.* **100**, 19545–19550 (1996).

161. Claydon, M. F. & Sheppard, N. The nature of 'a,B,C'-type infrared spectra of strongly hydrogen-bonded systems; Pseudo-maxima in vibrational spectra. *J. Chem. Soc. D Chem. Commun.* 1431–1433 (1969). doi:10.1039/C29690001431

162. Bordiga, S. *et al.* FTIR adsorption studies of H2O and CH3OH in the isostructural H-SSZ-13 and H-SAPO-34: Formation of H-bonded adducts and protonated clusters. *J. Phys. Chem. B* **109**, 7724–7732 (2005).

163. Hunger, M. & Horvath, T. Adsorption of methanol on Bronsted acid sites in zeolite H-ZSM-5 investigated by multinuclear solid-state NMR spectroscopy. *J. Am. Chem. Soc.* **118**, 12302–12308 (1996).

164. Pazé, C. *et al.* Acidic properties of H-β zeolite as probed by bases with proton affinity in the 118-204 kcal mol-1 range: A FTIR investigation. *J. Phys. Chem. B* **101**, 4740–4751 (1997).

165. Parrillo, D. J., Gorte, R. J. & Farneth, W. E. A Calorimetric Study of Simple Bases in H-ZSM-5: A Comparison with Gas-Phase and Solution-Phase Acidities. *J. Am. Chem. Soc.* **115**, 12441–12445 (1993).

166. Thursfield, A. & Anderson, M. W. 1H, 2H, and 13C solid-state NMR studies of methanol adsorbed on a series of acidic microporous zeotype materials. *J. Phys. Chem.* **100**, 6698–6707 (1996).

167. Derouane, E. G. & Chang, C. D. Confinement effects in the adsorption of simple bases by zeolites. *Microporous Mesoporous Mater.* **35**–**36**, 425–433 (2000).

168. Cao, J., Aubry, C. & Holmes, J. L. Proton affinities of simple amines; entropies and enthalpies of activation and their effect on the kinetic method for evaluating proton affinities. *J. Phys. Chem. A* **104**, 10045–10052 (2000).

Associated content

Figure 1.6 reprinted with permission from “Jacobs, P. A., Beyer, H. K. & Valyon, J. Properties of the end members in the Pentasil-family of zeolites: characterization as adsorbents. Zeolites 1, 161–168 (1981)”.License number: 4786000174821.

Scheme 1.3 reprinted with permission from “Malola, S., Svelle, S., Bleken, F. L. & Swang, O. Detailed reaction paths for zeolite dealumination and desilication from density functional calculations. Angew. Chemie Int. Ed. 51, 652–655 (2012)”.License number: 4786391470797.